January 2005 ECN-C--05-011

Kristallijn silicium zonnecellen: thermische behandelingen en nieuwe materialen "TherMat II"

Novem contract 2020.01.13.11.002
ECN project 74686

April 1, 2002 to May 31, 2004

L.J. Geerligs, D. Macdonald, A. Azzizi, P. Manshanden, A.R. Burgers, A. Schönecker

Aan dit project is in het kader van het Besluit milieusubsidies, Subsidieregeling milieugerichte technologie een subsidie verleend uit het programma Milieu & Technologie dat gefinancierd wordt door het Ministerie van Volkshuisvesting, Ruimtelijke Ordening en Milieubeheer. SenterNovem beheert deze regeling

Preface

This work presents the results of the project "Kristallijn silicium zonnecellen: thermische behandelingen en nieuwe materialen (TherMat II)", performed by ECN under contract 2020.01.13.11.002 from Novem, between April 1, 2002 and May 31, 2004.
The purpose of TherMat II was to investigate the relation between silicon material quality and solar cell efficiency, and the changes in material which occur as a result of high-temperature process steps.
Silicon wafers are used for 95% of solar cell production worldwide. The quality of the wafer is an important parameter for solar cell efficiency. Variation of quality of wafers in commercially produced batches already causes variation of 10% or more in cell efficiency. Current R&D efforts to produce lower-cost wafers, by using low-cost silicon, or by so-called silicon ribbon-growth, will make lower-quality wafers more common in the future. Therefore understanding of the background of these quality variations, and what can be done about them, is important.

In the course of this project, collaborations have taken place with foreign institutions with expertise on specific subjects:
- Australian National University, with expertise on defects and defect engineering in crystalline silicon.
- Fraunhofer Gesellschaft, Institut für Solare Energiesysteme (FhG-ISE), with expertise on carrier lifetime mapping and light-induced defect changes.
- Technical University of Trondheim, with expertise on Si materials science and Si ingot growth.
- University of Bilbao, with expertise on properties and processing of n-type doped silicon.

Acknowledgments

We gratefully acknowledge Novem for its support to increase ECN's knowledge and capabilities in this important field. Further acknowledgements are due to
- useful discussions and assistance from the staff of ECN.
- the suppliers of silicon wafers (most of the major wafer producers).
- hospitality of Australian National University where part of the work was carried out.
- visits from and collaboration with: Fede Recart and Velia Rodriguez from University of Bilbao, Oyvind Mjoes from Technical University of Trondheim, Harold Dekkers of IMEC.
- collaboration with Stephan Riepe of FhG-ISE on the B-O defect.
- collaboration with Axel Schönecker of ECN and Armin Müller of Deutsche Solar on chapter 9.
- the use of NAA results by A. Kinomura and Y. Nakano (AIST and Kyoto University) through the collaboration with Daniel Macdonald of Australian National University.
- useful discussions with staff from other institutes and companies, in particular Tonio Buonassisi (University of California, Berkeley), Andres Cuevas (Australian National University, Canberra), Giso Hahn (University of Konstanz), Wolfgang Koch (KoSolCo GmbH), Erik Sauar (Renewable Energy Corporation, Oslo), Gaute Stokkan (Scanwafer, and Technical University of Trondheim).

Abstract

The TherMat II project investigated the relation between silicon material quality and solar cell efficiency, and the changes in material which occur as a result of high-temperature process steps.

Goals of the project were:
1. To find out whether the negative effects of extra impurities in the silicon wafer, e.g. due to the use of new feedstock, can be avoided.
2. To find out which extra impurities and defects are present in Si wafers which are made with modern high-throughput equipment and prototypes, and how these can be eliminated.
3. To look at the effect of short high-temperature process steps.

Important results of the project are
- New quantitative information on the presence of impurities, and new insight in the segregation phenomena occurring during crystallisation of silicon (chapter 1).
- New knowledge on measuring Fe in silicon (chapters 2 and 3).
- New insight in the relation between the doping of the silicon and the detrimental effect of impurities (chapters 4 and 5).
- Characterisation of the detrimental effect of boron-oxygen defect-pairs (chapter 6).
- Promising results to measure and characterise the passivation of defects with hydrogen, by monitoring interstitial Fe (chapter 7).
- Insight in the relation between ingot growth, Si material parameters and cell efficiency for standard processing (chapters 8 and 9).
- Improved gettering of impurities during emitter diffusion (chapter 10).

Four practical results are particularly noteworthy:
- Improvement of the thermal profile for gettering/diffusion, resulting in carrier lifetime increases of up to a factor 10;
- Understanding of the doping-dependence of carrier lifetime in Si, in particular leading to a proposal to use n-type doping for future lower-quality Si wafers;
- Quantification of (part of) the detrimental effect of oxygen (due to its interaction with boron) in mc-Si; and
- Results which open the way for a better characterisation of the passivation of defects with hydrogen, by monitoring interstitial Fe.

CONTENTS

INTRODUCTION

Solar cells based on multicrystalline silicon wafers accounted for more than 50% of the total PV production in 2002. The properties of solar cells produced from multicrystalline silicon (mc-Si) wafers show a significant variation, dependent on material properties. For example, in the ECN solar cell baseline a variation of over 10% is found in the efficiency of cells from current commercial wafers.
It is important to understand this variation, to relate it quantitatively to material properties, and to minimise it as much as possible. For one reason, it will obviously be attractive if PV producers can reproducibly manufacture products of a fixed quality.
Another reason for the importance of this project is that an increase of the variation in material properties seems unavoidable for the near future. The growth of the PV industry in the next ten years will largely be based on silicon solar cells. To enable the continued cost reduction of PV and growth of the PV industry, new silicon and wafer production techniques are being introduced. As a result, mc-Si wafers will present more complicated material properties and result in more variation in cell properties.

Therefore, the TherMat II project investigated the relation between silicon material quality and solar cell efficiency, and the changes in material which occur as a result of high-temperature process steps.

Goals of the project were
1. to find out whether the negative effects of extra impurities in the silicon wafer, e.g. due to the use of new feedstock, can be avoided.
2. to find out which extra impurities and defects are present in Si wafers which are made with modern high-throughput equipment or prototypes, and how these can be eliminated.
3. to look at the effect of short high-temperature process steps

The main results obtained in the project are summarised in the next section. Most of it has been described in publications for the open literature. Chapters 1-10 of this report consist of those publications and "preprints". The chapters are ordered as follows:
<u>Determination of impurities in silicon</u>
- new quantitative information on the presence of impurities, and new insight in the segregation phenomena occurring during crystallisation of silicon (chapter 1).
- new knowledge on measuring of the presence of Fe in silicon (chapters 2 and 3).

<u>Model studies of the effect of impurities and defects in silicon</u>
- new insight in the relation between the doping of the silicon and the detrimental effect of impurities (chapters 4 and 5).
- characterisation of the detrimental effect of boron-oxygen defect-pairs (chapter 6).
- promising results to measure and characterise the passivation of defects with hydrogen, by monitoring interstitial Fe (chapter 7).

<u>Relation between defects and cell efficiency</u>
- insight in the relation between ingot growth, Si material parameters and cell efficiency for standard processing (chapters 8 and 9).
- improved gettering of impurities during emitter diffusion (chapter 10).

CONCLUSIONS AND DISCUSSION

Highlights

The TherMat II project has resulted in a significant increase in knowledge, both of mc-Si and its behaviour under high-temperature processes, and of its characterisation techniques. Four practical results are particularly noteworthy:

- Improvement of the thermal profile for gettering/diffusion, resulting in carrier lifetime increases of up to a factor 10;
- Understanding of the doping-dependence of carrier lifetime in Si, in particular leading to a proposal to use n-type doping for future lower-quality Si wafers;
- Quantification of part of the detrimental effect of oxygen (due to its interaction with boron) in mc-Si; and
- Results which open the way for a better characterisation of the passivation of defects with hydrogen.

Recent improvements of cell processing at ECN have led to efficiencies which attract strong industrial attention. While these improvements are mainly due to other projects, the Thermat II project has at least contributed to understanding why certain process changes were successful.

Conclusions

In relation to the goals listed in the introduction, the conclusions of the Thermat II project are the following:

1. avoid negative effects of extra impurities

Several ways to reduce the effect of impurities were investigated. Useful approaches are: reduction of oxygen in the silicon wafer; using improved thermal profiles for gettering/diffusion; optimising the resistivity of the wafers; and changing to cells based on n-type silicon wafers instead of p-type silicon wafers. The first point is an opportunity for wafer manufacturers. The last three are an opportunity for solar cell manufacturers.

2. which impurities and defects are present, and how can they be eliminated

Iron and oxygen are found to be the major impurities where it concerns the charge carrier lifetime in wafers (the usual measure of material quality). Neutron activation profiles also showed the presence of Cu and Co, and provided ambiguous indications for other impurities. In addition, crystal defects in interaction with impurities also play an important role in the reduction of quality of wafers. Especially precipitates at crystal defects are important.

Oxygen and crystal defects can be reduced by appropriate crystallisation conditions and using appropriate materials in crystallisation furnaces. This is deduced from the fact that certain wafer manufacturers perform systematically better on these aspects than others. However, they can probably never be completely eliminated in multicrystalline wafer manufacturing. This report indicates to which feasible level oxygen should be eliminated by wafer manufacturers. This report also shows and explains how impurities can be removed from wafers by gettering.

3. the effect of short, high-temperature process steps

This is related to the elimination of impurities in point 2. Thermal steps will dissolve precipitates, and cause impurities to diffuse. When combined with gettering this can result in reduction of impurities, but this depends on the exact thermal parameters. In the experiments on gettering in this project it turns out that lower temperature and longer process steps are better than short, high-temperature process steps, at least for the case of phosphorous diffusion/gettering.

Characterisation techniques

Monitoring the changes in silicon wafers under thermal processes requires sensitive and well-understood characterisation techniques. Therefore quite some attention in this project focussed on elaboration of characterisation techniques. It turned out that much was still unknown about characterisation of iron in silicon, even though iron may well be the most abundant and important impurity. Therefore lifetime measurements and measurements of iron concentration were further developed in the project.
Hydrogen-passivation of impurities and/or crystal defects can improve silicon wafer quality significantly. A significant effort in this project was spent on trying to characterise and monitor the hydrogen in-diffusion into a silicon wafer. This turned out to be very difficult. Several potential techniques failed at the required level of sensitivity. Nevertheless, a technique based on hydrogen-passivation of interstitial iron was developed and looks very promising.

The following techniques for multicrystalline silicon characterisation which are relevant for understanding of cell performance were used and/or made available for research at ECN:
1. resistivity measurement to establish background dopant concentration
2. Fourier transform infra-red (FTIR) measurement of the concentration of dissolved oxygen and carbon impurities
3. carrier lifetime measurement by quasi-steady state photoconductivity (Sinton) and modulated free carrier absorption (MFCA)
4. FeB concentration derived from carrier lifetime measurements
5. Neutron Activation Analysis (NAA) of total impurity concentrations
6. defect etch and etch pit count (qualitative)

Of these techniques, especially technique 4 was strongly extended beyond the current state of the art. Also the influence of oxygen (technique 2) was considered in more detail than in other or previous studies. Advances were made in the use of MFCA, in particular on modelling.
Individually, the above techniques were known to be useful for analysis of mc-Si. Their use in combination had been lacking, until the Silke project (recently funded by Novem under contract no. 146.110-020.1 and executed by ECN). Also, their application to a representative set of wafers from normal quality ingots, instead of undefined or unusual mc-Si wafers, is rather uncommon in literature. These are two of the important aspects of the TherMat II project.
An important issue which cannot be easily probed directly is the formation and dissolution of small precipitates. By using and interpreting lifetime, FeB, and NAA measurements in combination, however, and by varying thermal process parameters, new insight was obtained on this subject.

Cost reductions and improvement of cell efficiency

On the basis of the results of this project, the following cost reductions are possible:

a. Improved yield of conventional ingots: cost reduction approx. 0.04 €/Wp.
Publications from this project have been used by Sinton Consulting Inc. for an instrument for improved characterisation of mc-Si ingots (ch. 2,3,8,9). According to Sinton the possible increase of yield from ingots is more than 10% (Proceedings European Photovoltaic Specialists Conference, Paris 2004, p. 520). Since the cost of crystallisation of an ingot is about 30 €/kg, which is equivalent to 0.4 €/Wp, an increase of yield by 10% corresponds to a cost reduction of approx. 0.04€/Wp.
The practical introduction of this technique can be immediately.

b. Improved cell efficiency: subject of ongoing research.
At ECN, changes in emitter diffusion and gettering have resulted in an cell effiency improvement of 0.2 to 0.3%$_{abs}$. Research on gettering in this project has contributed to understanding the reasons for this improvement (ch. 10). The results of ch. 10 provide possibilities for further

improvement of cell efficiency and yield. In particular for low quality wafers, it is expected that the cell efficiency can improve strongly, e.g. by 1 to 2 $\%_{abs}$. This is currently being investigated. The practical introduction of this technique can be immediately.

This project *contributes to* the following cost reductions:

a. Use of metallurgical solar grade silicon as feedstock for solar cells: cost reduction approx. 0.2 €/Wp.
This project has contributed to a better understanding of defects, electrical activity of defects, and defect-elimination in silicon wafers (ch. 1, 4-10). With this understanding, the project has contributed to the chances of employing cheap metallurgical solar grade silicon for solar cells in the future. The accompanying cost reduction is approx. 0.20 €/Wp (a combination of a specific Si-consumption of 10 g/Wp, and a reduction of the price of Si by 20 €/kg).
Practical introduction of metallurgical silicon feedstock on a larger scale: estimated between 2007 and 2010.

b. Improved results with ribbon silicon wafers: cost reduction approx. 0.075 €/Wp.
ECN has a large effort on introduction of so-called "RGS"-ribbon wafers for solar cells. It is expected that such ribbon wafers can provide a cost reduction of 0.50 €/Wp. This project provides ideas for several improvements for RGS-wafers and -cell technology, in particular improved gettering and the use of n-type silicon. It is impossible to calculate the improvement exactly with the present state of technology, but it seems reasonable to expect an improvement of cell efficiency of 15%, i.e. a cost reduction of 0.075 €/Wp.
Practical introduction of RGS on a larger scale: estimated between 2006 and 2008.

RECOMMENDATIONS AND FOLLOW-UP

The ideas and innovations from this project can be elaborated in several ways. In the cases below, actual efforts are already going on:

a. Multicrystalline cell process based on n-type silicon
National project NBEST (supported by SenterNovem).
European project NESSI.
Smaller activities in national and international RGS-projects.
Proposal for a European R&D project to combine n-type metallurgical feedstock and cell technology, with a consortium of several important wafer, cell, and metallurgical companies.

b. Improved gettering
This is currently being investigated at ECN with own funding, and in collaboration with a wafer manufacturer. Depending on cell results, this effort may be elaborated.

c. International network, participation in Centre of Excellence
ECN participates in a proposal on a centre of excellence for solar energy systems, specifically on 'defect engineering', with an intended international collaboration and exchange of researchers.

d. Application of knowledge and characterisation and modelling tools in projects on high-efficiency cell technology.
The knowledge obtained in this project is applied in several research projects of ECN on high-efficiency solar cells, feedstock, etc.

1. TRANSITION METAL PROFILES IN A MULTICRYSTALLINE SILICON INGOT

Daniel Macdonald and Andrés Cuevas

Department of Engineering, Faculty of Engineering and Information Technology, The Australian National University, Canberra, ACT 0200, Australia

A. Kinomura

National Institute of Advanced Industrial Science and Technology (AIST), 1-1-1 Umezono, Tsukuba, Ibaraki 305-8568, Japan

Y. Nakano

Kyoto University Research Reactor Institute, Kumatori-cho, Sennan-gun, Osaka 590-0494, Japan

L. J. Geerligs

ECN Solar Energy, PO Box 1, NL-1755 ZG Petten, The Netherlands

The concentrations of transition metal impurities in a photovoltaic-grade multicrystalline silicon ingot have been measured by Neutron Activation Analysis. The results show that the concentrations of Fe, Co and Cu are determined by segregation from the liquid to solid phase in the central regions of the ingot. This produces high concentrations near the top of the ingot, which subsequently diffuse back into the ingot during cooling. The extent of this back-diffusion is shown to correlate to the diffusivity of the impurities. Near the bottom, the concentrations are higher again due to solid-state diffusion from the crucible after crystallization has occurred. Measurement of the interstitial Fe concentration along the ingot shows that the vast majority of the Fe is precipitated during ingot growth. Further analysis suggests that this precipitation occurs mostly through segregation to extrinsic defects at high temperature, rather than through solubility-limit driven precipitation during ingot cooling.

Paper acceptebed for publication in Journal of Applied Physics, 2005.

I. INTRODUCTION

Transition metal impurities are detrimental to crystalline silicon solar cells, but are relatively common in photovoltaic-grade materials. They cause reduced solar cell conversion efficiencies through increased carrier recombination, whether they are present as isolated point-like impurities, or as precipitates. The purpose of this work is to study the concentration profiles of some common metallic impurities along the length of a standard directionally-solidified multicrystalline silicon ingot grown for solar cell production.

The concentrations of such impurities are generally below 10^{15} cm^{-3}, and as such cannot be detected by physical techniques such as Secondary Ion Mass Spectroscopy. Deep-Level Transient Spectroscopy and other electrical techniques are sensitive enough, but fail to give quantitative information on how many atoms are incorporated in precipitates. Here we have used Neutron Activation Analysis (NAA), a technique which has been successfully applied to such material in the past[1,2], to reveal the total concentrations of Fe, Co, Cu, Ag, Au, Zn and Cr. The resulting concentration profiles are modeled using a simple segregation model, which explains the data well in regions which are not influenced by further diffusion of impurities after crystallization is complete.

NAA data does not provide any information regarding the chemical state of the impurities – they may be present as point-like impurities, or as precipitates. For the case of Fe we have also determined the concentration of electrically active interstitial Fe atoms via carrier lifetime measurements before and after dissociation of iron-boron pairs. The results reveal that the vast majority of the Fe must be precipitated, although both the interstitial and precipitated Fe concentrations have a similar shape along the ingot length. This latter fact suggests that the precipitation is chiefly driven by energetically-favored segregation to extrinsic defects at high temperature, rather than the deceasing solubility limit during cooling. This in turn has implications for the chemical form of the precipitates, and their behavior during solar cell processing.

II. EXPERIMENTAL METHODS

The multicrystalline ingot analyzed was a standard, boron-doped (nominally 1Ωcm) ingot from a commercial process for solar cell production. Crystallization occurred from bottom to top, resulting in a vertical, columnar grain structure. The large square-based ingots are then sawn vertically into ‘bricks’, which are in turn sawn horizontally into 12.5×12.5 cm wafers for solar cell processing. Typically, thin slabs from the top and bottom of the bricks are removed before wafering, as these sections have high impurity concentrations due to solid-state diffusion

from the crucible at the bottom, and from impurity segregation at the top. In this case however, the bottom and top sections were retained in order to monitor the entire vertical impurity profile.

The chosen brick was taken from the center of the ingot in order to avoid contamination from the crucible walls, which may extend over a few centimeters[3,4]. In addition, all measurements were performed on wafer sections that were vertically aligned, meaning that cross sections of the same columnar grains were included. This should minimize the impact of lateral variations in the metal content of the ingot.

A. Neutron activation analysis

Wafers for NAA were selected at 4%, 10%, 20%, 42% and 98% of the total ingot length, as measured from the top, with the total ingot height being approximately 350mm. A small section, approximately 8 cm^2 of each 300 micron thick wafer, was subjected to NAA, giving a sample volume of around 0.25 cm^3. The analyzed wafer area is large enough to include a representative average of grain boundaries and intra-grain regions, which is important considering that metal precipitates occur much more frequently at grain boundaries[1,5].

Prior to NAA, the wafer sections were cut, chemically cleaned, and then etched in a HF/HNO_3 solution to a depth of approximately 15 microns per side to remove saw-damage and surface contamination. The wafers were then chemically cleaned again in fresh solutions to minimize possible re-plating of dissolved impurities.

The samples were then subject to neutron activation for 190 hours during 3 weeks with a nominal thermal-neutron flux of 4.7×10^{13} n/cm^2s at the Research Reactor Institute, Kyoto University. The resulting gamma rays emitted by the decaying nuclei were monitored by a pure Ge detector, firstly for 1 hour after a cooling time of about 4 days, then again for 24 hours after one month. The measurement was, in principle, based on the monostandard method[6] using ^{197}Au as a single standard. Sensitivities of Ag, Co, Zn, Cu and Fe were calibrated in advance by using samples with known concentrations of the relevant isotopes. These standard samples were prepared by ion-implantation into Si wafers for the first 5 elements, and by deposition of a thin metallic film on Si for the case of Fe (since the relevant isotope ^{58}Fe has a natural abundance of only 0.3%). As a result, the uncertainty in the NAA measurements was substantially improved, as indicated by the error bars in Figs 2 and 3.

B. Interstitial iron measurement

To supplement the NAA results, the concentration of interstitial Fe (Fe_i), as opposed to the total Fe concentration, was measured on wafers from the same brick. This was achieved using a technique based on the optical dissociation of FeB pairs, which causes a characteristic change in

the carrier diffusion length, or lifetime[7,8]. This technique was originally developed for use with Surface PhotoVoltage (SPV) diffusion length measurements in low-injection[7], but has recently been extended to arbitrary injection[8], meaning other lifetime measurement techniques can be used.

In this work, injection-dependent carrier lifetimes were measured using the quasi-steady-state photoconductance technique (QSSPC)[9], and values were extracted at an excess carrier concentration of 10^{15}cm^{-3}. Knowledge of the change in lifetime after FeB pair dissociation by illumination at this excess carrier density, coupled with the dopant concentration, allows very sensitive determination of the concentration of Fe_i.[8] A further benefit of measuring the injection-dependence of the carrier lifetimes is that it provides independent confirmation that the changes due to illumination are indeed caused by Fe_i, as opposed to other possible light-induced changes, such as charging of the nitride layer,[10] boron-oxygen complexes,[11] or breaking of Cu_s-Cu_i pairs.[12] It has been shown that, for the case of Fe_i and FeB pairs, such injection-dependent lifetime curves display a characteristic 'crossover' point at an excess carrier density between 1-2×10^{14}cm^{-3}. We observed the presence of this crossover point in all samples studied here.

Surface passivation was achieved by plasma-enhanced chemical vapor-deposition of SiN films on both wafer surfaces, after etching and cleaning.[13] The QSSPC technique measures an area of several square centimeters, and thus provides an 'average' of the Fe_i concentration across several grains. This can cause an overestimation (by up to a factor of 2) of [Fe_i] if the lifetime varies considerably between grains.[8] Nevertheless, this error is small in comparison to the changes in [Fe_i] observed along the ingot length.

It is essential that almost complete pairing and dissociation are ensured for the two measurements to enable the *total* Fe_i concentration to be determined. Initial measurements with the Fe_i in the paired state were performed after at least 3 hours re-pairing in the dark. For 1Ωcm material this ensures more than 98% pairing. In this study, the illumination used to break the FeB pairs was white light with intensity of approximately 0.7 W/cm^2 for a duration of 20 seconds. This is sufficiently intense to ensure complete dissociation even in wafers with relatively low lifetimes.[14] The samples were clamped to a cooled Al block during illumination to minimize heating.

The slight delay between illumination and measurement allows some re-pairing, so several measurements were taken at varying time intervals to allow extrapolation to the initial state of almost complete dissociation. This is shown in Fig. 1 for a sample 13% from the top of the ingot. The total Fe_i concentration was determined to be 4.2×10^{11}cm^{-3}. The exponential fit gave a characteristic re-pairing time of 620 seconds. This value is within a factor of 2 of the expression from Zoth and Bergholz[7], which gives a re-pairing time of 1100 seconds for this 0.95Ωcm sample at an assumed temperature of 35°C. This fairly small disagreement will be the subject of

a future publication. In figure 1, measurements for 20 and 40 seconds illumination are shown to give the same result, indicating that the dissociation process was complete in both cases.

III. NAA RESULTS AND DISCUSSION

The NAA results for Fe, Co and Cu are shown in Fig. 2, as well as the boron concentration measured via the dark conductance of the wafers. The NAA results for Cr, Zn, Ag and Au are plotted in Fig. 3. For all of these impurities, the measured concentrations are well below their respective solid solubility limits near the melting point of silicon.[15] Due to the qualitative difference between the profiles of the first set of metals and the second, they are discussed separately below.

A. NAA results for Fe, Co and Cu

For Fe, Co and Cu, the concentration profiles along the ingot length show similar trends. In the central regions of the ingot, their concentrations are low. There is a strong increase towards the top of the ingot due to segregation into the molten phase, while the sharp increase at the bottom is probably due to solid-state in diffusion from the crucible after solidification. Considering that the bottom is the first part to crystallize, there is ample time at high temperature for this to occur (tens of hours generally).

The concentration of impurities incorporated into the solid phase C_S during crystallization, is given by $C_S=k_0C_I$ where k_0 is the equilibrium segregation coefficient and C_I the concentration of impurities at the solid/liquid interface.[16] The value of C_I may be very different from the concentration in the bulk liquid C_L due to imperfect mixing. In such cases the effective segregation coefficient k_{eff} is used: $C_S=k_{eff}C_L$, where k_{eff} depends on the growth rate v, the diffusivity of the impurities in the molten phase D, and the boundary layer thickness δ :

$$k_{eff} = \frac{k_0}{k_0 + (1-k_0)\exp(-v\delta / D)}. \qquad (1)$$

The boundary layer thickness approximates the width of the region near the interface in which no convection or mixing currents occur. The critical point is whether or not the impurities are able to diffuse out of the static boundary layer, and into the bulk melt, before being overtaken by the advancing crystallization front.

Assuming a fixed volume of solidifying liquid, as occurs for multicrystalline silicon growth, gives rise to the Scheil equation:[17,18]

(2)

$$C_S = k_{eff} C_0 (1 - f_s)^{k_{eff} - 1}$$

where C_0 is the initial concentration in the liquid and f_S the solidified fraction.

This expression describes the distribution of boron in the ingot quite well, as shown in Fig. 2, using k_{eff} = 0.65. This is a little lower than the literature value for k_0 of 0.8.[19] For effective segregation coefficients less than approximately 0.05, the *shape* of the impurity profile is indistinguishable, although for smaller values the *magnitude* is reduced for a given initial concentration in the melt. This reflects the fact that for low segregation coefficients, the shape of the profile is governed entirely by the almost complete ejection of impurities into a decreasing melt volume.

Fig. 2 shows an attempt to fit the Scheil expression to the measured Fe concentration, using $k_{eff} < 0.05$. In this case the data is distorted at the top and bottom by solid-state diffusion during post-crystallization cooling. Nevertheless, the model is in reasonable agreement in the upper part of the ingot. The equilibrium segregation coefficient for Fe is reported[20,21] as $k_0 = 5 - 7 \times 10^{-6}$. This would imply an initial concentration of Fe in the melt of 2×10^{18} cm^{-3}! This is extremely unlikely, and may be explained by incomplete mixing in the molten phase, producing a much larger segregation coefficient than the equilibrium value. It is also possible that the effective segregation coefficient is increased by rapid precipitation of Fe at extended defects during crystallization, as discussed in Section IV.

Applying the Scheil equation with $k_{eff} < 0.05$ to the data for Co and Cu results in a poorer fit. Although they show the same trend as for Fe, i.e. they increase towards the top, this increase is much greater than is possible with the Scheil equation. This deviation may be due to solid-state diffusion back into the ingot after crystallization is complete.

The extent of this back-diffusion will be determined by the diffusion length of the respective impurities during cooling. This is in turn determined by the cooling rate and the diffusivity at each temperature. Since the cooling rate is not well known in this case, nor are the diffusivities known for the whole temperature range, it is difficult to model this back-diffusion accurately.

Nevertheless, a simple evaluation is instructive. The Scheil equation with $k_{eff} < 0.05$ was fitted to the lowest measured data point for each impurity. The ratio of the *measured* concentration to this modeled curve was then determined at 4% below the top of the ingot. This should approximately represent the extent of back-diffusion. The results are plotted in Fig 4 against the normalized square root of the diffusivity for Fe, Co and Cu in silicon at 950°C (a temperature at which the diffusivity is known for all three[15]). While this does not provide a precise simulation of the back-diffusion process, the figure nevertheless shows a clear correlation between the extent of back-diffusion and the diffusivity for each impurity. This clearly indicates that the deviation from the segregation model near the top of the ingot is due to

solid-state back-diffusion. In the case of Cu, Fig. 2 shows that the back-diffusion extends more than 10% of the ingot height, a distance of more than 3 cm. As an order of magnitude approximation for the cooling period, the diffusion length[15] of Cu in silicon at 1000°C for 10 hours is around 2 cm, in approximate agreement.

B. NAA results for Cr, Zn, Ag, and Au

Figure 3 shows the NAA results for Cr, Zn, Ag and Au. They show relatively flat profiles, and lack the characteristic increase at the bottom and top of the ingot due to post-crystallization contamination and segregation. In all cases the NAA spectra were clearly identified, and the uncertainties in each measurement are quite small, being much less than the apparently random fluctuations in the data. This suggests the possibility of surface contamination. Contamination levels in the range of 10^{10}-10^{11} cm^{-2} would be sufficient for Ag, Cr and Zn, while values as low as 10^{8} cm^{-2} are all that is required for the amount of Au detected.

However, it is worthwhile considering if such flat profiles can possibly occur through segregation for metals with very small equilibrium segregation coefficients (k_0 < 0.0001 for each of these metals[20,21]). Firstly, in relation to the lack of concentration peaks at the bottom of the ingot, in-diffusion from the crucible would not actually be expected for Zn, Ag and Au, since they have much lower diffusivities in the solid state than Fe, Co or Cu. This is due to the fact that they diffuse via the kick-out mechanism[15,22]. Cr, however, diffuses interstitially, and its diffusivity is only a little lower than that of Fe. Hence some in-diffusion of Cr from the crucible would be expected, if it were present there in high enough concentrations.

Regarding the flat profiles throughout the rest of the ingot, this would require k_{eff} values close to unity. According to Equation 1, this can occur through changes in the values of the growth rate, the boundary layer thickness or the diffusivity of the impurities in the melt. Since the first two must be the same for all species, only changes in the diffusivity can increase k_{eff} for some impurities relative to others. However, modeling using equations 1 and 2, with realistic growth rates in the range 2-20 microns per second[23], reveals that this would require a diffusivity for Cr, Au, Ag and Zn at least an order of magnitude smaller than for Fe, Co and Cu. This seems unlikely, since the diffusivities of different impurities in molten silicon are quite similar, despite enormous differences in the solid state.[19,24] For example, impurities as diverse as B, P, Al, O, C, Fe and Cu have diffusivities in molten silicon[19,24] that fall within the range 0.5 - 7×10^{-4} cm^2s^{-1} (for Fe and Cu a value of 2×10^{-4} cm^2s^{-1} has been suggested[24]). Although values are not known for Cr, Zn, Ag or Au, they would probably also fall within this range.

In conclusion then, although it is not possible to definitely rule out the profiles for Cr, Zn, Ag and Au reflecting concentrations in the bulk of the wafers, it seems the most likely explanation is surface contamination. Such surface contamination has been reported for Cr via

re-plating of the metal onto the silicon surface during wet processing.[15] It is worth bearing in mind that the lower values for Fe, Co and Cu may also be affected by surface contamination. This may be the reason for the slightly higher measured values for Fe and Co at 40% from the ingot top, where solid-state diffusion should not occur, in comparison to the Scheil equation fit.

IV. TOTAL AND INTERSTITIAL IRON RESULTS

For the case of Fe it is possible to compare the total Fe concentration [Fe] as measured by NAA to the interstitial Fe concentration [Fe_i] from lifetime measurements before and after dissociation of FeB pairs. The results are shown in Fig. 5. Data for the interstitial Fe concentration is not available at the very top and bottom of the ingot because the carrier lifetimes there are too low to allow complete FeB pair dissociation.

The striking feature is that the interstitial Fe data also follows the Scheil equation, apart from a deviation near the top of the ingot, presumably due once again to solid-state back-diffusion. This data is in qualitative agreement with recently published results for similar multicrystalline ingots, using the same Fe_i detection technique.[25,26] Another observation is that the vast majority of the Fe is not in interstitial form, and must therefore be present as precipitates. The results presented here allow some speculation as to how these precipitates form.

Since Fe only precipitates heterogeneously[15] (unlike Cu or Co), the precipitates must form at extrinsic defects in the material such as grain boundaries and dislocations. There are two distinct mechanisms which can influence the amount of precipitated Fe at a given point in the ingot after cooling. These have been referred to as 'relaxation' and 'segregation' gettering[27,28], the latter word a reference to the fact that the extrinsic defects act as internal gettering sites. These two mechanisms are discussed in turn in relation to our measurements.

A. Relaxation mechanism

In the 'relaxation' process the precipitation is driven by the decreasing solid solubility limit during the cooling of the ingot. Just below the melting point of Si, the solubility[15] of Fe is above 10^{16} cm^{-3}, well above any of the measured values here. Hence all of the Fe is initially dissolved in the solid-state. As the ingot cools after crystallization is complete, the solubility limit also decreases until it reaches the local Fe concentration. If the excess Fe atoms are still diffusive enough, they can reach extrinsic defects and precipitate. Eventually, the diffusivity becomes too low and the remaining non-precipitated Fe is frozen in the interstitial state. The determining factors for the final concentration of interstitial Fe under the relaxation process are then the *cooling rate* and the *density of extrinsic defects*. If these are the same everywhere in an ingot,

then the final value of [Fe_i] should be constant, irrespective of variations in the initial Fe content.

Recent numerical simulations[29] of multicrystalline silicon ingot growth have shown that most parts of an ingot cool at approximately the same rate below 1200ºC (at which temperature the solubility of Fe is still above $10^{16}cm^{-3}$), except for the very top, bottom and edges. Similarly, the density of extrinsic defects, the most important of which are probably grain boundaries and dislocations, also increases near the very top, bottom and edges, but is generally fairly constant throughout the central regions. It therefore seems unlikely that the relaxation mechanism explains the observed [Fe_i] trend in the central region. According to the relaxation model, and assuming an effective segregation coefficient k_{eff} similar to the equilibrium value[20,21] of k_0 = 5 - 7×10^{-6}, then the starting concentration of Fe in the melt would be as high as 2×10^{18} cm^{-3}, which is also unlikely.

B. Segregation mechanism

The fact that the two sets of Fe profiles are observed to be parallel hints that maybe the concentration of interstitial Fe is actually formed at higher temperatures, rather than during the cool-down. This can occur via the so-called 'segregation' mechanism, in which there is not only segregation from the liquid melt to the bulk solid, but also to extrinsic defects within the solid. The precise mechanism of the segregation to extrinsic defects is unclear – it may occur either directly from the liquid phase, or after a brief incorporation in the bulk solid. In either case, the system can be thought of as equilibrium segregation occurring between *three* phases, (the third phase being the extrinsic defects), rather than just two. Segregation to extrinsic defects is driven by lower free energies for metal atoms where the lattice is distorted, as compared to regions of perfect crystal structure.[27,28] Note that this implies that precipitation can proceed even when the dissolved concentration is well below the solubility limit. This phenomenon has been observed recently for Fe in defected silicon.[27,28]

Consider the case when the crystallization occurs slowly enough to allow the three-phase segregation processes to equilibrate. Assume also that segregation to the extended defects occurs primarily from the solid phase, rather than directly from the liquid phase. Given that typical crystallization velocities are in the range of 5-10 μm/s in the central part of the ingot[23], and that the diffusion length of Fe atoms in the solid phase near the melting point is around 30 μm in a time of 1 second, then equilibration will occur in regions where the average distance between extrinsic defects is of a similar distance (30 μm) or less. For dislocations, this corresponds to an areal dislocation density of approximately 10^5 cm^{-2}.

Multicrystalline silicon materials commonly have numerous regions with dislocation densities above 10^6 cm^{-2}.[30,31] Hence it is likely that in such regions the segregation of Fe to extrinsic defects will deplete the Fe concentration in the solid phase near the interface, resulting in greater incorporation from the liquid phase, and hence a larger effective segregation coefficient. On the other hand, if the distance between extrinsic defects is large, the segregation process will not occur until some time after the crystallization front has passed, and will not result in increased incorporation from the melt. This implies that the total Fe concentration in highly dislocated regions would be much higher than in other parts of an ingot.

The starting concentration of Fe in the melt can be estimated within the framework of this segregation mechanism. Assume that in highly dislocated regions the three phases are in equilibrium, and therefore there is increased segregation from the melt in those regions. If we also assume that the Fe precipitated in this way dominates the total Fe concentration, then the relevant concentration in the solid phase for determining the starting concentration in the melt is the *interstitial* concentration, rather than the *total* concentration. Assuming an effective segregation coefficient k_{eff} similar to the equilibrium value[20,21] of $k_0 = 5 - 7\times10^{-6}$, the starting concentration of Fe in the melt would then be around 1×10^{16} cm^{-3}, compared with 2×10^{18} cm^{-3} for the relaxation mechanism. This seems a more reasonable value, although it may still be too high considering that incomplete mixing in the melt may increase the effective segregation coefficient from its equilibrium value. If such a high starting concentration did occur, it is unlikely to come solely from the starting polysilicon material, suggesting contamination from handling or from the crucible during the melting stage.

Reflecting these processes mathematically, it is possible to express the effective segregation coefficient between liquid and solid (excluding precipitated atoms) $k_{eff} = C_S/C_L$ in terms of segregation coefficients between the liquid phase and extrinsic defects $k_{L/ED}$ and between extended defects and the bulk solid phase $k_{ED/S}$, such that $k_{eff} = k_{L/S} = k_{L/ED}\, k_{ED/S}$. This model naturally leads to a situation where the interstitial and dissolved Fe concentrations both follow segregation-model curves, as observed in Fig 5. Furthermore, the data in Fig. 5 allows us to estimate $k_{ED/S} \approx 0.005$. If we assume $k_{eff} = k_{L/S}$ is approximately equal to the equilibrium value k_0 from the literature, this implies that $k_{L/ED} \approx 0.001$. This value is below 0.05, for which different curves are indistinguishable in shape in a plot such as Fig 5. This is in agreement with the observation that the total Fe curve does indeed follow the Scheil equation with $k_{eff} < 0.05$.

The results suggest that the precipitated and interstitial Fe concentrations as formed at high temperatures are largely preserved during the cooling down of the ingot. This could occur if $k_{ED/S}$ itself is relatively temperature independent, or if there are kinetic barriers against further precipitation or dissloution of Fe.

It is instructive to note that the ratio of interstitial to total Fe concentration, or in other words $k_{ED/S}$, is quite constant in the central regions of the ingot. This is consistent with the fact that the density of extrinsic defects is roughly constant in this region. This value may increase significantly towards the edges and ends of the ingot due to an increase in the extrinsic defect concentration. It could also vary considerably for different growth processes. In recent experiments with segregation of Fe from monocrystalline silicon to a thin film of polycrystalline silicon (at temperatures between 1050 and 1200 C), Istratov *et al.* found values for $k_{ED/S}$ of 0.06 and 0.4.[27]

C. Relative importance of the two mechanisms

It is likely that in grains with high densities of dislocations, above approximately 10^5 cm^{-2}, the segregation mechanism would be dominant, and may act quickly enough to allow depletion of the solid-phase near the interface, and hence result in increased incorporation into the solid phase. This would also occur if segregation to extended defects proceeded directly from the melt, rather than via the solid phase.

However, in large grains of high crystal quality, with sparsely distributed extrinsic defects, such depletion near the liquid/solid interface will not occur. In these regions, segregation precipitation will proceed on a slower time scale determined by the extrinsic defect density. In such regions the relaxation mechanism may also play an important role in precipitation. It is therefore possible that there is a mixture of both segregation and relaxation precipitation occurring during ingot growth. However, the fact that both the interstitial and precipitated Fe profiles are parallel suggests that the segregation mechanism is responsible for the vast majority of the Fe precipitation.

A further consequence of the segregation versus relaxation mechanism relates to the chemical form of the precipitates. Since under the segregation mechanism the precipitates are created at relatively high temperatures, just below the melting point, they are probably largely in the form of α-$FeSi_2$, which forms above approximately 920°C.[32] These silicides have large binding energies, and are very difficult to dissolve during subsequent solar cell processing. This may explain the observation that highly dislocated regions do no respond well to phosphorus gettering.[30,31] On the other hand, for the relaxation precipitation mechanism, a significant proportion may occur as β-$FeSi_2$, which are formed[33] below 800°C and therefore more easily dissolved and removed by gettering.

V. CONCLUSIONS

The total concentrations of Fe, Co and Cu along the length of a photovoltaic-grade multicrystalline silicon ingot appear to be determined by segregation from the liquid to the solid phase in the central region of the ingot. Near the bottom the concentrations are higher due to in-diffusion in the solid state from the crucible. Near the top, the segregated impurities diffuse back into the solid ingot during cooling. The extent of this back-diffusion is clearly related to the diffusivity of each impurity. For Cu, the back-diffusion extends over several centimeters. Maximum concentrations of 3.8×10^{14}, 3.7×10^{12} and 2.8×10^{15} cm^{-3} were detected near the top of the ingot for Fe, Co and Cu respectively.

For the case of Fe, the interstitial Fe concentration was measured in addition to the total Fe concentration. The results indicate that only approximately 1 in 200 Fe atoms occur interstitially. However, the two profiles followed similar curves, indicating that the majority of the Fe precipitation is driven by energetically-favored segregation to extrinsic defects at high temperature, rather than by the decreasing solubility limit during ingot cooling.

The authors are grateful to JS Williams for coordinating the joint research between ANU and AIST, and to T. Buonassisi for enlightening discussions. This work has been carried out in part under the Visiting Researcher's Program of the Kyoto University Research Reactor Institute. L.J.G. acknowledges the assistance of The Netherlands Agency for Energy and the Environment. D.M. and A.C. acknowledge the support of the Australian Research Council.

[1] A. A. Istratov, T. Buonassisi, R. J. McDonald, A. R. Smith, R. Schindler, J. A. Rand, J. P. Kalejs and E. R. Weber, *Journal of Applied Physics* **94**, 6552 (2003).

[2] D. Macdonald, A. Cuevas, A. Kinomura and Y. Nakano, in *Proceedings of the 29th IEEE Photovoltaic Specialists Conference,* New Orleans, LA (IEEE, New York, 2002), p. 285.

[3] M. Acciarri, S. Binetti, S. Ratti, C. Savigni, S. Pizzini, F. Ferrazza and D. Margadonna, in *Proceedings of the13th European Photovoltaic Solar Energy Conference,* Nice, France (H S Stephens and Associates, Felmersham, UK, 1995), p. 1336.

[4] M. Rinio, C. Ballif, T. Buonassisi and D. Borchert, in *Proceedings of the 19th European Photovoltaic Solar Energy Conference,* (Paris 2004), to be published.

[5] S. A. McHugo, A. C. Thompson, A. Mohammed, G. Lamble, I. Perichaud, S. Martinuzzi, M. Werner, M. Rinio, W. Koch, H. U. Hoefs and C. Haessler, *Journal of Applied Physics* **89**, 4282 (2001).

[6] J. I. Kim, *J. Radioanal. Chem.* **63**, 121 (1981).

[7] G. Zoth and W. Bergholz, *Journal of Applied Physics* **67**, 6764 (1990).

[8] D. Macdonald, L. J. Geerligs and A. Azzizi, *Journal of Applied Physics* **95**, 1021 (2004).

[9] R. A. Sinton and A. Cuevas, *Applied Physics Letters* **69**, 2510 (1996).

[10] A. G. Aberle, *Crystalline Silicon Solar Cells: Advanced Surface Passivation and Analysis,* (University of New South Wales, Sydney, 1999).

[11] J. Schmidt and A. Cuevas, *Journal of Applied Physics* **86**, 3175 (1999).

[12] W. B. Henley, D. A. Ramappa and L. Jastrezbski, *Applied Physics Letters* **74**, 278 (1999).

[13] M. J. Kerr and A. Cuevas, *Semiconductor Science and Technology* **17**, 166 (2002).

[14] L. J. Geerligs and D. Macdonald, *accepted for publication in Applied Physics Letters* (2004).

[15] K. Graff, *Metal Impurities in Silicon-Device Fabrication, Springer Series in Material Science* (Springer-Verlag, Berlin, 2000).

[16] J. R. Carruthers and A. F. Witt, in *Crystal Growth and Characterization*, edited by R. Ueda and J. B. Mullin (North-Holland, Amsterdam, 1975), p. 107.

[17] E. Scheil, *Z. Metallk.* **34**, 70 (1942).

[18] R. A. Brown and D. H. Kim, *Journal of Crystal Growth* **109**, 50 (1991).

[19] H. Kodera, *Japanese Journal of Applied Physics* **2**, 212 (1963).

[20] J. R. Davis, A. Rohatgi, R. H. Hopkins, P. D. Blais, P. Rai-Choudhury, J. R. McCormick and H. C. Mollenkopf, *IEEE Transactions on Electron Devices* **27**, 677 (1980).

[21] H. Lemke, in *Semiconductor Silicon/1994*, edited by H. R. Huff, W. Bergholz and K. Sumino (The Electrochemical Society, New Jersey, 1994), p. 695.

[22] D. Grünebaum, T. Czekalla, N. A. Stolwijk, H. Mehrer, I. Yonenaga and K. Sumino, *Applied Physics A: Solids and Surfaces* **53**, 65 (1991).

[23] I. Steinbach, M. Apel, T. Rettelbach and D. Franke, *Solar Energy Materials and Solar Cells* **72**, 59 (2002).

[24] G. F. Wakefield, *Journal of the Electrochemical Society* **127**, 1139 (1980).

[25] R. A. Sinton, in *Proceedings of the 19th European Photovoltaic Solar Energy Conversion Conference,* (Paris 2004), to be published.

[26] L. J. Geerligs, in *Proceedings of the 3rd World Conference on Photovoltaic Solar Energy Conversion,* Osaka (WCPEC-3, 2003), p. 1044.

[27] A. A. Istratov, T. Buonassisi, W. Huber and E. R. Weber, in *Proceedings of the 14th Workshop on Crystalline Silicon Solar Cell Materials and Processes,* Winter Park CO (NREL, Golden CO, 2004), p. 230.

[28] A. A. Istratov, W. Huber and E. R. Weber, *submitted to Appl. Phys. Lett.* (2004).

[29] D. Franke, T. Rettelbach, C. Häßler, W. Koch and A. Müller, *Solar Energy Materials and Solar Cells* **72**, 83 (2002).

[30] B. L. Sopori, L. Jastrzebski and T. Tan, in *Proceedings of the 25th IEEE Photovoltaic Specialists Conference,* Washington, DC (IEEE, New York, 1996), p. 625.

[31] D. Macdonald, A. Cuevas and F. Ferrazza, *Solid-State Electronics* **43**, 575 (1999).

[32] D. A. Ramappa and W. B. Henley, *Journal of the Electrochemical Society* **144**, 4353 (1997).

[33] W. B. Henley and D. A. Ramappa, *Journal of Applied Physics* **82**, 589 (1997).

Figure 1. Reduction in the 'apparent' Fe_i concentration due to re-pairing after illumination. The straight line shows the exponential fit used to estimate $[Fe_i]$ immediately after illumination. Illumination times of 20 and 40 seconds are shown.

Figure 2. Concentrations of B, Fe, Co and Cu as a function of ingot position (fraction from top, hence 0 is the top, 1 the bottom). The straight lines are segregation model fits, with k_{eff} =0.65 for B, and k_{eff} <0.05 for Fe.

Figure 3. Concentrations of Au, Ag, Cr and Zn as a function of ingot position (fraction from top).

Figure 4. Ratio of measured to modeled impurity concentrations for Fe, Co and Cu, as a function of $D^{0.5}$ at 950°C, the normalized, approximate diffusion length for these impurities at the top of the ingot during cooling.

Figure 5. Concentrations total Fe and interstitial Fe as a function of ingot position (fraction from top). The straight lines are segregation model fits, with k_{eff}<0.05.

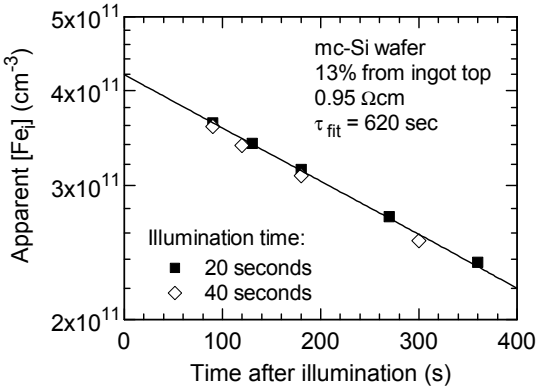

Figure 1 Macdonald *et al.* J. Appl. Phys.

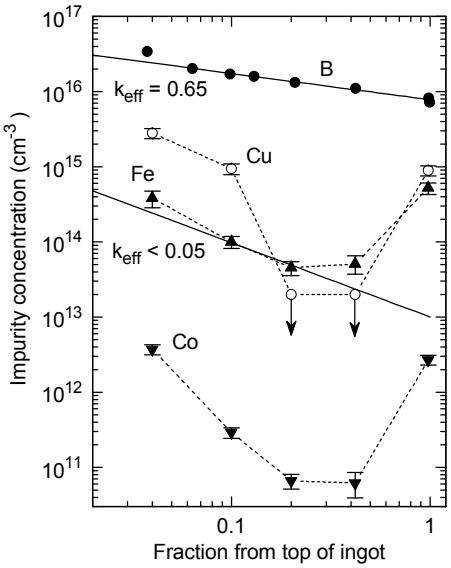

Figure 2 Macdonald *et al.* J. Appl. Phys.

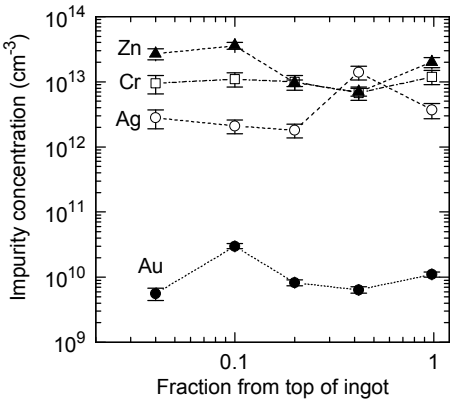

Figure 3 Macdonald *et al.* J. Appl. Phys.

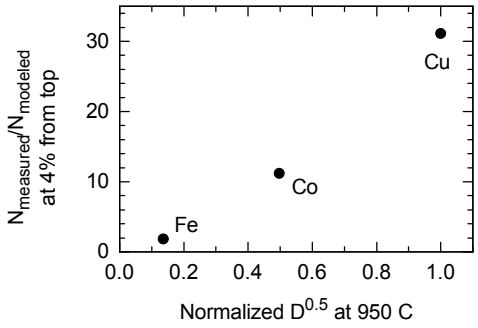

Figure 4 Macdonald *et al.* J. Appl. Phys.

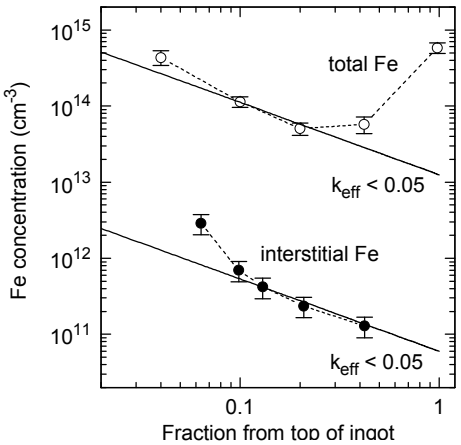

Fig. 5. Macdonald *et al.* J. Appl. Phys.

2. DYNAMICS OF LIGHT-INDUCED FEB PAIR DISSOCIATION IN CRYSTALLINE SILICON

L. J. Geerligs

Energy research Centre of the Netherlands ECN, Solar Energy, PO Box 1, NL-1755 ZG Petten,
The Netherlands

Daniel Macdonald

Department of Engineering, FEIT, Australian National University,Canberra, ACT 0200, Australia

Abstract

The dynamics of light-induced dissociation of iron-boron (FeB) pairs in p-type crystalline silicon is investigated. The dissociation is observed to be a single-exponential process which is balanced with thermal repairing. The dissociation rate is proportional to the square of the carrier generation rate and the inverse square of the FeB concentration. This suggests that the dissociation process involves two recombination or electron capture events. A proportionality constant of $5x10^{-15}$ s describes the dissociation rate well in the absence of other significant recombination channels. The dissociation rate decreases in the presence of other recombination channels. These results can be used for reliable detection of iron in silicon devices and materials, and for further elucidation of the electronically driven FeB dissociation reaction.

Published in Applied Physics Letters **85**, 5227-5229 (2004).

Iron is an important contaminant in silicon-based integrated circuit and solar cell technology. The presence of interstitial iron (Fe_i) in silicon can dramatically reduce the non-equilibrium carrier lifetime, even at very low concentrations. Therefore the most sensitive technique available for detecting iron contamination is based on lifetime or diffusion length measurements.[1] It utilizes the fact that the iron content of a boron-doped p-type Si wafer can be deliberately cycled between being mostly present as Fe_i or as pairs with substitutional boron: $(Fe_i)^+(B_s)^-$ pairs. At room temperature in thermal equilibrium virtually all Fe_i is present as FeB pairs. FeB pair dissociation can be accomplished by illumination at room temperature,[2] by minority carrier injection,[3] or by increasing temperature which shifts the equilibrium state of Fe_i and B to isolated ions.**Error! Bookmark not defined.** The isolated and paired form of interstitial iron have markedly different recombination properties.[4,5] This leads to significant changes in carrier lifetime and diffusion length after dissociating the FeB pairs. Assuming that all other recombination processes remain unchanged, the FeB concentration can be found by measuring the carrier lifetime before (τ_0) and after (τ_1) pair dissociation: $[FeB]=C(\tau_1^{-1}-\tau_0^{-1})$. The use of the known recombination parameters of both FeB pairs and Fe_i provides the pre-factor C.[6] This technique for detection of iron has become widely used in commercial applications for contamination control in microelectronics, as well as being an extremely useful tool for researching iron in silicon and gettering processes in silicon photovoltaics.

The repairing kinetics of FeB was investigated previously by Zoth and Bergholz[1] and was reported to follow an exponential behavior with repairing rate $\Gamma_r = (N_A T/4.3\cdot 10^5)\exp(0.68\text{eV}/k_B T)$ with the boron dopant density N_A in cm^{-3} and T in K. However, the kinetics of the light-induced dissociation of FeB has not been reported in any detail previously, even though illumination is most often used in practice. It is believed that the process is recombination-enhanced or recombination-induced. In this paper we present experimental results and modeling which describe quantitatively the light-induced dissociation, and provide insight into the dissociation mechanism and the dependence on sample characteristics. We compare the results to earlier carrier-injection driven FeB pair dissocation reported by Kimerling and Benton.[3] As these authors noted, apart from the technological relevance, the dissociation is in itself an interesting object for study of electronically driven defect reactions.

Details of the investigated samples are given in Table 1. Most of the experiments were performed on monocrystalline float-zone (FZ) silicon. Some multicrystalline (mc-Si) samples were also investigated because of the dominance of this material in solar cell technology. The FZ samples were contaminated with Fe by implantation or in-diffusion.[4] Mc-Si already contains a significant amount of interstitial Fe from the growth process and therefore the mc-Si samples did not receive any additional iron. The samples received a surface-passivating SiN_x coating (surface recombination velocity less than 100 cm/s) and carrier lifetime was measured by quasi-steady state photoconductance (QSSPC)[7]. The total FeB concentration was determined by lifetime change after intense illumination, sufficient to dissociate all FeB pairs. In two samples the surface recombination rate was deliberately increased, for sample FZ8* by corona charging the SiN_x coating, and for sample MC1c* by omitting the SiN_x coating altogether.

The FeB dissociation was accomplished by illumination with halogen lights, at or slightly below room temperature. Intervals of illumination were alternated with measurements of the momentary FeB

concentration. The repairing during each measurement can be calculated and is only significant (4-10%) in a few samples with high [FeB] and high N_A, in which case the measurements were corrected for this effect. The minority carrier generation rate G due to the illumination was calculated from the illumination level in suns,[8] as measured with a high-efficiency silicon solar cell. 1 sun was estimated to result in $G=2.1\cdot10^{17}$ cm^{-2}s$^{-1}/t$, where t is the sample thickness. In samples FZ1b and MC1c* the carrier diffusion length was so low that the excess carrier density was inhomogeneous over the thickness of the sample, therefore t was replaced by an effective thickness.[9]

Figure 1 shows FeB dissociation data of sample FZ8 for two illumination intensities, as an example of typical curves. The results are expressed in $n(t)\equiv N_{FeB}(t)/N_{FeB}(0)$, i.e., the concentration of FeB pairs after illumination for a cumulative duration t, relative to the total concentration at $t=0$. It can be observed that the FeB concentration initially follows a single-exponential curve, but for large t flattens off to an asymptotic value larger than zero.

This behavior can be described by a single-exponential light-induced FeB dissociation process with rate Γ_d, balanced with the thermal repairing process with rate Γ_r. If dissociation and repairing rates do not depend on the relative concentrations of Fe_i and FeB, then $dn/dt=-n(t)[\Gamma_r+\Gamma_d]+\Gamma_r$, and

$$n(t)\equiv\frac{N_{FeB}(t)}{N_{FeB}(0)}=\left[\frac{\Gamma_d}{\Gamma_r+\Gamma_d}\right]e^{-(\Gamma_r+\Gamma_d)t}+\frac{\Gamma_r}{\Gamma_r+\Gamma_d}$$

(1)

This equation was used to fit the data in Figure 1. It is clear that within measurement accuracy the model describes the data well. For accurate determination of the FeB dissociation rate Γ_d for all samples, we have used the fact that the initial decay rate of $\ln[n(t)]$ equals Γ_d, i.e., $\frac{d}{dt}\ln[n(t)]_{t=0}=\Gamma_d$. Deriving Γ_d from a fit to the complete $n(t)$ curve is complicated by the fact that for low illumination levels recombination through Fe_i is more effective than through FeB. Thus, as FeB is being dissociated and replaced by the more recombination-active Fe_i, the *recombination per FeB center* is reduced. It can therefore be expected that Γ_d decreases as *n(t)* is reduced. In agreement with this, we generally found the asymptotic value $n(\infty)=\Gamma_r/(\Gamma_r+\Gamma_d)$ to be larger than the value calculated from the $t=0$ value of Γ_d and the independently determined value of Γ_r.

For several samples, Γ_d was determined as a function of minority carrier generation rate G. Those measurements followed a power-law dependence $\Gamma_d \propto G^m$. Table 1 lists the fitted value of m for each sample, which varies around m=2. Under steady-state conditions, the generation G is balanced by recombination. Recombination in the FZ wafers is dominated by FeB and Fe_i (at $t=0$, by FeB only). The scaling of Γ_d with G^m, with m≈2, therefore indicates that 2 recombination or electron capture events through an FeB center are responsible for the dissociation.

If the FeB dissociation rate depends on the square of the recombination rate through the FeB centers, it may then also be expected that for constant G samples with different FeB concentration show a scaling $\Gamma_d \propto [FeB]^{-2}$. To verify this, in Figure 2 all measured dissociation rates are plotted as Γ_d

$\times[FeB]^2$ versus carrier generation rate. The FZ sample data in Figure 2, with the exception of samples FZ1a and FZ20, are indeed quite well arranged on a single line: $\Gamma_d = K \times G^2/[FeB]^2$, with $K \approx 5\text{x}10^{-15}$ s. This means that the square of the recombination rate per FeB center determines Γ_d. The cause for the deviation of FZ20 is unclear. The deviation of FZ1a and of the mc-Si samples is attributed to the existence in these samples of significant other recombination channels.

Note that the carrier lifetime is strongly injection-level dependent, and therefore the excess carrier density does not scale linearly with G. Scaling of Γ_d with G is therefore different from scaling with excess carrier density.

If there are other recombination channels (defects, other impurities, surface recombination), the recombination per FeB center is reduced and therefore a lower dissociation rate is expected. We describe the recombination through such other recombination channels by a rate τ_{other}^{-1}, and the recombination through FeB by the rate τ_{FeB}^{-1}. Table 1 shows for each sample the ratio τ_{other}/τ_{FeB} at an excess carrier density of 10^{15} cm^{-3}. Indeed, when the surface recombination of sample FZ8 was increased by corona-charging of the SiNx, a reduction of the ratio τ_{other}/τ_{FeB} from 3.4 in FZ8 to 1.5 in FZ8* resulted in a reduction of $\Gamma_d \times [FeB]^2/G^2$ from $8\text{x}10^{-15}$ to $5\text{x}10^{-15}$ s. Similarly, for samples MC1c and MC1c*, the absence of a surface-passivating coating decreases τ_{other}/τ_{FeB} from 10 to 0.14 and drastically reduces $\Gamma_d \times [FeB]^2/G^2$ from $6\text{x}10^{-16}$ to $1.8\text{x}10^{-18}$ s. For sample FZ1a, $\tau_{other}/\tau_{FeB}=1$ is also relatively low, which may be the reason for the low value of $\Gamma_d \times [FeB]^2/G^2$ for this sample. With the present data a quantitative analysis of the reduction of Γ_d due to other recombination channels is however impossible, because τ_{other} is determined from QSSPC data at an injection level of 10^{15} cm^{-3}, whereas a precise characterization at the injection levels actually reached during illumination (which are generally much lower) would be necessary. This is difficult to accomplish with the QSSPC method.

The results for the mc-Si samples in Figure 2 agree well with the FZ samples. It should however be noted that in mc-Si samples inhomogeneities affect the results. The QSSPC technique measures the geometrically averaged lifetime. Since low-lifetime areas contribute little to the QSSPC signal, in mc-Si the FeB concentration may be overestimated (we estimate typically by a factor of ~2)[6,10], and the effect of other recombination channels may be underestimated.

Finally, we compare our experiments to earlier reports of carrier-injection induced FeB pair dissociation, and consider the implications for the dissociation mechanism. Kimerling and Benton studied the kinetics of FeB dissociation by carrier injection in n^+p-junctions.**Error! Bookmark not defined.** They concluded that a charge-capture driven process was occurring, where neutralisation of the $(Fe_i)^+$ removes the Coulomb attraction between Fe_i and B_s. They noted that by itself this neutralization is not sufficient to result in a significant dissociation rate at room temperature, and also can not result in the observed temperature dependence with a very low activation energy of 0.1 eV. Therefore, an additional 'energy deposition process' was involved in their model. The observation of a quadratic dependence on generation level in our experiments is consistent with this interpretation. The quadratic dependence implies that two electron capture events are involved in FeB dissociation. A possible mechanism may be, for example, that the Fe_i is negatively charged by two capture events, resulting in Coulomb repulsion of the Fe_iB_s pair. An alternative mechanism may be that one

recombination event is the 'energy deposition process' and a second electron capture results in neutralization of the Fe_i, together resulting in pair dissociation.

Kimerling and Benton observed a linear dependence of the dissociation rate on the injected current density, between 0.1 and 1.5 A/cm^2. This seems to contradict our experimental results. This discrepancy is presently not understood. However, the local injection levels used by Kimerling and Benton were very high and therefore Auger recombination may have masked the quadratic dependence (Auger recombination provides an 'other recombination channel' as previously discussed, and increases with injection level). In any case, the results presented here are more directly applicable to light-induced dissociation, which is more widely used than dissociation by current injection.

In conclusion, we have presented results showing that the FeB dissociation rate scales with the square of the carrier generation rate, and the inverse square of the FeB concentration. The proportionality constant of $5x10^{-15}$s describes the dissociation rate well in the absence of other recombination channels. These results show that the square of the recombination rate per FeB center is the determining factor for the dissociation rate, which may help to elucidate the precise dissociation mechanism.

Acknowledgments

This work has been supported by NOVEM (The Netherlands Agency for Energy and the Environment) and the Australian Research Council. We would like to thank A.R. Burgers for helpful advice on the modeling and Kate McClean for performing some of the measurements. LJG thanks Australia and the Australian National University for their hospitality during a visit in which most of the work was performed.

References

[1] G. Zoth and W. Bergholz, J. Appl. Phys. 67, 6764 (1990)

[2] K. Graff and H. Pieper, J. Electrochem. Soc. 128, 669 (1981).

[3] L.C. Kimerling and J.L. Benton, Physica 116B, 297 (1983); L.C. Kimerling, Proc. of the MRS Annual Meeting, 1980, Boston, MA (North-Holland), p. 85.

[4] D. Macdonald, A. Cuevas, J. Wong-Leung, J. Appl. Phys. 89, 7932 (2001).

[5] A.A. Istratov, H. Hieslmair, and E.R. Weber, Appl. Phys. A: Mater.Sci.Process. 69, 13 (1999).

[6] D.H. Macdonald, L.J. Geerligs, and A. Azzizi, J. Appl. Phys. 95, 1021 (2004).

[7] R.A. Sinton and A. Cuevas, Appl. Phys. Lett. 69, 2510 (1996); www.sintonconsulting.com

[8] sun is the unit of illumination intensity concentration. 1 sun results in the same solar cell current as the standardized (1000 W/m^2, AM1.5) terrestrial solar spectrum. See Handbook of Photovoltaic Science and Engineering, Eds. A. Luque and S. Hegedus, Wiley, 2003.

[9] The cross-over of the lifetime curves of Fe_i and FeB, which occurs at a well-defined excess carrier density, provides this effective thickness. See ref.

[10] L.J. Geerligs, D. Macdonald, Practical aspects of FeB measurements in crystalline silicon, to be published.

Table 1. Samples investigated in this paper. FZ designates a monocrystalline float-zone silicon sample, MC a multicrystalline silicon sample. All samples apart from MC1c* are surface-passivated with SiN_x. MC1c and MC1c* are sister wafers. τ_{other}/τ_{FeB} is a measure of the importance of recombination through FeB versus recombination through other channels. m_{fit} is the fitted exponent of the dependence of FeB dissociation rate on minority carrier generation rate: $\Gamma_d \propto G^m$.

sample	ρ (Ωcm)	N_A (cm^{-3})	[FeB] (cm^{-3})	τ_{other}/τ_{FeB}	m_{fit}
FZ1a	1	$1.5x10^{16}$	$1.5x10^{11}$	1.2	1.8
FZ1b	1.1	$1.4x10^{16}$	$1.1x10^{13}$	13	
FZ4	4	$3.5x10^{15}$	$5.4x10^{12}$	>>10	1.7
FZ8	8	$1.7x10^{15}$	$6.3x10^{11}$	3.4	1.5-2.2
FZ8* corona-charged	8	$1.7x10^{15}$	$6.3x10^{11}$	1.5	
FZ20	20	$6.8x10^{14}$	$8x10^{11}$	>10	2.8
MC1a	1.1	$1.3x10^{16}$	$2.3x10^{11}$	0.8	
MC1b	0.9	$1.7x10^{16}$	$6.9x10^{11}$	1.7	
MC1c	1.2	$1.3x10^{16}$	$2.5x10^{12}$	10	1.6
MC1c* unpassivated surface	1.2	$1.3x10^{16}$	$2.5x10^{12}$	0.14	

Figure captions.

Figure 1. Normalized FeB concentration as a function of illumination time for sample FZ8, for two different illumination levels: i) 0.068 sun corresponding to $G=6\cdot10^{17}$ $cm^{-3}s^{-1}$; and ii) 0.134 sun corresponding to $G=1.2\cdot10^{18}$ $cm^{-3}s^{-1}$. Inset: logarithmic plot. The dashed and dotted lines are fits to equation 1, with $\Gamma_d(0.068sun)=0.0075$ s^{-1}; $\Gamma_d(0.134sun)=0.03$ s^{-1}; and $\Gamma_r= 4.5\cdot10^{-4}$ s^{-1}.

Figure 2. FeB pair dissociation rates plotted as $\Gamma_d x[FeB]^2$ as a function of light-induced carrier generation G. The dashed lines are guides to the eye connecting data points. The solid line shows the quadratic dependence $\Gamma_d=(5\cdot10^{-15}\ s)\times G^2/[FeB]^2$.

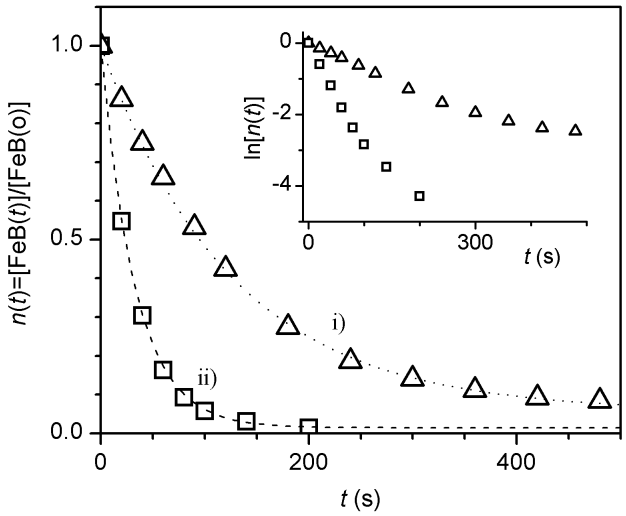

Figure 1
L.J. Geerligs and Daniel Macdonald

Applied Physics Letters

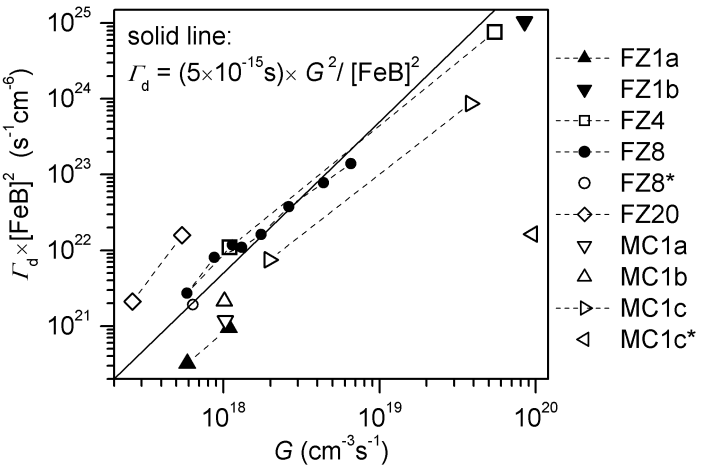

Figure 2
L.J. Geerligs and Daniel Macdonald

Applied Physics Letters

3. IRON DETECTION IN CRYSTALLINE SILICON BY CARRIER LIFETIME MEASUREMENTS FOR ARBITRARY INJECTION AND DOPING

D. H. Macdonald, L. J. Geerligs and A. Azzizi

ECN Solar Energy, PO Box 1, NL-1755 ZG Petten, The Netherlands

An existing technique for accurate measurement of iron in silicon, which was previously restricted to low-injection and a narrow doping range, has been extended to arbitrary injection and doping levels. This allows contact-less lifetime measurement techniques to be used for very sensitive and rapid iron detection under a wide range of conditions. In addition, an easily measured and unambiguous 'fingerprint' of iron in silicon has been identified. It is based on the invariant nature of the excess carrier density at which the injection-dependent lifetime curves, measured before and after iron-boron pair dissociation, cross over. This characteristic crossover point lies in the narrow range of $1.4\text{-}2.0\times10^{14}\text{cm}^{-3}$, provided only that the boron concentration is below $5\times10^{16}\text{cm}^{-3}$. To demonstrate the value of these techniques, they have been applied to photovoltaic-grade cast multicrystalline silicon wafers.

Published in Journal of Applied Physics **95**, 1021-1028 (2004).

I. INTRODUCTION

The presence of interstitial iron (Fe_i) in silicon can dramatically reduce the non-equilibrium carrier lifetime, even at very low concentrations. It is therefore not surprising that the most sensitive technique available for detecting iron contamination is based on lifetime or diffusion length measurements. This widely used technique was developed by Zoth and Bergholz[1], and utilizes the fact that the iron content of a boron-doped p-type Si wafer can be deliberately cycled between being mostly present as either Fe_i, or as FeB pairs. Courtesy of their different energy levels and capture cross-sections, these two forms of iron have markedly different recombination properties. This leads to significant changes in diffusion length after dissociating the FeB pairs, either by thermal annealing or optical activation.

Zoth and Bergholz showed that, by measuring the low-injection diffusion length before (L_0) and after (L_1) pair dissociation, and assuming that all other recombination processes remain unchanged, the total iron concentration (cm^{-3}) can be found by:

$$[Fe] = A \times \left(\frac{1}{L_1^2} - \frac{1}{L_0^2} \right) = C \times \left(\frac{1}{\tau_1} - \frac{1}{\tau_0} \right) \qquad (1)$$

The pre-factor A was determined empirically to be 1.06×10^{16} $\mu m^2 cm^{-3}$ for silicon wafers of dopant density $1\text{-}3 \times 10^{15} cm^{-3}$ (resistivity range 5-15Ωcm). If the low-injection carrier lifetime τ is measured rather than the diffusion length, then the pre-factor C is related to A via $A = D_n C$, where D_n is the minority carrier diffusion coefficient.

Equation 1 has become widely used in commercial applications for contamination control in microelectronics, as well as being an extremely useful tool for researching iron in silicon[2-4]. It is most sensitive when iron is the dominant recombination center, but is also valid when other centers are present too, provided they are not affected by the dissociation procedure.

However, there are some restrictions on the use of this specific technique. Firstly, the diffusion lengths must be measured under low-injection conditions. The most reliable technique for this is the Surface PhotoVoltage method (SPV), since it operates in true low-injection. However, other lifetime measurement techniques, such as microwave-detected photoconductance decay or the Quasi-Steady-State PhotoConductance (QSSPC)[5] technique, suffer from reduced sensitivity at low-injection. Equally importantly, they are also affected by minority carrier trapping artifacts at low-injection[6]. Such trapping causes a large excess of majority carriers, which distorts the photoconductance, since it comprises both minority and majority carriers. Voltage-based techniques such as SPV are not affected by trapping because they detect only minority carriers. As a result of these considerations, the photoconductance-based lifetime techniques, which are widely-used and otherwise more convenient than SPV, generally operate at mid- to high-injection. In this regime the value of C will be different (often very significantly) to that determined for SPV measurements.

Secondly, even for low-injection SPV measurements, if the dopant density is well outside the range 1-3×10^{15}cm^{-3}, it is not entirely valid to use the pre-factor found by Zoth and Bergholz. This is due to the particular properties of Fe_i and FeB: the energy level of the FeB center is relatively shallow, and its impact on the low-injection lifetime therefore depends on the dopant density. On the other hand, Fe_i, being a deep center, produces a low-injection lifetime that is *independent* of the doping

$$\tau_{SRH} = \frac{\tau_{p0}(n_1 + \Delta n) + \tau_{n0}(N_A + p_1 + \Delta n)}{N_A + \Delta n}. \qquad (2)$$

level[7]. Since the pre-factor C is determined by the *difference* of the inverse lifetimes, it must also vary with the dopant density.

In this paper we make use of the known recombination parameters of both FeB pairs and Fe_i to determine the pre-factor C for arbitrary dopant density and injection level. This allows the current Fe detection method to be greatly extended. As an example, the Fe concentration in solar grade multicrystalline silicon (1Ωcm) is measured before and after gettering, using the QSSPC technique operating at excess carrier densities in the range 10^{14}-10^{16}cm^{-3}. Despite the quite strong injection dependence of the measured lifetimes in this range, the calculated Fe concentration is shown to be independent of the injection level, as indeed it should be.

An important aspect of using this technique is that the proportion of Fe present as FeB pairs must be known reasonably accurately during the measurements before and after dissociation. By comparing optical and thermal dissociation, we demonstrate that strong optical illumination (>0.1Wcm^{-2}) results in almost complete (>99%) dissociation of the FeB pairs. Allowing a sample to relax in the dark for at least 24 hours results in almost complete repairing for typical dopant densities.

In addition, a distinctive fingerprint of Fe contamination in silicon is presented. It is based on measuring the injection level at which the lifetime curves before and after FeB pair dissociation cross over. The fact that such a 'crossover' exists has been observed previously[8-10]. However, in this paper we show this crossover point is *independent* of the dopant density. Measuring the excess carrier density at which the crossover occurs allows fast and unambiguous identification of iron in silicon.

II. DETERMINING THE FACTOR *c* for arbitrary injection and doping

When the density of a given type of recombination center is small, it is possible to use Shockley-Read-Hall (SRH) statistics[11,12] to model their impact on the excess carrier lifetime. Due to its relatively low solubility at typical processing temperatures, this is almost always true for iron in silicon. For p-type silicon with an acceptor concentration N_A, the Shockley-Read-Hall lifetime τ_{SRH} is given by[13]:

The parameters τ_{n0} and τ_{p0} are related to the electron and hole capture cross sections σ_n and σ_p of the recombination center, their density N, and the carrier thermal velocities v_{th}:

$$\tau_{n0} = \frac{1}{N\sigma_n v_{th}} \qquad \tau_{p0} = \frac{1}{N\sigma_p v_{th}}. \tag{3}$$

The factors n_1 and p_1 are the equilibrium carrier densities when the recombination center energy E_T coincides with the Fermi level. The thermal velocity[14] is taken as 1.1×10^7cms^{-1}.

When there are two types of recombination center present, such as for boron-doped p-type silicon containing both FeB and Fe_i, their combined impact, together with the impact of other recombination processes, results in an effective lifetime:

$$\frac{1}{\tau_{eff}} = \frac{1}{\tau_{FeB}} + \frac{1}{\tau_{Fe_i}} + \frac{1}{\tau_{other}}. \tag{4}$$

The robustness of the technique pioneered by Zoth and Bergholz is largely due to the use of the *difference* of the inverse effective lifetime before and after dissociating the FeB pairs. Hence the term involving other processes cancels out, provided these processes are not altered by the dissociation step. Also, since Zoth and Bergholz used SPV for diffusion length measurements, they were naturally restricted to the low-injection regime, where the lifetimes are independent of the excess carrier density.

However, in general, the value of the constant C in Eq 1 does depend on both the dopant density and the excess carrier density. It will also depend on the precise proportion of Fe present as FeB pairs and Fe_i before and after the dissociation process. In the simplest case, we may assume that 100% of the Fe is paired before dissociation and 100% interstitial afterwards, an assumption which is shown in later sections to be reasonable when strong optical dissociation is used. By using known values of the energy levels and capture cross sections[7,15], shown in Table I, C can be calculated directly for any dopant density or excess carrier density by substituting Eq 2 for both Fe_i and FeB into Eq 1. In other cases where either association or dissociation is incomplete, the value of C can be calculated with the aid of Eq 4.

As an example, Fig 1 shows calculated values of $1/C$ as a function of Δn for a range of dopant densities. In these plots, complete pairing and dissociation are assumed. At very low injection conditions, the value of C is always positive (meaning lifetimes decrease after dissociation) and independent of the excess carrier concentration. This is the region in which Zoth and Bergholz's SPV technique is valid. Fig 1 shows that even when low-injection conditions prevail, the value of C does indeed vary with the dopant density. This variation becomes even greater when considering the corresponding diffusion length constant A, due to the doping dependence of D_n.

At injection levels greater than approximately $\Delta n=2\times10^{14}$cm^{-3}, the value of C becomes negative for all dopant densities, meaning that the lifetime *increases* after dissociation. It is this region,

as magnified in Fig 2, which is of relevance for determining Fe concentrations by lifetime techniques that operate under medium to high injection.

In order to minimize the uncertainties when using this approach for Fe detection, it is desirable to measure the change in lifetime at a fixed value of Dn near which C does not change too rapidly. For commonly used dopant densities this corresponds to the region Dn=10^{15}-10^{16}cm^{-3}. Above this range, the presence of Auger or emitter recombination may cap the *magnitude* of the effective lifetime, therefore reducing sensitivity.

The detection limit of the technique will depend on the value of C, and this of course varies with injection level. The low-injection SPV technique has been shown capable of detecting Fe concentrations as low as 7×10^{7}cm^{-3} in 1-10Ωcm material[2], in which case the diffusion length changed very slightly from 1126 to 1119μm after dissociation. These measurements required a 3mm thick Si slab to avoid excessive rear surface recombination, and averaging of several measurements to reduce noise. If using other lifetime techniques at an injection level of 1×10^{15}cm^{-3}, and assuming excellent surface passivation capping the effective lifetime to 5000μs, the corresponding change in lifetime would be from around 4990 to 4950μs for 7×10^{7}cm^{-3} of Fe. This means a relative uncertainty of less than 1% in the lifetime measurements would be required, which would only be possible with extremely stable surface passivation and averaging. However, using mid- to high-injection measurements, Fe detection well below 10^{10}cm^{-3} is certainly feasible.

A. Low-injection values of *A*

A verification of the calculated values can be obtained by comparison with the empirical value of A=1.06×10^{16} μm^{2}cm^{-3} obtained for 5-15Ωcm material by Zoth and Bergholz. They used thermal dissociation, and estimated that almost 100% of the iron was paired before thermal treatment, and 70% dissociated after heating and then quenching on an Al plate.

Fig 3 shows the values of A calculated from the SRH model for a range of dopant densities. Two cases are shown: the first assuming 70% dissociation as suggested by Zoth and Bergholz, and the second with 100% dissociation (relevant for strong optical dissociation). The electron diffusion coefficient D_n was determined from PC1D version 5.5[16]. The equilibrium proportion present as FeB pairs before dissociation was determined for each resistivity according to the empirical relation[17]:

$$\frac{[FeB]}{[Fe_i]} = 10^{-23} N_A \exp\left(\frac{0.65}{kT}\right) \qquad (5)$$

For a dopant density of N_A=1.0×10^{16}cm^{-3}, as is typical for photovoltaic silicon, this results in 99.99% as FeB pairs at 300K. Even when the dopant density is as low as 1×10^{14}cm^{-3}, this value only decreases to 99%.

Fig 3 shows that there is good agreement with Zoth and Bergholz's single data point, giving confidence in the methodology used here. This approach allows the correct pre-factor *A* to be determined for SPV measurements over a large range of resistivity.

For optical dissociation, the 100:100 curve should be quite accurate, as shown in Section IV, assuming the post-dissociation measurement is performed quickly enough to avoid re-pairing. However, the situation is more complex for thermal dissociation, since at the elevated temperatures that occur during quenching, the time constant for re-pairing may be very short, especially for more highly doped samples (see Section IV). Therefore, the 70% assumed by Zoth and Bergholz would most likely not hold for significantly different doping levels when using the same quenching conditions. For photovoltaic-grade silicon, which is usually around 1Ωcm in resistivity, it is preferable to use optical dissociation to avoid these uncertainties.

III. THE FIXED 'CROSSOVER' POINT

It should always be kept in mind that there are numerous possible explanations for an observed change in carrier lifetime after exposure to illumination. For example, the surface recombination velocity of certain types of Plasma-Enhanced Chemical Vapor Deposited (PECVD) silicon nitride films is thought to be altered by the capture of light-induced carriers at so-called K-centers[18]. Another well-known example is the carrier-induced degradation associated with metastable boron-oxygen complexes in Czochralski silicon[19], which causes a reduction in lifetime across all injection levels. The breaking of Cu-Cu pairs by illumination is also believed to reduce the lifetime[20]. It is therefore important to have an independent means of checking if any observed changes are actually due to the presence of iron.
One such method, suggested by Zoth and Bergholz, is to measure the characteristic re-pairing time as the lifetime relaxes to equilibrium conditions at room temperature. This approach, as discussed in section IV, indeed provides convincing evidence for the presence of Fe, but has the disadvantage of being somewhat time consuming.

Courtesy of the extreme asymmetry between the electron and hole capture cross section of Fe_i, it turns out that there is another robust and convenient 'fingerprint' for Fe in silicon. For all dopant densities in Figs 1 and 2, there is a particular excess carrier density $\Delta n_{crossover}$ at which the lifetime remains *unchanged* after dissociation. Despite the dopant density changing by more than two orders of magnitude in these figures, the value of this crossover point remains *almost constant* at around 1.5×10^{14}cm^{-3}. It is also possible to show that the value of this crossover point is independent of the relative populations before and after dissociation, although of course greater dissociation will allow

more accurate determination of $\Delta n_{crossover}$. The constancy of this crossover point makes it an excellent identifier of Fe.

In order to demonstrate these useful properties, consider the conditions under which the lifetimes before and after dissociation are equal:

$$\frac{1}{\tau_{FeB}(N_1)}+\frac{1}{\tau_{Fe_i}(N_2)}=\frac{1}{\tau_{FeB}(N_3)}+\frac{1}{\tau_{Fe_i}(N_4)}. \quad (6)$$

In this expression, the symbols N_1 etc. represent the density of recombination centers, such that $N_1+N_2=N_3+N_4=[Fe_i]+[FeB]=[Fe]_{total}$. The impact of other recombination mechanisms, which are not altered by the dissociation process, cancel out and are not shown.

In Appendix A it is shown that Eq 6 is equivalent to stating that:

$$\tau_{FeB}(N_1)=\tau_{Fe_i}(N_1) \quad (7)$$

In other words, the crossover point will be the excess carrier density at which the lifetimes due to any density N of FeB pairs equals the lifetime due to the *same* density of Fe_i.

We may then use the SRH model (Eq 2) to solve this expression for $\Delta n_{crossover}$. Due to the extremely small hole cross section of Fe_i, this reduces to:

$$\Delta n_{crossover} \approx \frac{\tau_{p0,FeB}}{\tau_{p0,Fe_i}} n_{1,FeB} = \frac{\sigma_{p,Fe_i}}{\sigma_{p,FeB}} n_{1,FeB} = 1.4\times10^{14}\,cm^{-3} \quad (8)$$

$$N_A << \left| \frac{\tau_{p0,FeB} n_{1,FeB}}{\tau_{n0,Fe_i}-\tau_{n0,FeB}} \right| = 1.5\times10^{17}\,cm^{-3}.$$

provided that: (9)

As N_A approaches the value on the right of Eq. 9, the crossover point begins to increase. However, so long as $N_A<5\times10^{16}cm^{-3}$, then $\Delta n_{crossover}$ will remain below 2.0×10^{14}. For most practical purposes therefore the crossover point resides in the narrow range $1.4\text{-}2.0\times10^{14}$ cm^{-3}.

There do exist some published values of the crossover point in the literature[7,8,10], and these are shown in Table II. Results from Section IV on photovoltaic-grade multicrystalline silicon are also included. Together, they provide excellent support for the value calculated above from the energy levels and capture cross sections. They also confirm that it is independent of the dopant density or silicon growth technique (i.e. presence of other recombination centers).

IV. IRON IN SOLAR-GRADE MULTICRYSTALLINE SILICON: AN EXAMPLE

Boron-doped multicrystalline silicon is in common use in photovoltaics, offering a reasonable compromise between economic cost and electronic quality. It often contains significant amounts of interstitial Fe, as shown in recent studies[9], as well as other metals[21], and so provides a suitable test for the techniques developed above. Due to its detrimental impact on lifetime, and therefore solar cell efficiency, it is also of direct interest to be able to identify Fe in such material with certainty, and to determine its concentration.

A. Identification by the 'crossover' point

Fig 4 shows injection-dependent lifetime measurements on a commercially produced, cast multicrystalline silicon wafer with N_A=1.5×10^{16} cm^{-3}. Lifetimes were measured using the QSSPC technique, with the surfaces passivated by PECVD silicon nitride[22]. Measurements were taken after 24 hours in the dark and again after 5 minutes exposure to 0.1Wcm^{-2} white light from a halogen lamp (approximately equivalent to 1 sun). The crossover point at 1.3×10^{14} cm^{-3} corresponds very well with that expected from the SRH model. A second wafer from another manufacturer, with N_A=2.2×10^{16} cm^{-3} was similarly measured and found to have a crossover occurring at 2×10^{14} cm^{-3}.

The two wafers had previously received on one side a belt furnace phosphorus diffusion resulting in a sheet resistivity of around 50Ω/square. The diffused layer, which was removed before surface passivation, provided some partial gettering of Fe and other impurities. In neighboring non-gettered wafers, the presence of minority carrier trapping centers[6] obscured the lifetime measurements below approximately 2×10^{14}cm^{-3}. The use of a correction procedure for subtracting the underlying excess photoconductance caused by traps[23] allows the crossover point to be observed in such cases. However, if the trap density is much higher than 5×10^{14}cm^{-3} this procedure becomes too uncertain at the crossover point. In such cases this technique can not be used to confirm the presence of iron in silicon.

B. Identification by re-pairing kinetics

To support the assertion that the light-induced changes in the multicrystalline samples above are due to Fe, the re-pairing rate at room temperature was measured and compared with previously reported values. This approach was recently used by Ballif *et al.*[9] to identify Fe in cast multicrystalline silicon.
After the FeB concentration has been perturbed from its equilibrium value, either by optical or thermal dissociation, the resulting excess Fe_i re-associates according to a mono-exponential decay with a

characteristic time τ_{assoc}. This parameter is well known and depends on both the dopant density and temperature[1]:

$$\tau_{assoc} = \frac{4.3\times10^{5}}{N_A} T \exp\left(\frac{0.68}{kT}\right) \qquad (10)$$

If the lifetime is measured at a carrier density above the crossover point, this repairing will result in a gradual *decrease* in the lifetime. Figure 5 shows a measurement of such relaxation for a non-gettered neighboring wafer of the multicrystalline sample of Fig 4, as well as another slightly more heavily doped sample. The lifetimes were measured at $\Delta n=3\times10^{15}$cm^{-3}. Dissociation was achieved by exposing the samples to white light of 0.1Wcm^{-2} intensity for 5 minutes. The decay of the lifetime as the FeB pair concentration approaches equilibrium fits very well with a single exponential model with τ_{assoc} = 38 and 26 minutes, as calculated from Eq 10, for these two wafers with N_A=1.5×10^{16} and 2.2×10^{16} cm^{-3} respectively. Hence there is little doubt that the observed changes in lifetime are due to Fe.

We may now turn our attention to calculating the Fe concentration from the change in lifetime at a given excess carrier density. This requires a reasonable knowledge of what proportion of Fe is paired before and after dissociation, whether by optical or thermal means, so that an appropriate value of C can be determined.

C. Paired fraction before dissociation

We may use Eq 5 to determine the equilibrium fraction of FeB pairs *before* dissociation. As discussed above, for most dopant densities this is well above 99% at room temperature. However, the time required for a sample to reach equilibrium at room temperature depends inversely on the dopant density (Eq 10). With N_A=1.0×10^{16}cm^{-3}, as is representative of the wafers used in this study, this leads to a value of 57 minutes at 300K. Hence after only 5 hours, the density of FeB pairs will reach 99% of its equilibrium value (which is 99.99% of the total Fe concentration for this dopant density). In this study wafers were rested in the dark for at least 12 hours before measurement, ensuring almost complete pairing. If using more lightly doped material however, the required relaxation times at room temperature are much longer: 50 and 500 hours for N_A=1.0×10^{15} and 1.0×10^{14}cm^{-3} respectively.

It is also possible that the measurement process *itself* causes significant dissociation of FeB pairs. For SPV this is unlikely since the illumination used to generate the photovoltage is very weak. For other mid- and high-injection techniques, much more intense illumination is generally used. The QSSPC technique, as used in this work, requires flashing the sample with a xenon lamp with an exponential decay time of 1.9ms. The peak intensity can be varied using gray filters, and ranges between 0.01-25Wcm^{-2}.

To check the extent of dissociation caused by this illumination, the multicrystalline wafer containing Fe with N_A=1.5×10^{16}cm^{-3} from Fig 5 was allowed to relax fully overnight. The lifetime was measured by QSSPC with flashes of increasing intensity, and then also after steady-state illumination of

0.1Wcm^{-2} for increasing lengths of time. The measured lifetimes are shown in Fig 6 as a function of the integrated absorbed energy. The results show that if the absorbed energy is kept below 0.01Jcm^{-2}, dissociation is avoided. This corresponds to a peak intensity of around 5Wcm^{-2} for our flash, a value that was not exceeded during any measurements presented in this work. It should be noted however that if the carrier lifetime is much larger than in the samples used here, the threshold intensity would be reduced due to the higher carrier densities, and hence greater dissociation rate, at a given illumination level.

It seems then that the assumption of almost complete pairing during the initial measurement is reasonable, at least in the cases presented here. The final question then is what proportion of iron is interstitial during the second measurement, after optical dissociation.

D. Paired fraction after dissociation

One approach to answering this is to compare the effects of optical and thermal dissociation. The advantage of thermal dissociation is that the fraction of FeB pairs is easily determined from Eq 5. However, it is important to be aware of possible re-pairing during cooling. To minimize the extent of this re-pairing, we used a vertical quench in water from between two heated metal plates.

The choice of anneal temperature is important, because at higher temperatures the dissociation is more complete, but the re-pairing time is faster. The best approach is to use a relatively high temperature where the dissociation approaches saturation. Any slight cooling before the sample hits the quench solution will then have less impact on the final interstitial proportion.

To illustrate this point, according to Eq 5, annealing at 300°C results in 92% present as Fe_i in silicon with N_A=1.5×10^{16} cm^{-3}. However, for this doping and temperature, the characteristic re-pairing time is only 0.02 seconds. This is not so important however, because even if the sample cools relatively slowly to 280°C before quenching, the proportion as Fe_i is still 89%.

By contrast, at 200 and 180°C the equilibrium proportions as Fe_i are 44% and 22% respectively, meaning a much more significant loss of Fe_i is possible if the quenching is not perfect.

The results of such annealing at 300°C are shown in Fig 5 for the non-gettered mc-Si sample with N_A=1.5×10^{16} cm^{-3}. By assuming the initial Fe_i proportion to be 92% for the thermal dissociation case, the proportion of Fe_i in the case of optical dissociation (5 minutes of 0.1Wcm^{-2} white light) for the same sample is found to be, using Eq 4, within 1% of 100%.

We can now be confident that, under the optical dissociation conditions used in these experiments, almost 100% of the Fe is paired during the first measurement, and 100% interstitial afterwards. The appropriate value of C can then be found for a given dopant density and excess carrier density, and finally $[Fe]_{total}$ can be calculated.

E. Determination of Fe concentration

In practice, it should only be necessary to measure the change in lifetime at a single value of Δn. In order to check the reliability of the technique however, we have calculated C and then $[Fe]_{total}$ at each value of Δn for the partially gettered sample in Fig 4, as well as for a neighboring wafer that was not gettered. The results are shown in Fig 7.

The uncertainties in $[Fe]_{total}$ have been calculated by assuming a 10% uncertainty in each lifetime measurement. If the difference between the two lifetimes at a given injection level is small, the resulting uncertainty in $[Fe]_{total}$ is increased. Naturally, this occurs for data near the crossover point. Nevertheless, the calculated value of $[Fe]_{total}$ is, as it should be, independent of Δn within the uncertainty limits. The range of Δn is smaller for the non-gettered sample due to trapping effects obscuring the data at lower injection levels.

The concentrations of Fe for the gettered and non-gettered wafers were determined to be 3×10^{11} and $9\times10^{11}cm^{-3}$. This reduction in Fe is not as large as might be hoped for when using phosphorus gettering. It may be that the gettering step is too short to allow complete gettering from deep within the wafer. Alternatively, the slow dissolution of precipitates in the wafer bulk may act as a constant source of interstitial Fe, maintaining a certain background level despite the ongoing gettering action.

It should be emphasized that the calculated Fe concentrations above in fact represent a form of *area-averaged* values, because the QSSPC method involves measuring a few square centimeters simultaneously, which almost always contains several grains. It is therefore likely that, in reality, the lifetime varies somewhat within this area, as may the 'background' lifetime τ_{other} (in Eq 4). These variations can cause distortions in the determination of $[Fe]_{total}$, since the QSSPC technique gives extra weight to high-photoconductance regions. For example, if 50% of the grains have τ_{other}=10μs and 50% have τ_{other}=100μs, but both contain $[Fe]_{total}$ =$5\times10^{11}cm^{-3}$, the resulting iron concentration will be overestimated by approximately 40%. However, if the inter-grain variations are not large, or the area of poor grains is small, as was the case in the regions chosen in this study, these effects will be relatively unimportant.

A more precise mapping of $[Fe]_{total}$ would be possible by using a technique such as Carrier Density Imaging[24]. This steady-state technique obtains a high-resolution map of Δn values, and therefore τ_{eff}, across a sample at a fixed generation rate. If the lifetime at a given position on the wafer changes during dissociation, and the same generation rate is used for both measurements, the resulting Δn values will be different. By contrast, when using the QSSPC technique above, which sweeps across a range of generation rates, the lifetimes before and after dissociation can be measured at the same average Δn value (although of course this will vary somewhat between grains). Using a fixed generation technique would therefore require a slight modification in the calculation of C. Since the

iron concentration and lifetime may also vary laterally across a sample, such a modified *C* value should, in principle, be calculated for every point.

Other *differential* lifetime mapping techniques, such as microwave-detected photoconductance decay, may not be as well suited for this approach to Fe mapping. This is because they do not directly measure the value of D*n*, but can only infer it from the measured lifetime value by assuming the lifetime is injection independent[25]. This may especially cause problems when measuring the lifetime after dissociation, since then the injection dependence is quite pronounced.

V. CONCLUSIONS

Existing procedures for measuring Fe concentrations using low-injection SPV diffusion length measurements on 5-15Ωcm Si have been extended to include arbitrary doping, as well as mid- and high-injection lifetime measurements. This allows the use of fast, contact-less lifetime techniques for very sensitive measurement of Fe concentrations on any crystalline silicon material. This extended technique is slightly more complex than the SPV approach, since the pre-factor for determining $[Fe]_{total}$ changes with the injection level, which may of course vary across a sample due to changing levels of Fe.

In addition, a characteristic 'fingerprint' of Fe contamination has been presented. The 'crossover' point between the lifetime curves before and after dissociation always occurs in the range 1.4-2.0×10^{14}cm^{-3} for any doping density below 5×10^{16}cm^{-3}. This provides a fast and convenient diagnostic tool for Fe contamination.

APPENDIX A

The condition for the lifetime to be equal before and after dissociation is:

$$\frac{1}{\tau_{FeB}(N_1)}+\frac{1}{\tau_{Fe_i}(N_2)}=\frac{1}{\tau_{FeB}(N_3)}+\frac{1}{\tau_{Fe_i}(N_4)}. \qquad \text{(A1)}$$

The parameters N_1 etc. represent the density of recombination centers, so that $N_1+N_2=N_3+N_4=[Fe]_{total}$.

From the linear nature of the SRH model, lifetimes caused by different concentrations of the same recombination center are related by:

$$\tau_{FeB}(N_1)=\frac{N_2}{N_1}\tau_{FeB}(N_2). \qquad \text{(A2)}$$

Using this fact, we may then re-write Eq (A1), after some rearranging, as:

$$\frac{1}{\tau_{FeB}(N_1)} = \frac{1}{\tau_{Fe_i}(N_2)}\left(\frac{N_4 - N_2}{N_2}\right)\left(\frac{N_1}{N_1 - N_3}\right) \qquad \text{(A3)}$$

Making use of the fact that N_4-N_2 =N_1-N_3, and then applying an analogue of Eq (A2), this reduces to the desired result:

$$\tau_{FeB}(N_1) = \tau_{Fe_i}(N_1). \qquad \text{(A4)}$$

This result is quite general and would also apply to other impurities that undergo some type of change of state that leads to a crossover in the injection dependent lifetime curves. It should be noted, however, that some pairs of meta-stable impurities, for example CrB and Cr_i, do not exhibit such a crossover, at least for some dopant densities[8]. For such sets of energy levels and cross sections, there exists no value of Δn which satisfies Eq (A4).

ACKNOWLEDGEMENTS

This work has been supported by NOVEM (The Netherlands Agency for Energy and the Environment) under contract number 2020.01.13.11.2002. The authors are grateful to A. Cuevas, J. Bultman and A. Weber for helpful discussions, and to staff of ECN for assistance with sample preparation.

REFERENCES

1. G. Zoth and W. Bergholz, Journal of Applied Physics **67**(11), 6764 (1990).
2. J. Lagowski, P. Edelman, A. M. Kontkiewicz, O. Milic, W. Henley, M. Dexter, L. Jastrzebski and A. M. Hoff, Applied Physics Letters **63**(22), 3043 (1993).
3. L. Jastrzebski, W. Henley, D. Schielein and J. Lagowski, Journal of the Electrochemical Society **142**(11), 3869 (1995).
4. W. B. Henley and D. A. Ramappa, Journal of Applied Physics **82**(2), 589 (1997).
5. R. A. Sinton and A. Cuevas, Applied Physics Letters **69**(17), 2510 (1996).
6. D. Macdonald and A. Cuevas, Applied Physics Letters **74**(12), 1710 (1999).
7. D. Macdonald, A. Cuevas and J. Wong-Leung, Journal of Applied Physics **89**(12), 7932 (2001).
8. T. Pavelka, in *Recombination lifetime measurements in silicon*, ed. by D. C. Gupta, F. R. Bacher, and W. M. Hughes (American Society for Testing and Materials, 1998) p.206.

9. C Ballif, S. Peters, D. Borchert, C. Hassler, J. Isenberg, R. Schindler, W. Warta, and G Willeke, Proceedings of the 17th EC-PVSEC, Munich, Germany, 2001, p. 1818.

10. R. Falster and G. Barionetti, in *Recombination lifetime measurements in silicon*, ed. by D. C. Gupta, F. R. Bacher, and W. M. Hughes (American Society for Testing and Materials, 1998) p.226.

11. W. Shockley and W. T. Read, Phys.Rev. **87**(5), 835 (1952).

12. R. N. Hall, Phys.Rev. **87**, 387 (1952).

13. J. S. Blakemore, *Semiconductor Statistics*, International Series of Monographs on Semiconductors, Vol 3 (Pergamon Press, Oxford, 1962).

14. W. M. Bullis and H. R. Huff, Journal of the Electrochemical Society **143**(4), 1399 (1996).

15. A. A. Istratov, H. Hieslmair, and E. R. Weber, Applied Physics A **69**, 13 (1999).

16. P. A. Basore and D. A. Clugston, *PC1D v5.5* (University of New South Wales, Sydney, Australia, 2000).

17. L. C. Kimerling and J. L. Benton, Physica **116B**, 297 (1983).

18. A. G. Aberle, *Crystalline Silicon Solar Cells: Advanced Surface Passivation and Analysis*, (Center for Photovoltaic Engineering, University of New South Wales, Sydney, Australia, 1999).

19. J. Schmidt and A. Cuevas, Journal of Applied Physics **86**(6), 3175 (1999).

20. W. B. Henley, D. A. Ramappa and L. Jastrezbski, Applied Physics Letters **74**(2), 278 (1999).

21. S. A. McHugo, A. Thompson, I. Perichaud and S. Martinuzzi, Applied Physics Letters **72**(26), 3482 (1998).

22. M. J. Kerr and A. Cuevas, Semiconductor Science and Technology **17**, 166 (2002).

23. D. Macdonald, R. A. Sinton and A. Cuevas, Journal of Applied Physics **89**(5), 2772 (2001).

24. J. Isenberg, S. Riepe, S. W. Glunz, and W. Warta, Journal of Applied Physics **93**(7), 4268 (2003).

25. J. Schmidt, IEEE Transactions on Electron Devices **46**, 2018 (1999).

Table I. Recombination parameters of FeB and Fe_i used in the calculation of *C*. Data taken from Refs 15 and 7.

	E_T (eV)	σ_n (cm^{-2})	σ_p (cm^{-2})
Fe_i	E_V+0.38	5×10^{-14}	7×10^{-17}
FeB	E_C-0.23	3×10^{-14}	2×10^{-15}

Table II. Values of the crossover point from the literature and this work for samples of various dopant density and growth technique. The values from Ref. [10] are shown as upper limits, since they reported the *peak* excess carrier concentration, rather than the *average*.

Resist. (Ωcm)	N_A (cm^{-3})	Growth	Crossover point (cm^{-3})	Ref.
0.3	6.6×10^{16}	FZ	1.2×10^{14}	[7]
1	1.7×10^{16}	FZ	1.4×10^{14}	[7]
5	3×10^{15}	FZ	2.5×10^{14}	[7]
8-15	$1.0\text{-}1.7\times10^{15}$	Cz	$1\text{-}2\times10^{14}$	[8]
20	7×10^{14}	Cz	$<2.7\times10^{14}$	[10]
50	3×10^{14}	Cz	$<3.6\times10^{14}$	[10]
0.7	2.2×10^{16}	mc-Si	2.0×10^{14}	this work
1.1	1.5×10^{16}	mc-Si	1.3×10^{14}	this work

Figure 1. Inverse lifetime pre-factor *1/C* versus the excess carrier density Δn for various dopant densities.

Figure 2. Inverse lifetime pre-factor *1/C* versus the excess carrier density Δn for various dopant densities, for moderate Δn.

Figure 3. Comparison of the diffusion length pre-factor A from Zoth and Bergholz with those calculated from the recombination parameters of Table I. The case of 100% FeB before and 100% Fe_i after dissociation corresponds to strong optical dissociation, while the 100%:70% case corresponds to the thermal dissociation used by Zoth and Bergholz.

Figure 4. Effective lifetime versus excess carrier concentration for a partially gettered mc-Si sample containing Fe, showing the crossover of the lifetime curves at $1.3\times10^{14}cm^{-3}$ before and after optical dissociation.

Figure 5. Decrease of the effective lifetime, measured at $\Delta n=3\times10^{15}cm^{-3}$, of non-gettered mc-Si samples as the FeB pairs re-form after optical or thermal (300°C then quenched in water) dissociation. The lines show mono-exponential fits with time constants determined from Eq. 10. For the thermal dissociation case, the proportion as Fe_i immediately after quenching is 92%.

Figure 6. Effective lifetime of a non-gettered mc-Si wafer versus integrated absorbed energy from either an exponential flash or a steady-state lamp. The point at which the lifetime begins to increase marks the beginning of FeB pair dissociation.

Figure 7. Calculated Fe concentration $[Fe]_{total}$ for the non-gettered and partially gettered neighboring mc-Si samples, revealing that for each sample $[Fe]_{total}$ is independent of Δn within measurement uncertainty.

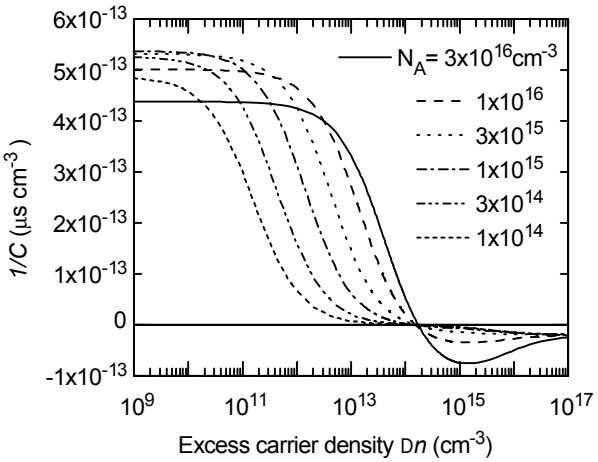

Fig. 1, Macdonald *et al*., J. Appl. Phys.

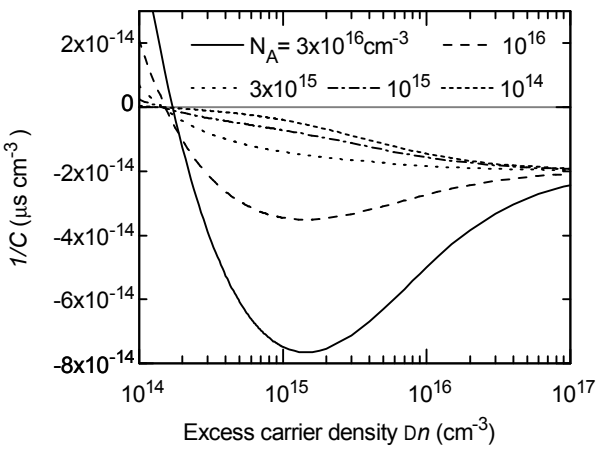

Fig. 2, Macdonald *et al*., J. Appl. Phys.

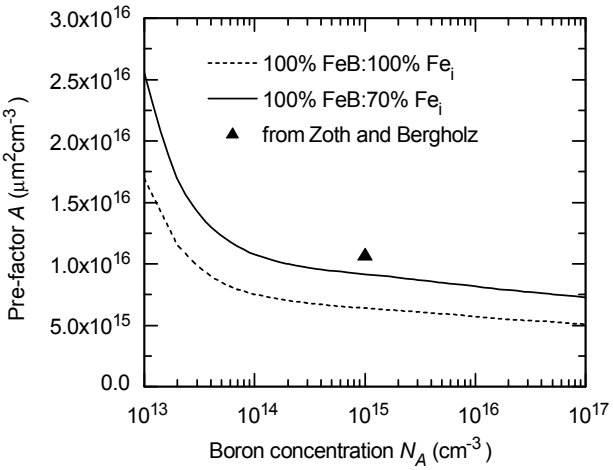

Fig. 3, Macdonald *et al*., J. Appl. Phys.

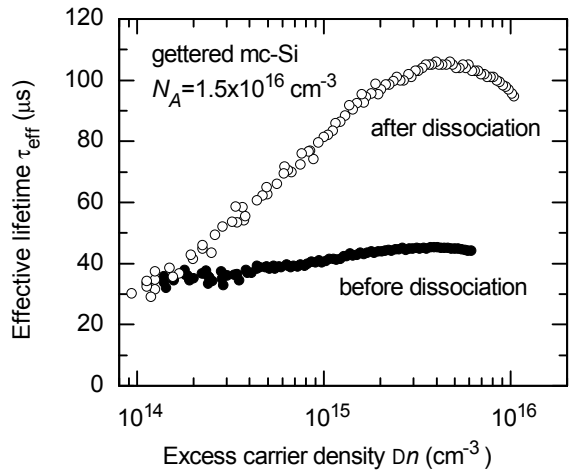

Fig. 4, Macdonald *et al*., J. Appl. Phys.

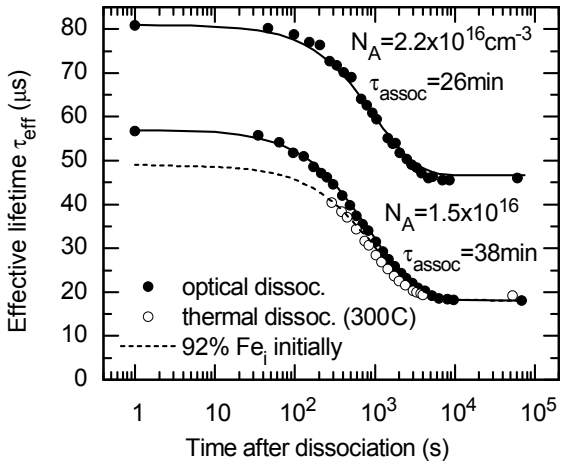

Fig. 5, Macdonald *et al*., J. Appl. Phys.

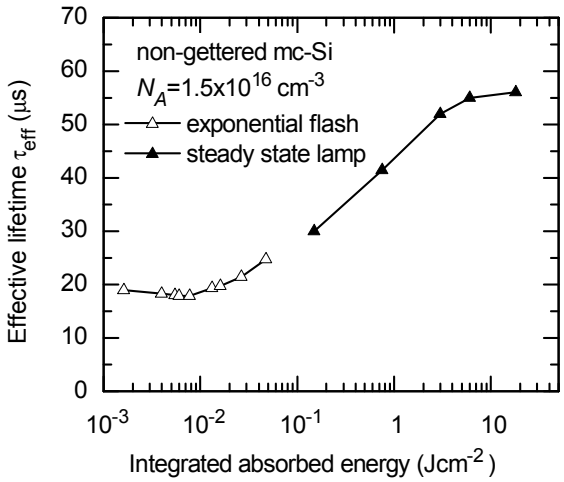

Fig. 6, Macdonald *et al*., J. Appl. Phys.

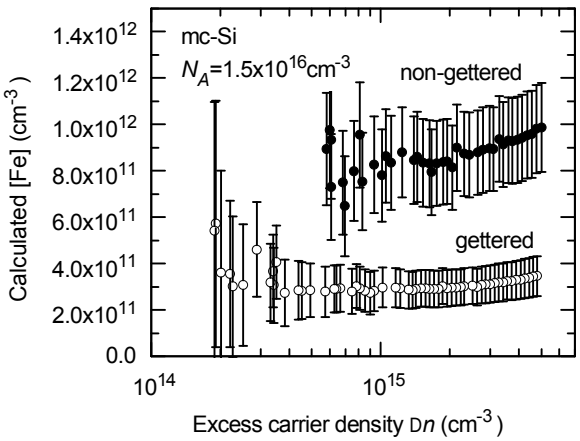

Fig. 7, Macdonald *et al*., J. Appl. Phys.

4. BASE DOPING AND RECOMBINATION ACTIVITY OF IMPURITIES IN CRYSTALLINE SILICON SOLAR CELLS.

L.J. Geerligs[1] and D. Macdonald[2]

[1]Energy research Centre of the Netherlands, ECN, P.O. Box 1, 1755 ZG Petten, The Netherlands

[2]Dept. of Engineering, FEIT, The Australian National University, Canberra ACT 0200, Australia

Abstract

The optimisation of base doping for industrial crystalline silicon solar cells is examined with model calculations. Focus is on the relation between base doping and carrier recombination through the important impurities interstitial iron (Fe_i) and the metastable boron-oxygen (BO) complex. In p-type silicon, the optimum base resistivity is strongly dependent on defect concentration. In n-type silicon, recombination due to Fe_i is much lower and nearly independent of resistivity. Fe_i is likely representative for other transition metal impurities. In many real cells a balance between Fe_i or similar defects, and BO will occur.

Keywords

silicon, base, recombination, resistivity, doping.

Contract/grant sponsors:

The Netherlands Agency for Energy and the Environment (NOVEM); contract/grant number: 2020.01.13.11.2002.

The European Commission; contract/grant number: ENK6-CT-2002-00660.

The Australian Research Council through the Discovery Program.

Published in Progress in Photovoltaics: Research and Applications **12**, 309-316 (2004).

The question of optimal base resistivity for silicon solar cell processing is of great practical interest. Decreasing base resistivity provides a way to increase V_{oc} and, accordingly, potentially the cell efficiency as well. However, it also increases Auger and radiative recombination, and reduces the effectiveness of back surface fields (BSF), and of surface passivating coatings. High-efficiency laboratory cells use a base resistivity of ~1 Ω–cm, which has been empirically found to provide a good balance between these parameters. Also for industrial multicrystalline cells, a base resistivity of 1-3 Ω-cm is commonly used. Since recombination through defects and impurities in the bulk and at the surfaces of these cells is considerably higher, the question is why the optimum in this case is not found at significantly lower resistivity. Indeed, previous modelling of industrial solar cells suggests the use of a lower base resistivity. In a recent paper, Brody *et al.* describe and model the relation between the base resistivity of silicon solar cells and cell efficiency. [1] They determine the optimal base resistivity, varying parameters such as BSF, emitter resistivity, surface passivation, and cell thickness. Their general conclusion is that the optimal resistivity is lower or even much lower than the 1-3 Ω-cm currently used. For example, for 300 micron thick cells with 20 μs bulk recombination lifetime, the optimal resistivity would be 0.24 Ω-cm in the presence of an Ohmic rear contact, and 0.6 Ω-cm for a BSF.

The paper by Brody et al. also suggests a tentative explanation for this discrepancy. It explains how it may be due to the presence of an (unspecified) dopant-defect interaction, which is modelled as essentially increasing the recombination activity of defects proportionally to the doping concentration N_A, without changing other recombination parameters such as energy level or ratio of capture cross sections. One example of such a dopant-defect interaction is the boron-oxygen-related metastable defect (BO defect, for short) which strongly limits the performance of boron-doped Czochralski (Cz) wafers. [2] The effect of the BO defect is less important in multicrystalline wafers, because these have a lower undegraded lifetime to start with (due to other defects) and the oxygen concentration is generally lower. [3,4,5]

In this paper we present another explanation for the discrepancy between modeled and empirical optimal base resistivity. This explanation is *inherent* in the relation between base resistivity and carrier recombination through impurities in the Shockley-Read-Hall (SRH) model, and is relevant for several common transition metal impurities. In the SRH model the recombination rate will either be constant or *increase* with *decreasing* base resistivity, depending on the energy level and capture cross sections of the dominant defect. An increase in recombination rate for a decrease of the resistivity of course counteracts any beneficial effects and shifts the optimum towards higher resistivity.

The dependence of SRH recombination on resistivity is very small if the defect's capture cross sections for holes and electrons are almost equal and its energy level is not shallow. It will be very prominent if the hole and electron capture cross sections differ significantly and the

smallest cross section is for the majority carrier. This is the case, for example, for interstitial iron (Fe_i), one of the most dominant impurities in p-type multicrystalline silicon. [6] Therefore we think it is probable that neglect of the relation between SRH recombination rate and base resistivity at least contributed to the discrepancy discussed above.

In this paper we will consider in detail the cases of Fe_i and, for comparison, the BO defect in industrial solar cells. Both defects drive the optimum resistivity to higher values, although via different mechanisms. It is estimated that the impact of the two defects is roughly comparable, although unfortunately the knowledge of the activity of the BO defect in multicrystalline material is limited. In addition to the effect of base resistivity, we will also shortly discuss the effect of the type (n or p) of base doping for the case of Fe_i.

The SRH recombination lifetime is, for p-type silicon, accurately represented by [7]

$$\tau_{SRH} = \frac{\tau_{p0}(n_1 + \Delta n) + \tau_{n0}(N_A + p_1 + \Delta n)}{(N_A + \Delta n)} \qquad (1)$$

N_A is the base doping concentration, which is of course directly related to resistivity: a higher N_A corresponds to a lower resistivity. Δn is the excess carrier density (assumed to be equal for electrons and holes). The parameters τ_{n0} and τ_{p0} are related to the electron and hole capture cross sections σ_n and σ_p of the recombination center, their density N, and the carrier thermal velocities v_{th} :

$$\tau_{n0} = \frac{1}{N\sigma_n v_{th,n}} \text{ and } \tau_{p0} = \frac{1}{N\sigma_p v_{th,p}}$$

The factors n_1 and p_1 are the equilibrium carrier densities when the recombination center energy E_t coincides with the Fermi level. The thermal velocity is taken as ~1.7×10^7 cms^{-1}. [8]

The approximation $\Delta n << N_A$ is appropriate for industrial solar cells with base doping N_A larger than about 10^{15} cm^{-3} and operating at maximum power, and allows the equation to be simplified further to

$$\tau_{SRH} = \frac{\tau_{p0}(n_1 + \Delta n) + \tau_{n0}(N_A + p_1)}{N_A} \qquad (2)$$

Therefore, the lifetime will depend on the base doping concentration as

$$\frac{\tau_{SRH,1}}{\tau_{SRH,2}} = \frac{N_{A,2}}{N_{A,1}} \times \frac{1+a\times(N_{A,1}+p_1)}{1+a\times(N_{A,2}+p_1)} = \frac{N_{A,2}}{N_{A,1}} \times K \qquad (3)$$

where $a = \frac{\tau_{n0}}{\tau_{p0}(n_1+\Delta n)}$

This means that if $N_{A,1} > N_{A,2}$, then $\tau_{SRH,1} < \tau_{SRH,2}$.

In some cases the factor K in eq. (3) will approach 1, and τ_{SRH} will be approximately linear in $1/N_A$, and as a result, approximately linear in resistivity. For example, Fig. 1a shows the lifetime determined by a concentration of $3\text{x}10^{11}$ cm^{-3} Fe_i, as a function of base resistivity, for typical injection levels. The Fe_i recombination parameters are E_c-E_t = 0.774 eV, σ_p=7x10^{-17} cm^2, σ_n=5x10^{-14} cm^2. [9] A concentration of Fe_i around 10^{11} cm^{-3} is common in mc-Si after gettering. [10] The region in which the lifetime increases roughly linearly with the resistivity is clearly visible. The dependence of the lifetime on the base resistivity increases dramatically for a fixed generation rate (chosen as 0.1 suns to approximate maximum power conditions in a solar cell), rather than a fixed injection level. This striking effect is related to the dependence of SRH recombination on injection level. Fig. 1a clearly shows that a significant concentration of Fe_i will result in a preference for higher base resistivity, necessary to maintain a reasonable carrier lifetime.

Fig. 1b shows a similar lifetime calculation for the BO defect. The BO defect in multicrystalline silicon has been studied in several papers. [3,4,5] Because absolute capture cross sections of this defect are not known, the relation between defect density and degradation of lifetime (from τ_i to τ_f) is expressed through a 'normalized defect density' N_t^*:

$$N_t^* \equiv \frac{1}{\tau_f} - \frac{1}{\tau_i}$$

N_t^* is proportional to the boron concentration, therefore N_t^*/N_A (in 10^{16} cm^{3}µs^{-1}) can be used to remove the dependence on the boron concentration.

The reported N_t^*/N_A varies from less than $0.01\text{x}10^{16}$ cm^{3}µs^{-1} for 6 ppma oxygen, to $0.2\text{x}10^{16}$ cm^{3}µs^{-1} for 20 ppma. The oxygen concentration in multicrystalline ingots typically is between 10-20 ppma in the bottom, decreasing to less than 5 ppma in the top. [11] The value of N_t^*/N_A=$0.01\text{x}10^{16}$ cm^{3}µs^{-1} is therefore a representative value, and is used in Fig. 1b. In this case the the majority of the dependence of lifetime on resistivity arises from the chemical presence of boron in the defect itself, and not from the electronic properties of the defect. The increase of

lifetime with resistivity is slightly stronger than linear because the BO defect has an asymmetry of capture cross sections of a factor 9.3. [12]

Fig. 1 shows that the impact of both defects is similar for realistic defect densities. Clearly the balance will depend on the exact defect concentrations present in a particular material. For a precise analysis of their relative importance in multicrystalline material, the relation between N_t^*, oxygen concentration, and other material parameters would have to be known in more detail. Also, the Fe_i concentration in cells can vary rather strongly with process steps and process parameters.

We note that the Auger and radiative recombination lifetime[13] are much higher than the SRH lifetime in Fig.1, for resistivity higher than about 0.05 Ω-cm. Only for resistivity below 0.035 Ω-cm is the recombination rate from these processes higher than the SRH rate.

To illustrate how the dependence of lifetime on base resistivity can affect solar cells, Fig. 2 shows the calculated cell efficiency as a function of base resistivity. The cells were modeled with parameters typical for industrial processing, with a screen-printed Al-BSF modeled as a 9 micron thick region of high acceptor concentration ($4x10^{18}$ cm^{-3}) and low lifetime. [14] The calculations were performed in PC1D. [15] Three cases are compared: i) Fe_i recombination centers with a concentration of 10^{11} cm^{-3}, ii) BO centers with N_t^*/N_A =$0.01x10^{16}$ $cm^3\mu s^{-1}$, and iii) mid-gap recombination centers with $\sigma_n=\sigma_p$ and $\tau_{SRH} \approx 20$ μs (at 1.5 Ω-cm, only weakly dependent on base resistivity).

From plots like Fig. 2, for a range of defect concentrations, the optimal base resistivity as a function of defect concentration can be derived. The results are given in Fig. 3. Clearly, a higher Fe_i or BO concentration leads to a *higher* optimal base resistivity. Also shown, in Fig. 3b, is that, in contrast, for mid-gap recombination centers with $\sigma_n=\sigma_p$, where the bulk lifetime depends only weakly on base resistivity, a higher defect concentration leads to a *lower* optimal base resistivity.

It can be noted from Fig. 1 that recombination *only* due to Fe_i or BO leads to very high lifetime values for high base resistivity. Therefore this modelling results in rather high optimal resistivity values of 10 Ω-cm and higher. It is likely that in reality other impurities and defects will impose a cap on the actual bulk lifetime. The results of imposing such a lifetime cap in the modelling are also shown in Fig. 2 and Fig. 3. A cap does not change the qualitative behaviour of the dependence of optimal base resistivity on defect concentration in Fig.3, but it shifts the curve to lower values of optimal resistivity. In both cases, a relatively low cap of 20 μs can result in an optimum below 1 Ωcm. The position of the curves is influenced by the exact defect parameters, especially the energy level of the defect. The curves are rather independent of the model for the solar cell, except that if the model does not include rear surface passivation (such as the presence of a back surface field) there is no significant dependence of cell efficiency on bulk lifetime.

The behaviour described above for Fe_i is due to the fact that the hole capture cross section is much smaller than the electron capture cross section. Because of the small hole capture cross section, even though holes are majority carriers, their capture rate is limiting the recombination rate. This capture rate is proportional to the concentration of holes, which is in turn determined by the base doping.

If holes are the minority carrier their concentration will be determined by the injection level, and not by the base doping. In that case, a small hole capture cross section will result in a low recombination rate (high lifetime) *virtually independent* of resistivity. To illustrate this, Fig. 4 shows the lifetime in p-type and n-type silicon, both with $3x10^{11}$ cm^{-3} Fe_i impurities. The difference in lifetime between the two substrates is several orders of magnitude. Since Fe_i may be expected to be a dominant impurity in n-type silicon, too, this may explain the unusually high lifetimes recently observed in n-type silicon. [16]

It is important to note that Fe is representative for a wider range of impurities. The effects described in this paper are intrinsic properties of deep SRH centres with smaller cross sections for majority carriers than minority carriers. Many other transition metal contaminants in silicon have capture cross sections with asymmetry similar to Fe_i. [17]

In conclusion, asymmetrical capture cross sections of impurities, for electrons larger than for holes, provide an explanation for the empirical preference for higher resistivities in p-type solar grade silicon than might otherwise be expected.. It is also an explanation for remarkably high carrier lifetimes in n-type solar grade silicon. The physics of this effect is fundamentally different to and independent of chemical dopant-defect interactions such as occur with the BO defect. When impurities in silicon wafers are reduced (including the oxygen content), the optimal bulk resistivity may shift downwards, as indicated in Fig 3. The concentration of (active) defects can be reduced by, for example, improved silicon feedstock, improved ingot growth technology, improved gettering, or by hydrogen passivation. Therefore, the optimal resistivity determined empirically several years ago may have changed for the present wafer and cell production technologies.

References

1. Brody J, Rohatgi A, Yelundur V. Bulk resistivity optimization for low-bulk-lifetime silicon solar cells. *Progress in Photovoltaics: Research and Applications* 2001; **9**(4): 273-285.

2. Bothe K, Schmidt J, Hezel R. Comprehensive analysis of the impact of Boron and Oxygen on the metastable defect in Cz-Silicon. *3rd World Conference on Photovoltaic Energy Conversion, 11 - 18 May 2003, Osaka, Japan*, preprint, and references therein.

3. Dhamrin M, Akihide T, Hashigami H, Saitoh T. Light-induced lifetime degradation of commercial multicrystalline silicon wafers. *29th IEEE Photovoltaic Specialists Conference,* pp. 395-398 (2002).

4. Damiani BM, Light induced degradation in promising multi-crystalline silicon materials and cells. To be published in *Proceedings of the 3rd World Conference on Photovoltaic Energy Conversion*. May 11-13, 2003, Osaka, Japan.

5. Macdonald DH, Geerligs LJ, Riepe S. Light-induced lifetime degradation in multicrystalline silicon. *13th workshop on crystalline silicon solar cell materials and processes. Extended papers and abstracts.* NREL: Golden, 2002: 183-285.

6. Sopori BL, Jastrzebski L, Tan T. A comparison of gettering in single- and multicrystalline silicon for solar cells. *25th IEEE Photovoltaic Specialists Conference*, pp. 119-122 (1996). Geerligs LJ. Impact of defect distribution and impurities on multicrystalline silicon solar cell efficiency. To be published in *Proceedings of the 3rd World Conference on Photovoltaic Energy Conversion*. May 11-13, 2003, Osaka, Japan.

7. Blakemore JS. *Semiconductor Statistics. International Series of Monographs on Semiconductors, Vol 3.* Pergamon Press: Oxford, 1962.

8. Samudra G, et al. High-field electron transport for ellipsoidal multivalley band structure of silicon. *Journal of Applied Physics* 1992; **72** (10): 4700-4704.

9. Istratov A, Hieslmair H, Weber ER, *Applied Physics* 1999; **A 69**: 13. Macdonald D, Cuevas A, Wong-Leung J, *Journal of Applied Physics* 2001; **89**(12): 7932.

10. Ballif C, et al. Lifetime investigations of degradation effects in processed multicrystalline silicon wafers. *Proceedings of the 17th European Photovoltaic Solar Energy Conference.* WIP: Munich, 2002: 1818-1821. Geerligs LJ. Multicrystalline silicon: Relation between ingot quality and cell efficiency. *12th workshop on crystalline silicon solar cell materials and processes. Extended papers and abstracts.* NREL: Golden, 2002: 288-292.

11. Schönecker A, Geerligs LJ, Müller A. Casting technologies for solar silicon wafers: block casting and ribbon-growth-on substrate. *Solid State Phenomena* 2004; **95-96**: 149-158.

12. Rein S, Glunz SW. Electronic properties of the metastable defect in boron-doped Czochralski silicon: Unambiguous determination by advanced lifetime spectroscopy. *Applied Physics Letters* 2003; **82**: 1054-1056.

13. Kerr MJ, Cuevas A. *Journal of Applied Physics* 2002; **91**: 2473.

14. Tool CJJ, et al. Influence of wafer thickness on the performance of multicrystalline Si solar cells: an experimental study. *Progress in Photovoltaics: Research and Applications* 2001; **10**: 279-291. In the present paper, a higher diffusion length in the BSF - L_D=4.5 μm - is used because this fits the experimental internal quantum efficiency curves better.

15. PC1D v.5.5. Basore P, Clugston DA, University of New South Wales 2000.

16. Cuevas A, et al, Millisecond minority carrier lifetimes in n-type multicrystalline silicon. *Applied Physics Letters* 2002; **81**(26): 4952-4954. Libal J, et al., to be published.

17. Macdonald DH, et al. to be published.

Figure captions

Fig. 1.

Lifetime calculated as a function of base resistivity. a) For a concentration of $3x10^{11}$ cm^{-3} Fe_i impurities, according to eq. 1. For a fixed generation of 0.1 sun, the dependence on base resistivity is even stronger than for a fixed injection level. Base resistivity was related to dopant concentration N_A using PC1D. b) For the BO defect with normalized defect density $N_t^*/N_A=0.01x10^{-16}$ $cm^3/\mu s$ at $\Delta n=10^{15}$ cm^{-3}. For reference, a dotted line reproduces the 0.1 sun curve for Fe_i from a).

Fig. 2.

Cell efficiency calculated with PC1D as a function of base resistivity. a) For recombination via 10^{11} cm^{-3} Fe_i impurities, and for comparison, for recombination via mid-gap defects with $\sigma_n=\sigma_p$ and $\tau_{SRH} \approx 20$ μs at 1.5 Ω-cm, weakly dependent on resistivity. b) For the BO defect with normalized defect density $N_t^*/N_A=0.01x10^{-16}$ $cm^3/\mu s$ at $\Delta n=10^{15}$ cm^{-3}. An industrial cell process with Al-BSF rear surface passivation is modeled. The dotted line represents cell efficiency assuming a cap of 200 μs on the bulk lifetime.

Fig. 3.

a) Optimal base resistivity calculated as a function of Fe_i concentration, for cells as in Fig. 2. b) Optimal base resistivity calculated as a function of BO complex concentration, for cells as in Fig. 2. As a reference, also shown is the optimal doping as a function of defect concentration, for a mid-gap defect with $\sigma_n=\sigma_p$. Defect densities are represented as normalized values, i.e. as N_t^* at $N_A=10^{16}$ cm^{-3} for the BO complex, and as $1/\tau$ for the mid-gap defect.

The results are shown for modelling without bulk lifetime cap, and for caps of 200 and 20 μs.

Fig. 4.

Minority carrier lifetime calculated as a function of base resistivity in n- and p-type silicon, for a concentration of $3x10^{11}$ cm^{-3} of Fe_i. The calculations are for an injection level of $\Delta n=10^{13}$ cm^{-3}.

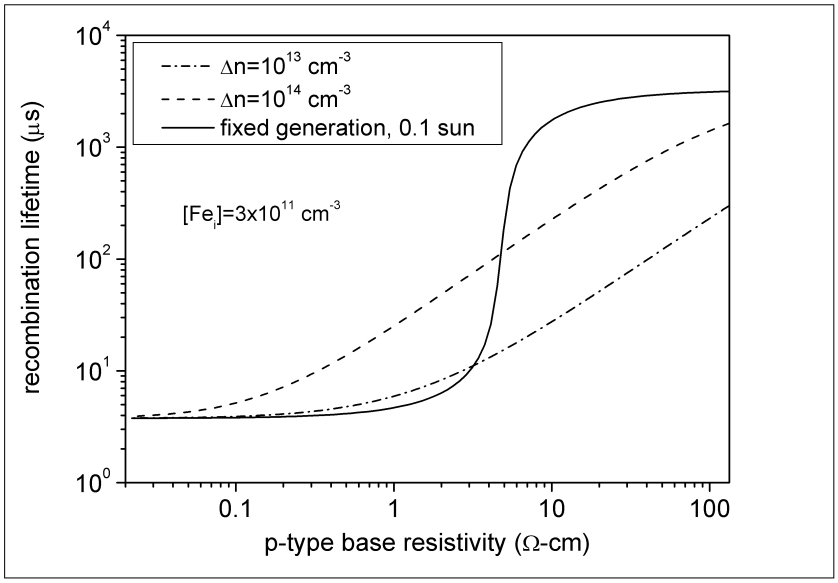
recombination lifetime (μs)
p-type base resistivity (Ω-cm)
Δn=10^13 cm^-3
Δn=10^14 cm^-3
fixed generation, 0.1 sun
[Fe_i]=3x10^11 cm^-3

Fig. 1a

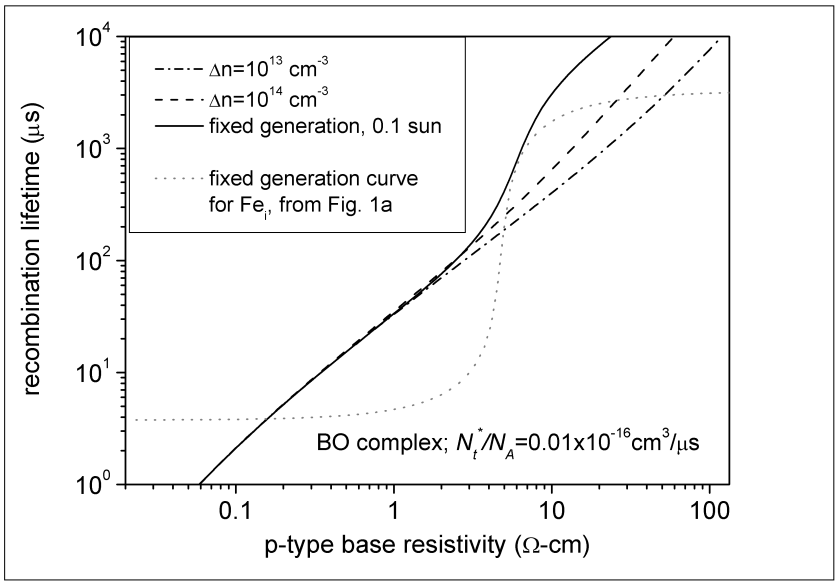
recombination lifetime (μs)
p-type base resistivity (Ω-cm)
Δn=10^13 cm^-3
Δn=10^14 cm^-3
fixed generation, 0.1 sun
fixed generation curve
for Fe_i, from Fig. 1a
BO complex; N_t*/N_A=0.01x10^-16cm^3/μs

Fig. 1b

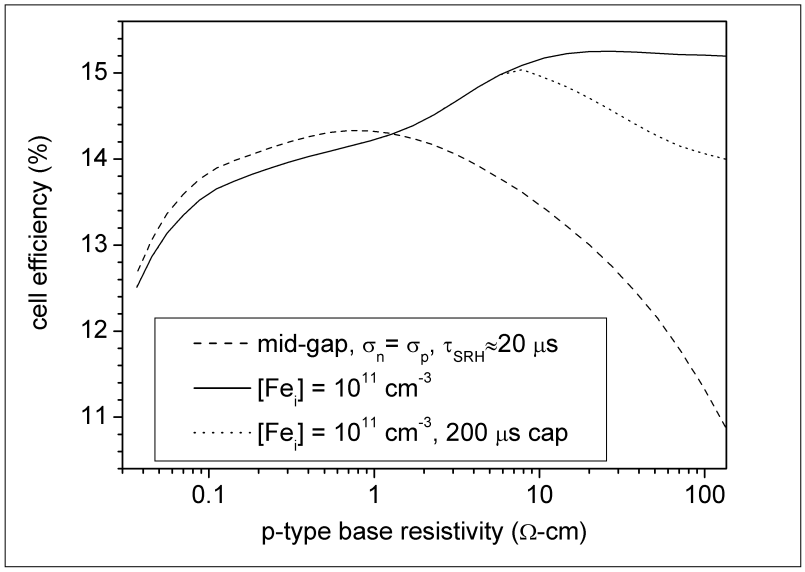
cell efficiency (%)
15
14
13
12
11
0.1
1
10
100
p-type base resistivity (Ω-cm)
mid-gap, σn = σp, τSRH≈20 μs
[Fei] = 10^11 cm^-3
[Fei] = 10^11 cm^-3, 200 μs cap

Fig. 2a

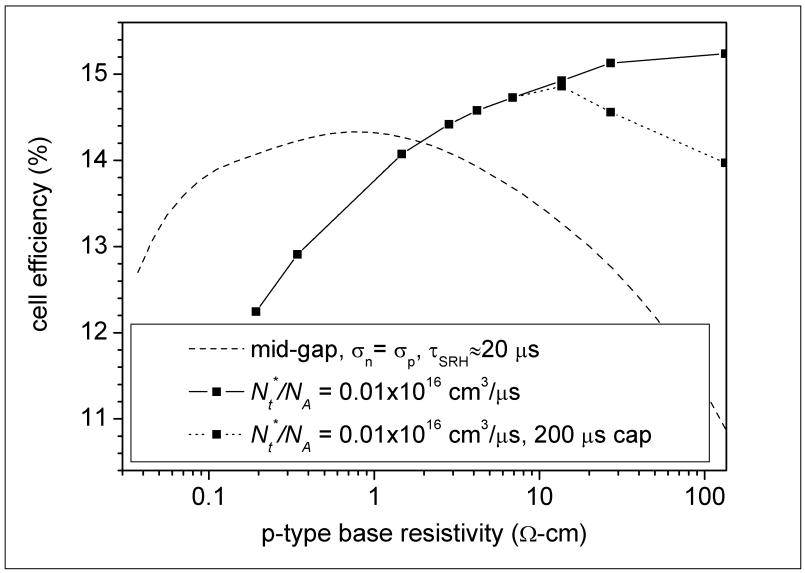
cell efficiency (%)
15
14
13
12
11
0.1
1
10
100
p-type base resistivity (Ω-cm)
mid-gap, σn = σp, τSRH≈20 μs
Nt*/NA = 0.01x10^16 cm^3/μs
Nt*/NA = 0.01x10^16 cm^3/μs, 200 μs cap

Fig. 2b

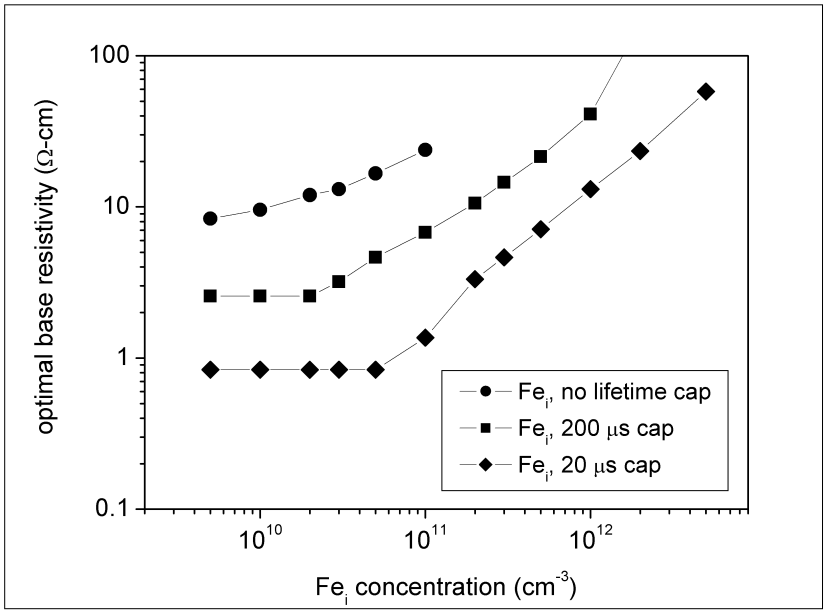
optimal base resistivity (Ω-cm)
100
10
1
0.1
10^{10}
10^{11}
10^{12}
Fe_i concentration (cm^{-3})
Fe_i, no lifetime cap
Fe_i, 200 μs cap
Fe_i, 20 μs cap

Fig. 3a

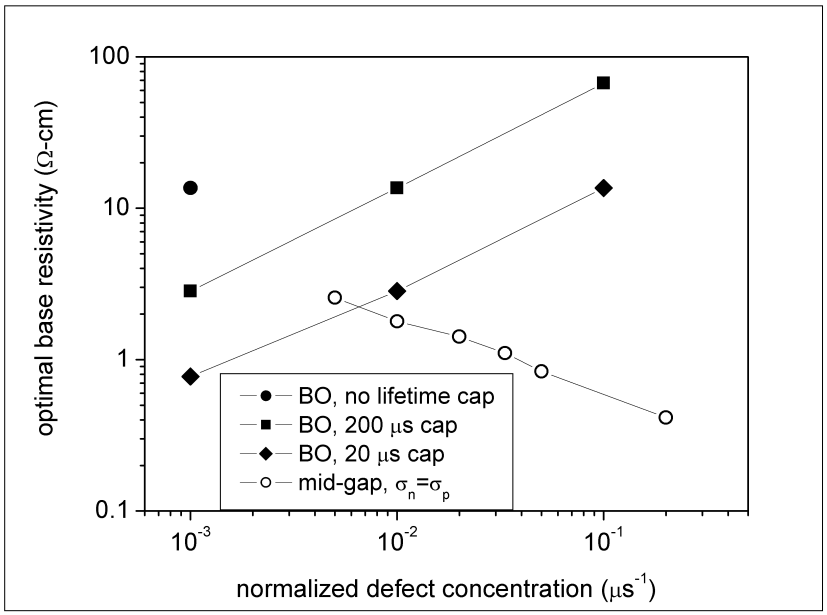
optimal base resistivity (Ω-cm)
100
10
1
0.1
10^{-3}
10^{-2}
10^{-1}
normalized defect concentration (μs^{-1})
BO, no lifetime cap
BO, 200 μs cap
BO, 20 μs cap
mid-gap, $\sigma_n=\sigma_p$

Fig. 3b

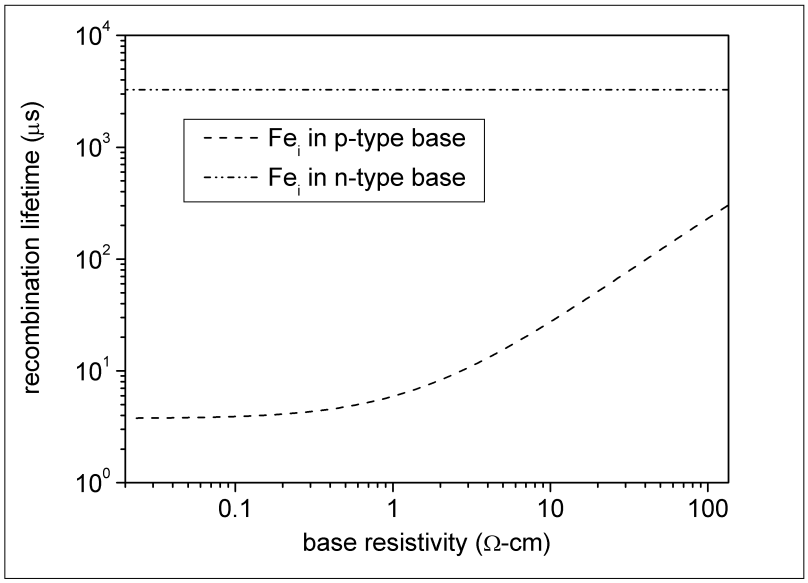
recombination lifetime (μs)
10^4
10^3
10^2
10^1
10^0
Fe_i in p-type base
Fe_i in n-type base
0.1
1
10
100
base resistivity (Ω-cm)

Fig. 4

5. RECOMBINATION ACTIVITY OF INTERSTITIAL IRON AND OTHER TRANSITION METAL POINT DEFECTS IN P- AND N-TYPE CRYSTALLINE SILICON

Daniel Macdonald

Department of Engineering, FEIT, The Australian National University, Canberra, ACT 0200, Australia

L. J. Geerligs

ECN Solar Energy, PO Box 1, NL-1755 ZG Petten, The Netherlands

Interstitial iron in crystalline silicon has a much larger capture cross section for electrons than holes. According to the Shockley-Read-Hall model, the low-injection carrier lifetime in p-type silicon should therefore be much lower that in n-type silicon, while in high-injection they should be equal. In this work we confirm this modeling using purposely iron-contaminated samples. A survey of other transition metal impurities in silicon reveals that those which tend to occupy interstitial sites at room temperature also have significantly larger capture cross sections for electrons. Since these are also the most probable metal point defects to occur during high temperature processing, using n-type wafers for devices such as solar cells may offer greater immunity to the effects of metal contaminants.

Published in Applied Physics Letters **85**, 4061-4063 (2004).

Metallic impurities are common in photovoltaic grade crystalline silicon. Neutron Activation Analysis[1,2] studies of directionally-solidified multicrystalline silicon have revealed, for example, significant quantities of Fe, Cr, Cu, Mo and Co. These contaminants are especially damaging when occurring at interstitial or substitutional lattice sites, since they may then be evenly distributed throughout the wafer. Precipitated metals may also be very active in terms of recombination, but at least in this case many impurity atoms are bound in one location.

Interstitial iron (Fe_i) is an especially common contaminant: it produces a deep level in the band-gap and has a much larger capture cross section for electrons than for holes[3]. According to the Shockley-Read-Hall model, this implies that the low-injection carrier lifetime should be much lower in *p*-type silicon (*p*-Si) than in *n*-type (*n*-Si). The purpose of this work is to confirm this modeling experimentally. In addition, it is shown that other metal contaminants which tend not to precipitate during cooling, and are therefore more likely to produce point-like defects, also have larger cross sections for electrons. It is precisely these types of impurities which are the most dangerous for devices which are sensitive to the bulk carrier lifetime, such as solar cells.

The recombination strength of a given impurity is determined by three parameters: the energy level and the capture cross sections for both electrons and holes. Deep Level Transient Spectroscopy (DLTS) has been applied to many metal impurities in silicon in recent decades, yielding much information about energy levels and majority carrier capture cross sections. In cases where minority capture was also studied, measurements were often performed well below room temperature (RT), and with strong electric fields (due to probing in the space-charge region). In only a few cases, such as for Ti and Zn[4,5], is the minority capture cross section also known from DLTS-like techniques under conditions applicable to the base region of solar cells (zero or small field and at RT). For some other impurities, the minority carrier cross sections under these conditions are known by carrier lifetime techniques. These values are collected in Table I for Fe[3], Cr[6,7], Ti[4], V[8,9], Mo[10], Zn[5] and Au[10]. Values from Refs. 5 and 7 are based on capture co-efficients $c_{n/p}$, converted to cross sections $\sigma_{n/p}$ using the thermal velocity[11] $v_{th} = 1.1\times10^{7}$cm/s.

For the case of Fe_i, the ratio of electron to hole capture cross sections, $k = \sigma_n / \sigma_p$, is approximately 700. Using these parameters, and the energy level, it is straightforward to model the injection-dependence of the excess carrier lifetime with the Shockley-Read-Hall (SRH) model[12-14]. For deep levels such as Fe_i, the low injection lifetime is limited by the capture of minority carriers, or electrons in *p*-Si. In high injection however, the lifetime is controlled by both the electron and hole capture rates. If the hole capture cross section is much smaller, it will dominate the high injection lifetime, making it relatively large. Consequently the lifetime will increase dramatically with injection level, as shown in Figure 1. In *n*-Si, on the other hand, the lifetime is controlled by hole capture across the entire injection range, making it independent of injection. Note that the ratio of the low-injection lifetimes in *n* and *p*-Si is equal to *k*.

To verify the modeling, samples containing Fe were prepared by ion-implantation with a dose of $10^{11}cm^{-2}$ and annealing at 900°C for 1 hour. After etching, plasma-enhanced chemical vapor-deposited SiN films were deposited for surface passivation. The float-zone (FZ) *n*-Si samples were of resistivity 2Ωcm (N_D=$2.4\times10^{15}cm^{-3}$) and 260 μm thickness, giving a distributed Fe concentration of $3.8\times10^{12}cm^{-3}$. The *p*-Si data is taken from Ref. 14, in which FZ wafers of 5Ωcm (N_A=$2.8\times10^{15}cm^{-3}$) and 290 μm thickness were used, giving a similar Fe concentration of $3.4\times10^{12}cm^{-3}$.

Effective carrier lifetimes t were measured using the quasi-steady-state photoconductance technique[15]. Control wafers without Fe implants were co-processed. By measuring the control and implanted wafers across the same injection range, the carrier lifetime due only to the introduced Fe_i (τ_{Fe}) can be extracted via $1/t_{Fe}=1/t_{implanted}-1/t_{control}$. This procedure subtracts out the influence of other recombination channels such as Auger and surface recombination. Figure 2 shows the result for the Fe-doped *n*-Si wafer. Figure 1 shows the results after the subtraction procedure for both *n*- and *p*-Si. The data for the boron-doped *p*-Si sample were taken after illumination to break the FeB pairs[16], which display an entirely different injection dependence[14].

The agreement between the model and the measured data is very good, especially considering the Fe_i concentration is determined by the dose, and is not a free parameter. Slight re-forming of FeB pairs (estimated to be approximately 10%) before measurement is probably the reason for the disagreement at higher injection levels for the *p*-type case. From this data we can extract a lower bound for the capture cross section ratio for Fe_i of $k>75$. The lifetime could not be measured at lower injection levels in the *p*-Si sample due to minority carrier trapping artifacts.

Many of the other transition metal impurities in Table I also have *k* values far from unity. Fig. 3 plots *k* as a function of the energy gap to the nearest band edge. The plot shows a striking trend: the donor levels all have $k>1$, while the acceptor levels have $k<1$. As recombination centers, donor levels alternate between a positively charged state which captures electrons, and a neutral state which captures holes. Since the charged state is more attractive to electrons than the neutral state is to holes, it seems reasonable to have $k>1$. The opposite occurs for the acceptor levels. Note also that double donors and acceptors, which are doubly charged, have even more extreme *k* values.

Graff[10] and Lemke[17] have noted that, in general, metals from Group 8 or less on the periodic table are more likely to produce donor states, while those from Group 9 or higher generally produce acceptor states, as reflected in Table I. There are numerous exceptions to this trend, for example Ti and V (Groups 4 and 5) exhibit both donor and acceptor states. However, their acceptor states are quite shallow[10], and are unlikely to dominate the recombination activity of these metals. Hence it is generally true that the most recombination-active levels of transition metals from Group 8 and below are donor states.

Graff[10] and Lemke[17] have also observed that transition metals from Group 8 or below tend to form moderate concentrations of interstitial centers at RT after high temperature processing, while

those from above Group 8 generally form precipitates and much lower concentrations of substitutional centers. This occurs because the diffusivities of the latter are significantly higher. Since their diffusion length is still high at temperatures where the solubility becomes extremely small, almost complete precipitation of the interstitial atoms occurs. As a result, only the very small fraction which occupied substitutional sites prior to quenching remains in solution. Such behavior is well known for Co, Ni and Cu (Groups 9, 10 and 11) for example[18].

Thus there is an apparent coincidence in Table I: metals from Group 8 and below are both donor-like and interstitial at RT, whereas those from above Group 8 are acceptor-like and substitutional at RT. As a result of being donor-like, the interstitial metals have large values of k, while the RT substitutional metals are acceptor-like with $k \ll 1$. This observation has profound implications for their recombination activity: the interstitial metals are, generally, more detrimental in p-Si, while the substitutional metals have a greater impact in n-Si. Itsumi[19] came to similar conclusions for the specific cases of Fe, Ni and Cu. Since the interstitial impurities are likely to occur in much higher concentrations than the substitutional ones (from the precipitation argument above), they are the most important point-like metal contaminants technologically. Notwithstanding the impact of precipitates, whose relative recombination activity in n- and p-Si is not well established, this supports the use of n-Si for devices such as solar cells. It may also explain the recently observed very high lifetimes in n-type multicrystalline silicon[20].

A further observation from Fig. 3 is that deeper energy levels have greater values of k. This is less easily explained, but is related to the details of the capture process, since cascade, multi-phonon or impurity-mediated Auger mechanisms lead to different models for how capture cross sections depend on the defect depth[21]. It can also be observed from Table I that, for the case of donor states, the major part of this effect is due to the variation in σ_p, while σ_n is relatively constant. This may be related to the fact that, for donor levels, the degree of coulombic attraction for electrons is not influenced strongly by the level depth, while the transition probability for a neutral (hole) capture process will be.

Although 'deep' levels with $k>1$ will display the same general injection-dependent behavior as Fe_i in Fig 1, shallower levels can be more complex due to interactions with the Fermi level. They may have an injection dependence that either increases or decreases, depending on the resistivity[8]. Since many of the other levels in Table I are not especially deep, it is important to apply the SRH model for each to determine if they result in a 'preference' for n-Si over p-Si. With $N_{A/D} = 1\times10^{16}cm^{-3}$, it is indeed true that V, Mo and both levels of Ti produce much greater recombination in p-Si. The opposite is true for the acceptor levels of Au and Zn.

Naturally, the performance of a solar cell depends on many parameters other than the low-injection lifetime in the base. Firstly, it is often the diffusion length L_D, rather than carrier lifetime τ, that determines the cell current. Since the minority carrier diffusivity D in n-Si is typically a factor of 3 lower than in p-Si, the lifetime must increase by a factor of 3 to achieve the same diffusion

length ($L_D = [Dt]^{1/2}$). Note that, except for Cr, all of the interstitial impurities shown in Table I have $k > 3$. Another consideration is that solar cells generally operate at moderate injection where the difference between *n*- and *p*-type lifetimes is not as large as in true low injection. In addition, recombination in other parts of a device may mask the impact of base recombination. It is also known that interstitial impurities can be removed by the gettering action of highly-doped regions, and some metals, such as Fe_i, are effectively hydrogenated during cell processing[22]. Nevertheless, industrial phosphorus diffusions are often too rapid to allow complete gettering, and similarly hydrogenation may be incomplete or ineffective for some metals. It is therefore conceivable that interstitial metals will, in some cases, impact on cell performance.

In conclusion, transition metal contaminants from Group 8 and below on the periodic table are the most likely to produce relatively large concentrations of point defect recombination centers in crystalline silicon. These are interstitial in nature, and correspond to those metals which tend to produce donor states, and therefore have much greater recombination strength in *p*-Si than *n*-Si. If the presence of these impurities dominates cell performance, then *n*-Si may prove to be a better choice of solar cell substrate.

This work has been supported by the Australian Research Council and The Netherlands Agency for Energy and the Environment.

References

1 A. A. Istratov *et al.*, J. Appl. Phys. **94**, 6552 (2003).

2 D. Macdonald *et al.*, in *Proceedings of the 29th Photovoltaic Specialists Conference* New Orleans, LA (IEEE, New York, 2002), p. 285.

3 A. A. Istratov, H. Hieslmair and E. R. Weber, Appl. Phys. A, **69**, 13 (1999).

4 A. C. Wang, L. S. Lu and C. T. Sah, Phys. Rev. B **30**, 5896 (1984).

5 C. T. Sah, *et al.,* IEEE Trans. Elec. Dev. **28**, 304 (1981).

6 H. Conzelmann, K. Graff and E. R. Weber, Appl. Phys. A, **30**, 169 (1983).

7 K. Mishra, Appl. Phys. Lett., **68**, 3281 (1996).

8 L. Tilly *et al.,* Phys. Rev. B, **44**, 12809 (1991).

9 J. P. Kalejs *et al.*, in *Conference Record of the 23rd IEEE Photovoltaic Specialists Conference*, Louisville, KY (IEEE, New York, 1993), p. 184.

10 K. Graff, *Metal Impurities in Silicon Device Fabrication*, Springer Series in Materials Science, Second Edition, (Springer-Verlag, Berlin, 2000).

11 W. M. Bullis and H. R. Huff, J. Electrochem. Soc. **143**, 1399 (1996).

12 W. Shockley and W. T. Read, Phys. Rev. **87**, 835 (1952).

13 R. N. Hall, Phys. Rev. **87**, 387 (1952).

14 D. Macdonald, A. Cuevas and J. Wong-Leung, J. Appl. Phys. **89**, 7932 (2001).

[15] R. A. Sinton and A. Cuevas, Appl. Phys. Lett. **69**, 2510 (1996).

[16] G. Zoth and W. Bergholz, J. Appl. Pjys. **67**, 6764 (1990).

[17] H. Lemke, in *Semiconductor Silicon/1994,* Edited by H. R. Huff, W. Bergholz and K. Sumino (The Electrochemical Society, New Jersey, 1994) p. 695.

[18] A. A. Istratov and E. R Weber, Appl. Phys. A, **66**, 123 (1998).

[19] M. Itsumi, Appl. Phys. Lett. **63**, 1095 (1993).

[20] A. Cuevas *et al*., Appl. Phys. Lett. **81,** 4592 (2002).

[21] A. Hangleiter, Phys. Rev. B, **37**, 2594 (1988).

[22] A. Azzizi, L. J. Geerligs and D. Macdonald, to be published in *Proceedings of the 19th European Photovoltaic Solar Energy Conference*, Paris (2004).

Table I: *Recombination parameters of point-like metal impurities in crystalline silicon at RT.*

Impurity	RT lattice site	Type	Group	Energy (eV)	s_n (cm^2)	s_p (cm^2)	$k = s_n/s_p$
Ti	interstitial	donor	4	E_C-0.27	3.1×10^{-14}	1.4×10^{-15}	22
	interstitial	d. donor		E_V+0.26	1.3×10^{-14}	2.8×10^{-17}	460
V	interstitial	d. donor	5	E_V+0.36	5×10^{-14}	3.0×10^{-18}	17000
Cr	interstitial	donor	6	E_C-0.22	2.3×10^{-13}	1.1×10^{-13}	2
Mo	interstitial	donor	6	E_V+0.28	1.6×10^{-14}	6.0×10^{-16}	30
Fe	interstitial	donor	8	E_V+0.38	5×10^{-14}	7×10^{-17}	700
Au	substitutional	acceptor	11	E_C-0.55	1.4×10^{-16}	7.6×10^{-15}	0.02
Zn	substitutional	acceptor	12	E_V+0.33	1.5×10^{-15}	$4.4\times10^{-$	0.34
	substitutional	d. acceptor					0.00002

Figure Captions

FIG 1. Modeled and measured lifetimes for Fe_i in n and p-type silicon.

FIG 2. Measured control and implanted lifetimes, and calculated lifetime due to Fe_i only (τ_{Fe}) for the n-Si sample.

FIG 3. Capture cross section ratio as a function of energy level depth for impurities in Table I.

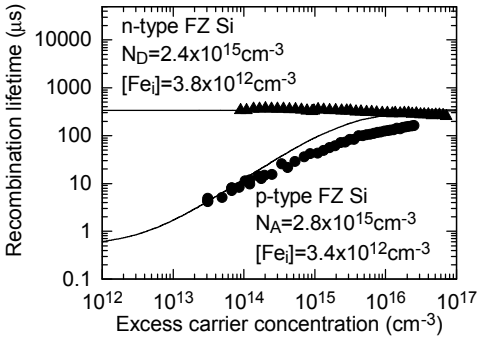

Fig. 1. Macdonald and Geerligs, Applied Physics Letters

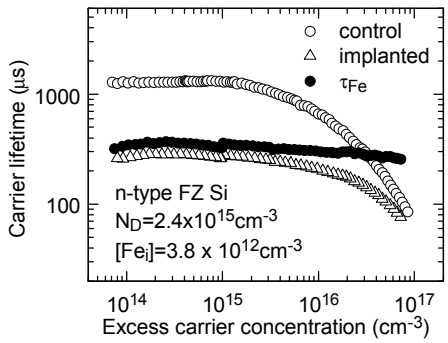

Fig. 2. Macdonald and Geerligs, Applied Physics Letters

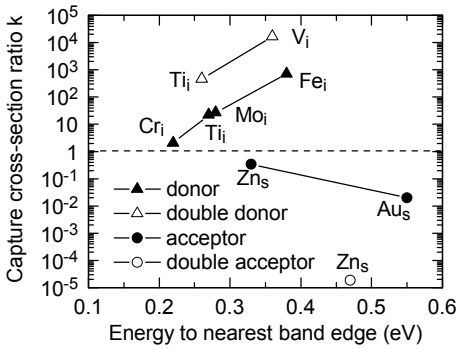

Fig. 3. Macdonald and Geerligs, Applied Physics Letters

6. LIGHT-INDUCED LIFETIME DEGRADATION IN MULTICRYSTALLINE SILICON

D. H. Macdonald[1], L. J. Geerligs[1] and S. Riepe[2]

[1]ECN Solar Energy, PO Box 1, NL-1755 ZG Petten, The Netherlands

[2]Fraunhofer ISE, Heidenhofstr. 2, 79110 Freiburg, Germany

Abstract

The correlation between interstitial oxygen content and light-induced lifetime degradation in cast multicrystalline silicon is complex. On a wafer-averaged scale, there is a strong positive correlation, which has been parameterized in this paper to model the impact of this degradation on cell voltage for a typical industrial process. However, on a local, grain to grain scale within a given wafer, the degradation can vary by an order of magnitude, while the interstitial oxygen content remains almost unchanged. This supports recent suggestions that O_i is not directly involved in the chemical composition of the defect.

Published in the 13th Workshop on Crystalline Silicon Solar Cell Materials and Processes. August 10th-13th, 2003. Vail, Colorado, USA (published by NREL, Golden, Co).

Light-induced degradation is a well-known phenomenon in boron-doped Czochralski (Cz) silicon [1], reducing the carrier lifetime and hence the cell efficiency. It has been linked to the presence of both boron and interstitial oxygen O_i, the latter being relatively abundant in standard Cz material. Degradation occurring under illumination of around 1 sun intensity takes approximately 24 hours to reach saturation. Since carriers injected through biasing also cause this degradation, the effect has become more properly known as "carrier-induced degradation" (CID) [2], as it is referred to in this paper from this point on. The initial non-degraded state can be recovered by annealing the sample above 200°C.

The extent of CID is characterized by the relative recombination center density N_t*, which is defined as the difference of the inverse lifetimes before (τ_b) and after (τ_a) degradation [1]:

$$N_t^* = \frac{1}{\tau_a} - \frac{1}{\tau_b}$$

In Cz-Si, this parameter has a clear linear dependence on the boron concentration NA, implicating the presence of B atoms in the defect composition. It also shows a dependence on the value of $[O_i]$, but usually with much more scatter. This indicates that O_i itself may not to be directly involved in the defect, but occurs in association with it. Recently, the oxygen dimer [3] and intrinsic point defects [4] have been suggested as possible alternatives.

Similar degradation has been reported in cast multicrystalline silicon (mc-Si) [5,6]. The effect in mc-Si has been shown to be reversible upon annealing, as it is with Cz-Si, and the rate at which the degradation occurs is similar in both materials. These facts suggest that the defect is indeed the same. In this paper, we examine the relationship between the degradation in mc-Si and the interstitial oxygen content, on both a macroscopic level (averaged across a wafer), and from grain to grain. The results allow some insights into the possible composition of the defects. The determined dependence of the average degradation on [Oi] also allows cell performance to be modeled, and criteria for acceptable [Oi] levels in ingots to be established.

Fig 1 shows the interstitial oxygen profiles measured by Fourier-Transform Infrared spectroscopy (FTIR) for 3 mc-Si ingots from different manufacturers. The concentration at the bottom of ingot 3 is high even by Cz-Si standards. Fig 2 shows the effect of illumination on the effective lifetime for wafers from these ingots, as well as a Cz wafer ($[O_i]$=10ppma) and a Float-zone (FZ) wafer ($[O_i]$<1ppma). The lifetimes represent area-averaged values of several grains, measured with the QSSPC technique at an excess carrier density of 3×10^{15} cm^{-3}. The FZ wafer showed no degradation, due to its low interstitial oxygen content, and confirms that the drop in lifetime observed in the other samples is not caused by changes in the surface passivating film (PECVD SiN), or by sample heating during illumination.

After 150 minutes illumination the samples were annealed at 250°C for 15 minutes, which caused the lifetimes to recover. Note also that the rate of lifetime decay is similar for the mc-Si and Cz samples, confirming that the defects are most likely the same. The two mc-Si wafers with the lowest lifetimes were sister wafers from the same ingot. One was measured without processing (other than etching, cleaning and surface passivating PECVD SiN deposition), and the other after emitter diffusion and hydrogenation by spike firing a SiN film, in similar fashion to industrial processing. The extent of CID is almost identical in these two wafers, suggesting that neither gettering nor bulk hydrogenation significantly reduce CID in this material.

A further point of interest in Fig 2 is the sudden increase in lifetime of the mc-Si wafers within the first few minutes. This effect is almost completely absent in the FZ and Cz wafers. By analyzing the decay behavior of this initial change we have confirmed that it is caused by the splitting of FeB pairs [7]. At the injection level measured, FeB pairs are more strongly recombining than interstitial Fe, and so the lifetime increases after breaking the FeB pairs. After degradation for 150 minutes, the sample was allowed to relax in the dark for 24 hours, long enough for the pairs to re-form, as shown in Fig 3. The lifetime could then be recovered again after 5 minutes further illumination. Fortunately, the very different time constants of the FeB splitting and CID allow them to be studied independently.

By the use of lifetime mapping techniques, such as Carrier Density Imaging (CDI) [8] and Modulated Free-Carrier Absorption (MFCA), it is possible to study the degradation on a local scale, as shown in Fig 4. The first two maps show CDI images of the carrier lifetime before and after degradation for 16 hours. The third map shows the local N_t* calculated using the expression above. The CDI images took approximately 3 min to capture, meaning that the FeB pairs were fully dissociated for almost the entire measurement time (dissociation is complete within tens of seconds in most cases).

In contrast to the QSSPC technique, both CDI and MFCA operate under fixed generation (equivalent to 1 sun in these measurements). This means that wafers or grains with higher lifetimes will be in higher injection, which will produce a greater apparent value for Nt*, as has been shown by Rein et al. [9]. We estimate that these effects will produce an overestimation of N_t* in the high lifetime regions of up to 50% for the conditions in this study. The overestimation would be less for lower lifetime grains and wafers. Unfortunately, this distortion is difficult to avoid when using mapping techniques.

The image clearly shows a large variation in N_t* from grain to grain. Some high lifetime grains remained almost unchanged, while others degraded strongly. This is indicated on the left of Fig 5, which reveals little correlation between N_t* and the initial lifetime. After degradation (right of Fig 5), all points lie below the limit imposed by the CID in parallel with a lifetime cap of 100ms due to surface recombination. Many points lie well away from this curve, meaning other bulk recombination centers, such as Fe, are also important in these regions.

It is instructive to match local N_t* data from lifetime maps with $[O_i]$ measurements made within a 5mm region of individual grains, as shown in Fig 6 (note that 1ppma $[O_i] = 5\times10^{16}$ cm^{-3}). The corresponding N_t* data were averaged over the same intra-grain regions. Several wafers from a single ingot are shown, as well as a Cz wafer. The mc-Si wafers were emitter diffused, stripped, and hydrogenated, and so should be representative of final cell substrates. In this figure, the parameter N_t*/N_A has been plotted to remove the influence of the boron concentration [4]. The data sets with error bars were measured with CDI, while the others are based on MFCA maps. The uncertainties are similar in both cases. The wafer from the top of the ingot was measured with both techniques, as shown on the plot, resulting in good agreement for local Nt* values.

The trend of increasing average degradation with increasing average $[O_i]$ is clearly evident. In the high $[O_i]$ region, the data agrees reasonably with fits for Cz-Si derived by Rein et al [4] and Bothe et al. [3]. The latter defined two fits, one for low $[O_i]$ which is almost linear, and another for high $[O_i]$ which is almost quadratic and aligns with Rein's fit. This shifting from a linear to a quadratic dependence is in accord with a proposed relationship between $[O_i]$ and the oxygen dimer concentration [3]. Such a shift is also reflected in our data for mc-Si. The apparent systematic overestimation in N_t* in our data is partly due to the effect of using constant generation described above. However, this effect is not likely to explain the entire difference. The remaining difference could be caused a different relationship between $[O_i]$ and CID in mc-Si compared to Cz-Si. At lower values of $[O_i]$, the magnitude of the lifetime is generally higher, meaning the constant-generation overestimation is greater. This could partly explain the apparent sub-linearity of our data in the low $[O_i]$ region.

Within any single wafer, the value of $[O_i]$ did not vary nearly as strongly as N_t*. In fact, for each of the individual sets of data in Fig 6, there appears to be no significant correlation at all between local $[O_i]$ and local N_t*/N_A. This supports the suggestion that O_i is not involved in the defect.

To model the impact of CID on industrial mc-Si solar cells, it is useful to determine an empirical relation between N_t*/N_A and $[O_i]$. A convenient way to characterize a dependence

which changes from near linear to near quadratic is through an exponential fit, as shown on Fig 6, of the form:

$$\frac{N_t^*}{N_A} = 0.0045 \exp(3 \times 10^{-18} \times [O_i])$$

Fig 7 shows the impact of CID on cell VOC, with several curves for different values of the area-averaged, non-degraded lifetime. In these PC1D simulations, typical optical and electronic parameters for SiN fired-through metallisation cells have been assumed. To allow a realistic simulation, we have assumed a modified Gaussian lifetime distribution before and after degradation [10,11]. The impact of these lateral variations on cell performance is accounted for by determining the area-averaged J_{0bulk} values [12], as calculated via PC1D, rather than using area-averaged lifetime values. The reduced lifetimes corresponding to these averaged J_{0bulk} values are shown on the plot.

Due to the constant generation artifact, the expression above will somewhat overestimate the degradation for a given $[O_i]$ value. For higher $[O_i]$ values, this error is only slight, and for lower $[O_i]$ values the impact of the degradation on cell voltage is negligible anyway. Therefore it should not significantly affect Fig 7.

The V_{OC} for the highest lifetime case shown is limited at low $[O_i]$ content to around 613mV by emitter and BSF recombination. Typical mc-Si material has initial area-averaged bulk lifetimes in the 30-100ms range. For the 30ms case, CID would reduce the V_{OC} from 593 to 588mV when $[O_i]= 7\times10^{17}$ cm^{-3} (14ppma). A similar 5mV drop for 100ms material (from 605 to 600mV) would occur at 4×10^{17} cm^{-3} (8ppma). These restrictions would become greater in more homogeneous material, since the modified Gaussian distribution assumed here tends to obscure the effect due to low lifetime regions which dominate the voltage. A further point to consider is if the interstitial oxygen content is very high, there is likely to be an observable link between the starting lifetime itself and $[O_i]$. For low and moderate values of $[O_i]$, this link is obscured by the presence of other defects.

In summary, the wafer-averaged carrier-induced degradation in mc-Si exhibits a super-linear dependence on $[O_i]$, becoming approximately quadratic at higher $[O_i]$ values. From grain to grain however, there is great variation in the extent of degradation, suggesting $[O_i]$ is not directly involved in the defect. As a rule of thumb, it seems that if the $[O_i]$ content is kept below

10ppma, typical industrial mc-Si cells will not be adversely affected. However, as cell designs improve and material becomes more uniform, [O_i] may need to be kept below 5ppma.

This work has been supported by NOVEM under contract 2020.01.13.11.2002. The authors are grateful to ECN staff for wafer processing and to S. W. Glunz for helpful suggestions.

[1] J. Schmidt et al, 26th IEEE PVSC, Anaheim (1997).
[2] S. W. Glunz et al, 3rd World Conf. On Photovoltaic Energy Conversion, Osaka, 2003.
[3] K. Bothe et al, 3rd World Conf. On Photovoltaic Energy Conversion, Osaka, 2003.
[4] S. Rein et al, 3rd World Conf. On Photovoltaic Energy Conversion, Osaka, 2003.
[5] H. Nagel et al, 14th EC-PVSEC, 762-765 (1997).
[6] M. Dhamrin et al, 29th IEEE PVSC, New Orleans, 2002.
[7] D. Macdonald et al, submit. to J. Appl. Phys.
[8] J. Isenberg et al, J. Appl. Phys, 93, 4268 (2003).
[9] S. Rein et al, 17th EC-PVSEC, Munich (2001).
[10] P. E. Mijnarends, et al, Sol. Energy Mat. and Solar Cells 33, 345-360 (1994).
[11] J. Isenberg et al, 17th EC-PVSEC, Munich (2001).
[12] R.A Sinton, 3rd World Conf. On Photovoltaic Energy Conversion, Osaka, 2003

Figure Captions

Fig 1. Interstitial oxygen content of mc-Si ingots from different manufacturers.

Fig 2. Carrier-induced degradation in various mc-Si, Cz and FZ wafers.

Fig 3. Details of lifetime changes due to FeB splitting and carrier-induced degradation.

Fig 4. CDI images of a wafer from the top of ingot 3. The images on the left are lifetime maps before and after degradation (μs). The image on the right is the relative defect concentration N_t*.

Fig 5. Scatter plot of local initial and degraded lifetimes (μs) versus local N_t*, taken from a line scan through Fig 4.

Fig 6. Correlation between local [O_i] and N_t*/N_A as measured with the CDI and MFCA techniques. All mc-Si wafers are from ingot 3. The black line is an exponential fit to the averages. The gray lines are fits to Cz data by Rein et al. and Bothe et al.

Fig 7. Modelled VOC as a function of [Oi] for standard SiN coated industrial mc-Si cells with modified-Gaussian lifetime distributions.

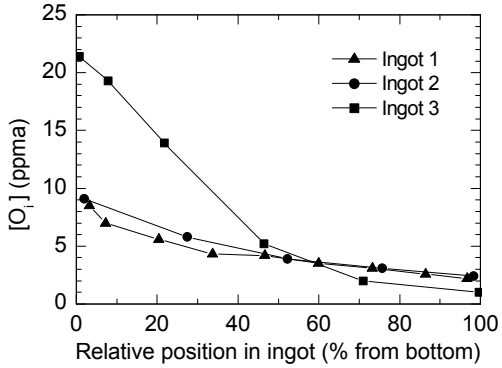

Figure 1

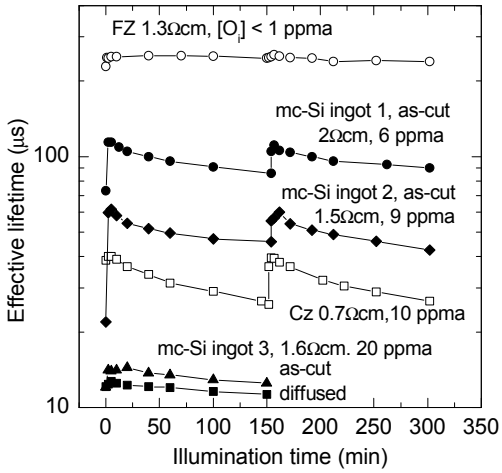

Figure 2

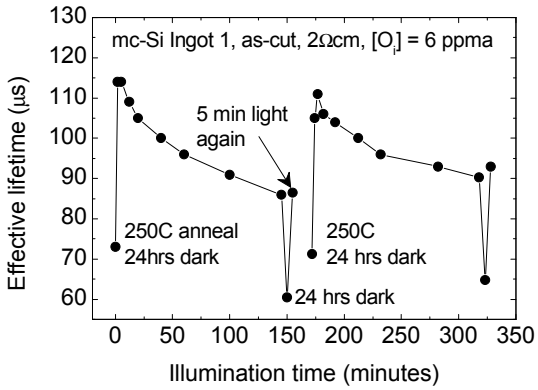

Figure 3

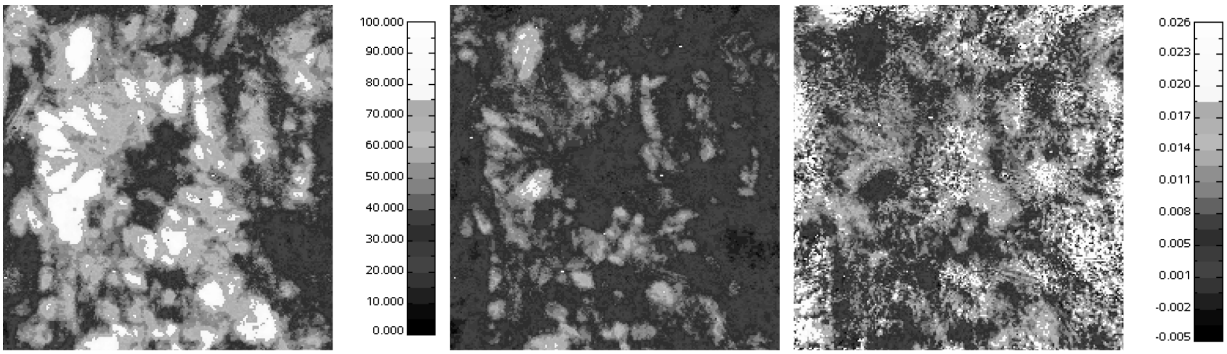

Figure 4

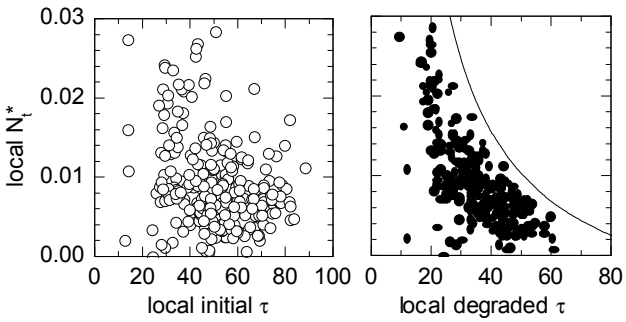

Figure 5

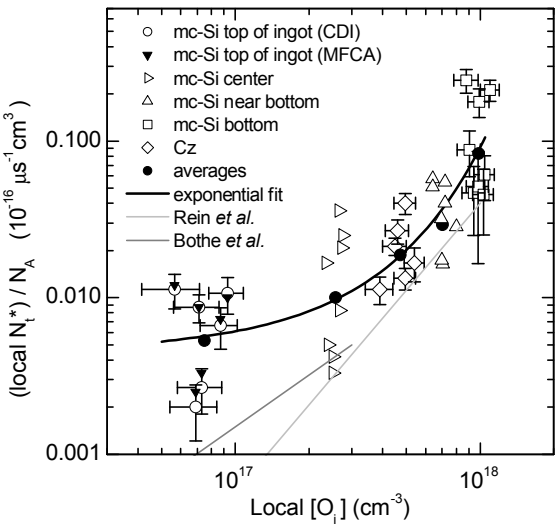

Figure 6

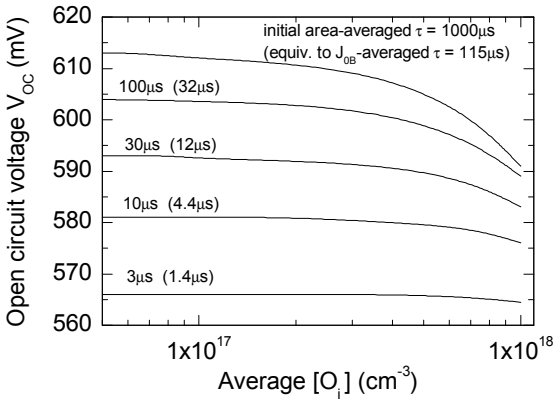
initial area-averaged τ = 1000μs
(equiv. to J0B-averaged τ = 115μs)
100μs (32μs)
30μs (12μs)
10μs (4.4μs)
3μs (1.4μs)
Open circuit voltage VOC (mV)
620
610
600
590
580
570
560
1x10^17
1x10^18
Average [Oi] (cm^-3)

Figure 7

7. HYDROGEN PASSIVATION OF IRON IN CRYSTALLINE SILICON

A. Azzizi[1], L. J. Geerligs[1], and D. Macdonald[2]

[1]ECN Solar Energy, PO Box 1, NL-1755 Petten, the Netherlands

[2]Dept of Engineering, The Australian National University, Acton ACT 0200, Australia

ABSTRACT

Hydrogen passivation of iron in silicon is investigated by measuring the recombination-active FeB-concentration with the light-induced FeB-dissociation technique. Floatzone wafers were intentionally contaminated with iron. Hydrogen passivation by annealing of the wafers with an SiNx coating leads to a decrease of the FeB concentration with about a factor 3 (from $1.2x10^{13}$ cm^{-3} to about $4.5x10^{12}$ cm^{-3}). Multicrystalline silicon wafers without an intentional iron contamination show a similar decrease of the measured iron concentration after annealing with SiNx coating. Based on these results, we conclude that the FeB defect is passivated by hydrogen in-diffusion after anneal of SiNx layers.

Keywords: iron, hydrogen passivation

Published in the proceedings of the 19th European Photovoltaic Specialists Conference, Paris, June 2004, pp. 1021-1024.

1 INTRODUCTION

The incorporation of hydrogen into multi-crystalline (mc) silicon materials leads to deactivation of certain impurities and defects and to passivation of grain boundaries [1-3]. However, it is challenging to monitor the process quantitatively. Various attempts have been made in this direction. For example, FTIR measurements of PtH complexes can trace diffusion of hydrogen, but this technique requires samples in which Pt is artificially in-diffused and measurements at cryogenic temperatures [4]. SIMS measurements of deuterium (D) is a straightforward approach, but in many materials with relatively low defect density, too little D is trapped and this technique has insufficient sensitivity [5].

In this paper we present experiments which show that another impurity than Pt can be used to trace diffusion of hydrogen, namely Fe. Virtually all mc-Si materials already contain interstitial Fe in measurable concentrations. As is well known, the concentration of interstitial Fe, paired with B acceptors, can be measured sensitively via minority carrier lifetime measurements (shortly reviewed below). Therefore, if interstitial FeB pairs are susceptible to hydrogen-passivation, and if this passivation can be measured conveniently, it is an ideal probe to study hydrogen diffusion in silicon.

In this article we present results of hydrogen passivation of iron in silicon. These results extend our preliminary results published earlier [6]. Two types of materials are used for investigation: FZ-wafers which are intentionally contaminated with iron, and several types of mc-Si wafers with different iron concentration. The mc-Si wafers are not intentionally contaminated; they contain only the Fe present due to the feedstock and the growth process.

DLTS (deep level transient spectroscopy) measurements indicate that several iron-related states exist in silicon; levels at E_v+0.1eV and E_v-0.23eV which are attributed to the Fe-B pairs, and a level at E_v+0.43, which is related to the interstitial (Fe_i) [7]. Pearton et al reported that a hole trap at E_v+0.4eV and E_v+0.33eV was passivated by exposure to a hydrogen plasma [8]. While E_v+0.33eV is assumed to be a complex of iron with oxygen [7], E_v+0.4eV has not been assigned. However, they did not confirm the passivation of the interstitial state at E_v+0.43eV. Kouketsu et al. reported the hydrogen passivation of the FeB pair levels with implanted hydrogen [9].

While DLTS is a very sensitive technique, it requires significant sample preparation time, and results are often difficult to interpret for multicrystalline silicon. However, the technique based on measurement of the minority carrier lifetime before and after light-induced FeB-dissociation is also very effective in determining very low FeB concentrations (as low as $5x10^{10}$ cm^{-3}), and has been shown to work well on monocrystalline as well as multicrystalline material. Due to various sources of contamination, Fe is always present in multicrystalline silicon, usually with concentrations of interstitial Fe above $1x10^{11}$ cm^{-3}, which is easily measurable. At room

temperature the interstitial Fe is paired with boron acceptors forming FeB pairs. Strong optical illumination (> 0.1Wcm^{-2}) leads to the complete (>99%) dissociation of the FeB pairs [10]. This dissociation causes significant changes in minority carrier lifetime. The FeB concentration can be found from the change in lifetime as:

$$[FeB] = C.\left[\frac{1}{\tau_1} - \frac{1}{\tau_0}\right]$$

where τ_0 and τ_1 are the measured minority carrier lifetimes before and after the dissociation by illumination. The pre-factor C is known from literature and should be taken at the actual injection level where the minority carrier lifetime was measured. The measurement of FeB pairs via lifetime has the advantages of being fast, non-contact, non-destructive and possible at room temperature.

The injection level-dependent lifetime curves of FeB and Fe_i recombination centres show characteristic behaviour (their shape, and the existence of a so-called cross-over point) which is can be used for identification [10]. The results obtained in multicrystalline material as well as intentionally contaminated monocrystalline material in this paper showed such behaviour.

Finally, it should be noted that our experiment only uses the FeB measurement to monitor the hydrogen passivation process. We have not quantitatively determined which changes in the Fe-related levels (position, cross section) occur due to passivation.

2 EXPERIMENT

FZ wafers with a p-type resistivity of 1Ω.cm were contaminated by immersing in $FeCl_2$ solution for about 10min. After drying with N_2, the wafers were annealed in a furnace at 900°C for 40 minutes. After anneal, the wafers were rapidly cooled down to room temperature. This cool-down rate is estimated to be 120°C/sec, enough to avoid precipitation of interstitial iron in the critical region (500-600°C) [11]. 30μm was removed from each side of the wafer to avoid any later effects of the Fe-contaminated surface layer. This procedure resulted in a range of 1-2×10^{13} cm^{-3} in Fe.

Multicrystalline wafers were not intentionally contaminated; instead, their already present Fe concentrations (lower than in the contaminated FZ wafers) were used. Multicrystalline Si is also known to contain other impurities (such as O, C, Cu, Ti etc…) and various crystal defects. In this experiment, multicrystalline silicon samples were chosen from the top and middle of one ingot (called material A and B, respectively). The distribution of impurities is not homogeneous along the ingot. The concentration of iron-boron pairs in the material A as-received is 6.5x10^{11} cm^{-3}, for

material B it is $3x10^{11}$ cm^{-3}. The concentration of carbon and oxygen are 3.5 (carbon at position B), 8.5 ppma (carbon at position A) and 2.6 ppma (oxygen at position B) versus 1 ppma (oxygen at position A), respectively.

These wafers were processed as described in Fig.1 and Fig.2. The experiments are divided in two parts. In the first part, the effect of hydrogen diffusion on the contaminated FZ and mc-Si was investigated. In the second part the effect of phosphorus diffusion on subsequent hydrogen passivation was inspected.

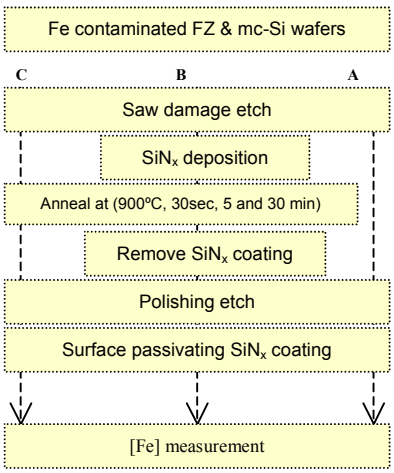

Fig.1: Schematic of processing group 1

Three different process schemes A-C sketched in Fig.1 were used to investigate the hydrogen passivation of Fe in the first group. Process A served to measure the as-cut minority carrier lifetime and the starting FeB concentration in the wafers. Group B served to monitor the effect of the hydrogen on the Fe in the materials. SiNx layers for bulk passivation were deposited by PECVD on both sides of wafers in group B. . Hydrogen diffusion into the wafers of group B was accomplished by a high-temperature (900°C) anneal step for different times. Group C served to monitor the effect of the anneal step, done without SiNx coating on wafers.

In the industry SiNx deposited on wafers serves as an ARC coating and as a source of hydrogen for passivation. The hydrogenation process step takes place during metallisation in a short time (about 20sec). Anneal at 900°C has the advantage that no iron precipitates form at this temperature [12].

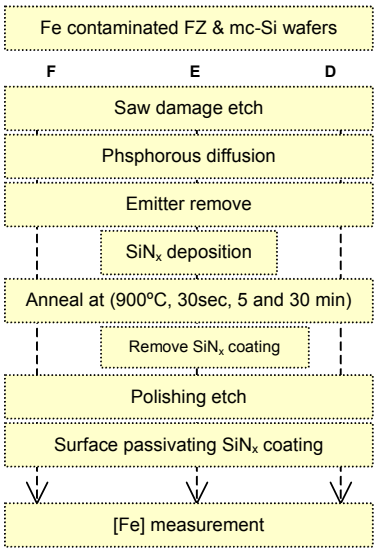

Fig.2: Schematic of processing group 2

In the second part of the experiment, neighbouring wafers are used to those used in the first part. Three different processing schemes D-F shown in Fig.2 were used to investigate hydrogen passivation of iron after phosphorous gettering. Group D served to monitor the effect of gettering on iron in the materials. Group E served to monitor the effect of hydrogen passivation of Fe after gettering, and the last group (F) monitored the effect of the anneal step without SiNx on the wafers.

After annealing steps, the wafers of all the groups were etched to remove 20µm from the surface, and a surface passivating SiNx was deposited by PECVD on both sides of the wafers. This allowed measurement of the bulk minority carrier lifetime.

3 RESULTS AND DISCUSSION

3.1 Contaminated FZ wafers

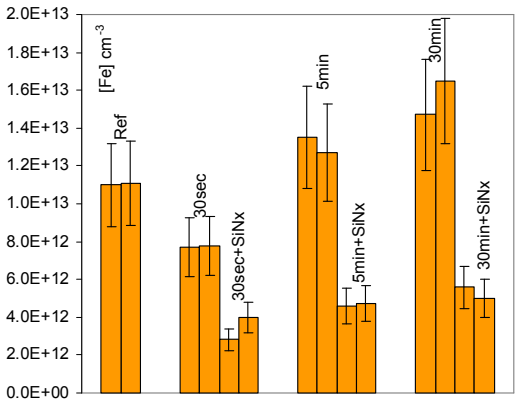

Fig.3: Iron concentration of contaminated FZ-wafers after different processing steps. The first two columns correspond to wafers annealed at 900°C without nitrides.

The contamination results in $1.2x10^{13}$ cm^{-3} iron. When the wafers were annealed for different durations without SiNx coating, the concentration of iron increases with anneal time. This may be due to the dissociation of iron-agglomerates, which are formed during the contamination. The results indicate that 30sec is not sufficient for dissociation of these agglomerates.

On the other hand, anneal of not-contaminated FZ wafers without SiNx coating in the furnace reduces slightly the minority carrier lifetime of these cotrol samples (data not shown). Analysis of the data show that the reduction of measured minority carrier lifetime is not due to the iron contamination, which means that the funace is clean enough.

However, when wafers are annealed with SiNx coatings on both sides, the concentration of measured iron decreased compared to those processed without SiNx layer. This decrease in iron concentration is surely due to hydrogenation and not to precipitation; otherwise iron would also be precipitated in the wafers that were annealed without SiNx coating. Note that for the wafers with SiNx, a slight increase in Fe concentration was observed for longer annealing times. However, taking into account the error bars no significant change is recorded. The error bars are based on an uncertainty in each lifetime measurement of 10%, mainly due to the systematic uncertainity of the equipment.

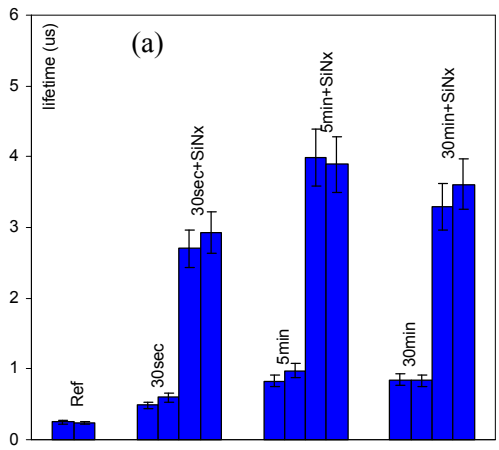

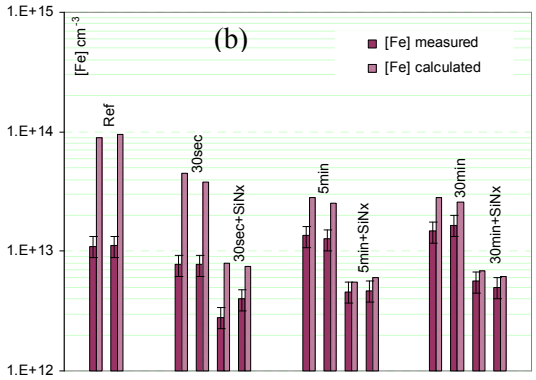

Fig.4: (a) Minority carrier lifetime of contaminated FZ wafers after different processing steps. (b) theoretical iron concentration which correspond to measured minority carrier lifetime.

The measured lifetime of 0.2µs corresponds theoretically to a concentration of iron equal to $8x10^{13}cm^{-3}$ while the experimentally determined iron concentration is equal to only $1x10^{13}cm^{-3}$ (Fig 4a). This observed difference may be caused by introduction of other types of contaminants or defects in the material during the intentional contamination with Fe. However, after hydrogenation the theoretically calculated iron concentration coincides perfectly with the measured values (Fig.4 (b)), meaning the wafers are then indeed dominated by Fe. This result can be interpreted as partial passivation of the iron and almost complete passivation of the other introduced defects. The calculation of lifetime based on iron concentration is described in detail in ref [10].

3.2 Multicrystalline wafers

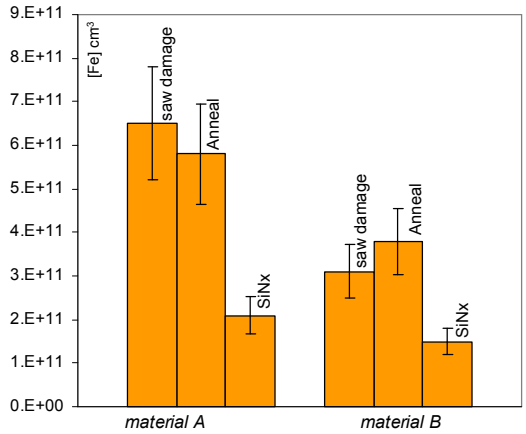

Fig.5: Iron concentration of mc-Si wafers after different processing steps (annealing at 900°C for 30sec).

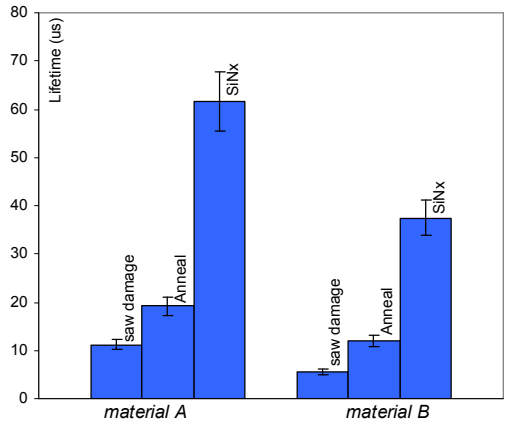

Fig.6: Minority carrier lifetime of mc wafers after different processing steps

Fig.5 shows the iron concentration in materials A and B after different processing steps. Annealing wafers with SiNx coating leads to the reduction of the measured iron concentration in both materials. After hydrogenation the minority carrier lifetime increases strongly (Fig.6) compared to the reference wafers. Similar to the situation for the FZ wafers, however, this increase of lifetime cannot necessarily be attributed to passivation of iron only because mc-Si wafers contain various defects and impurities.

3.3 Phosphorous-gettered multicrystalline wafers

Phosphorus gettering is known to remove metallic impurities from silicon materials. It has been used here to reduce the iron concentration in the neighbour wafers of those investigated in the first part of our experiment.

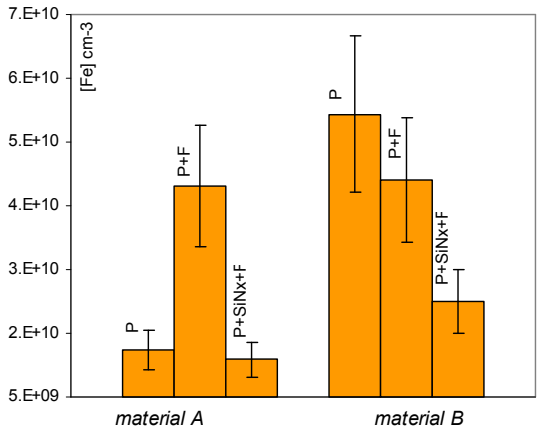

Fig.7: Iron concentration of mc-Si wafers after: (p): phosphorous gettering, (p+F): phosphorous gettering followed by anneal and (p+SiNx+F): phosphorous gettering followed by anneal with SiNx on wafers.

Fig.7 shows that due to gettering the iron concentration is dramatically reduced in both materials (from $6.5x10^{11}cm^{-3}$ to $1.6x10^{10}cm^{-3}$ and from $3.1x10^{11}cm^{-3}$ to $5.4x10^{10}cm^{-3}$ respectively for A and B). Annealing without nitrides leads to an increase in iron concentration, which is probably due to release of the iron from precipitates in the material A. But this is not the case for the material B. After hydrogenation, the iron concentration decreases further to its detection limit and the minority carrier lifetime increases (Fig.8).

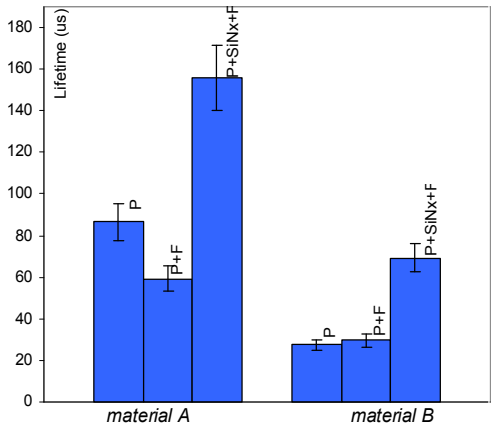

Fig.8. Minority carrier lifetime of mc-Si wafers -shown in Fig.7- after phosphorous gettering

3.4 Outlook

As a further step, the application of these techniques can lead to a clearer understanding of the hydrogen diffusion in silicon. The benefits of using this technique are the simplicity of both sample preparation and measurement of the iron concentration. Experiments have been started in this direction. Iron will be passivated by diffusion of hydrogen with varying parameters. Measurement of the iron concentration before and after removal of a surface layer will indicate to which depth is the hydrogen is diffused.

4 CONCLUSION

This investigation shows the capability of hydrogen passivation of iron in silicon and of detecting this by measuring the recombination-active FeB-concentration with the light-induced FeB-dissociation technique. Hydrogen passivation of intentionally contaminated Floatzone wafers with iron leads to a decrease of the FeB concentration with about a factor 3 (from $1.2x10^{13}$ cm^{-3} to about $4.5x10^{12}$ cm^{-3}). Multicrystalline silicon wafers without an intentional iron contamination show a similar decrease of the measured iron concentration after annealing with SiNx coating. Thus Fe can be a possible candidate to study hydrogen diffusion in silicon.

5 ACKNOWLEDGMENTS

This work has been carried out with financial support of NOVEM (The Netherlands Agency for Energy and the Environment) under contract numbers 2020.01.13.11.2002.

REFERENCES

[1] D. R. Campbell, M. H. Brodsky J. C.M. Hway, R. E. Robinson, and M. Albert, bull. Am. Phys. Soc. **24**, 435 (1979)

[2] C. H. Seager and D. S. Ginley Bull. Am. Phys. Soc. **24**, 401 (1979)

[3] C. H. Seager and D. S. Ginley Appl. Phys. Lett. **34**, 337 (1979).

[4] M. Stavola et al., 3rd World Conference on Photovoltaic Solar Energy Conversion, Osaka (2003).

[5] H. Dekkers et al., 3rd World Conference on Photovoltaic Solar Energy Conversion, Osaka (2003).

[6] L. J. Geerligs, A. Azzizi, D. Macdonald and, P. Manshanden 13th NREL workshop on crystalline silicon solar cell materials and process (2003)

[7] K. Graff and H. Pieper, J. Electrochm. Soc. **128**, 669 (1989).

[8] S. J. Pearton and A. J. Tavendale, J. Phys. C **17**, 9701 (1984).

[9] M. Kouketsu, S. Isomae, J. Appl. Phys. **80 (3)**, 1485 (1996).

[10] D. Macdonald, L. J. Geerligs, A. Azzizi, J. Appl. Phys. **95** (3), 1021 (2004).

[11] W. B. Henley and D. A. Ramappa J. Appl. Phys. **82 (2)**, 589 (1997).

[12] D. A. Ramappa and W. B. Henley J. Electrochm. Soc. 144, No 12,4353 (1997).

8. CASTING TECHNOLOGIES FOR SOLAR SILICON WAFERS: BLOCK CASTING AND RIBBON-GROWTH-ON SUBSTRATE

A. Schönecker[1], L. J. Geerligs[1] and A. Müller[2]

[1] ECN - Energy Research Center of the Netherlands, PO. Box 1, 1755 ZG Petten, The Netherlands.
schonecker@ecn.nl, geerligs@ecn.nl

[2] Deutsche Solar AG, Berthelsdorfer Str. 111a, 09599 Freiberg, Germany
armin.mueller@deutschesolar.de

Keywords: silicon wafer, photovoltaics, multi-crystalline, crystal growth

Abstract.
Multi-crystalline silicon solar wafer are the working horses of the rapidly developing photovoltaic market. The availability and cost efficiency but, even more important, the improved wafer quality and the understanding how to process multi-crystalline silicon wafers into highly efficient solar cells are important factors in this development. In this paper multi-crystalline silicon wafer manufacturing technologies both in industrial production as well as under development are outlined. Important wafer characteristics such as oxygen-, carbon and metallic impurities are described and experimental links to solar cell efficiency are exemplary demonstrated.

10th International Autumn meeting on Gettering and defect engineering in semiconductor industry. September 21-26, 2003. Berlin, Germany.
Solid State Phenomena Vols. 95-96 (2004), pp. 149-158

Introduction

In the last decade the photovoltaic solar energy market saw an explosive growth. Growth rates well above the long-term average of 15% could be realized and both politicians and PV module producers foresee growth scenarios in excess of 25% in the next years (up to 2010). These extra-ordinary growth rates are partially the result of governmental incentives such as the German 100.000 roof program, the Japanese 75.000 roof program and the one million-roof program in the US. Similar programs will most probably emerge in other countries of the European Union, to meet the ambitious target of the European Commission of 3 GWp PV installed in 2010.

The potential of Silicon wafer based solar cells is demonstrated by its still increasing market share of more than 90% (figure 1). Cost efficiency, stability and reliability of the silicon wafer based solar modules resulted in a superior market leadership of this technology. Nevertheless this also means that, in order for photovoltaics to become more cost efficient, the complete production chain from solar grade silicon to wafers, solar cells and modules has to be improved.

In the following we will focus on the possibilities and challenges of multi-crystalline silicon wafer manufacturing as one of the key technologies to lower PV module costs. Crystalline silicon wafers not only contribute to 35% - 45% of the total module manufacturing costs, but are also an important factor that determines solar cell respectively solar module efficiency. Thus both wafer manufacturing costs as also wafer quality are the drivers for further development of existing technologies and the benchmark for the introduction of new manufacturing methods.

Challenges in multi-crystalline silicon wafer manufacturing

The strong need in photovoltaics to minimize the manufacturing costs per solar electricity generation capacity (Wp), drives multi-crystalline silicon wafer manufacturers to improve the economical optimum between production efficiency and product quality. Although directionally solidified ingots [2] allowing for large area solar cell efficiency up to 18.3% [3] in a high-efficiency process are demonstrated, the commercially available wafers typically result in solar cell efficiencies around 15% in industrial solar cell processes.

The necessity to improve on wafer quality and manufacturing costs results in an ongoing effort to further develop production technology and machines as well as crystallization- and solar cell processes. With respect to crystallization- and solar cell process, the relation between silicon wafer material characteristics and solar cell efficiency is an area of ongoing research. Although the knowledge on silicon wafers developed by the semiconductor industry is inherited, the complex interaction between impurities, crystal structure and their behavior during the solar cell process as well as the large variation between solar cell processes makes it impossible to predict solar cell efficiencies from wafer parameters. This resulted in the situation that there is no generally accepted set of wafer parameters available that defines the quality of a silicon wafer

completely [4]. The suitability of a wafer for a solar cell process cannot be described but must empirically be tested in the cell process. With changes in either the material or the solar cell process these links have to be re-established.

Although the detailed mechanisms that control the relation between multi-crystalline silicon wafer characteristics and solar cell efficiency are very complex, there are guidelines for wafer quality with respect to oxygen, carbon, metallic impurities and crystal structures that can be used in the improvement of existing and the development of new silicon wafer materials.

In the following the development of multi-crystalline silicon wafer manufacturing technology will be outlined for two examples: the generic silicon block crystallization methods and the ribbon-growth-on-substrate (RGS) wafer casting as a promising representative of silicon ribbon manufacturing. Thereafter an overview on the relation between wafer characteristics and solar cell efficiency will be presented.

Block Casting Multi-Crystalline Silicon Wafer Manufacturing

Outline Technology. Historically, most of the multi-crystalline silicon wafers were and still are produced by crystallization of liquid silicon in the form of a block, which is then cut into wafers (see figure 2). Important milestones in the development of these technologies were the improved control of the planarity of the liquid-solid interface, which resulted in reduced stress of the silicon block. Also improvement of refractory material for the crucibles and the application of crucible coatings clearly enhanced wafer quality and reduced contamination from crucible walls.

As the crucible normally breaks during block cool down, increasing wafer production per crucible is of major importance. Separating melting from solidification units, as was applied in block-casting, improves the effective use of both melting crucible as well as solidification crucible (complete filling by liquid). The separation of these steps also allows enhanced control of melted silicon and solidification environment. Replenishment of the continuous melting unit could in principle enhance the cost effectiveness of block-casting even further.

Characteristics of block-cast multi-crystalline silicon wafers. Inherent to all forms of silicon block crystallization is the inhomogeneous distribution of the wafer characteristics due to the batch-wise process with changing process conditions. One of the major effects is the segregation of impurities due to the higher solubility of most materials in the liquid silicon phase. The positive effect is a cleaning of the silicon material by segregation of impurities into the top of the block. The disadvantage is the changing oxygen, carbon and doping concentration in the wafers, which depend on the height of the wafers in the block. Additional contamination from the crucible also results in different wafer characteristics in the areas of the wafer being in close

contact to the crucible walls (bottom, sides). This results in a location dependent behavior of the silicon wafers, which leads to a broadening of the solar cell efficiency distribution, e.g. a variation in short circuit current of 5-10% in dependence on the position of the wafer in a block [5].

Ribbon-Growth-on-Substrate (RGS) Multi-Crystalline Silicon Wafer Manufacturing

Outline Technology. The ribbon-growth on substrate (RGS) wafer casting technology is a silicon wafer manufacturing method, where liquid silicon is poured in a casting frame under which a colder substrate is moving, which causes the growth of a thin silicon layer (see principle of the RGS technology in figure 3). This technology was developed by Bayer AG [6] throughout the 80's and 90's and is now further developed by a Dutch consortium of ECN and S'Energy.
The challenges in the development of the RGS technology are the improvement of the material quality in order to become a cost competitive material and the realization of a reliable production machine.

Characteristics of RGS multi-crystalline silicon wafers. From a principle point of view one of the major advantages of the RGS technology is that it is a continuously operating process opposite to the batch-wise block-casting. This should result in homogeneous wafer properties. The challenges for the RGS material are the speed of the process (1 wafer/second) resulting in rapid thermal profiles and fast crystal growth (typically 300 μm/s) [7] and the close contact of the liquid and solid silicon to refractory materials (melting crucible, casting frame and substrates). Therefore improvements in process control and materials are very important for RGS wafer manufacturing and the main reason for the progress in material quality and related to it solar cell efficiency.
Record solar cell efficiencies achieved with RGS wafer-based solar cells show a remarkable trend over the last 10 years, which was the result of a good co-operation between wafer manufacturer (Bayer AG), solar cell process developers as well as basic silicon material research and development (HEXSi, KoSi, RGSells projects). This led to an increased understanding of the material characteristic and the behavior of the RGS wafer in a solar cell process. The consequences of this development can be seen by the steady efficiency increase as shown in figure 4. Latest record solar cell efficiency reached at the University of Konstanz are 12.8% [11].
In the future, it is expected that this development can be continued at the same or even increased speed. In order to do so, the next step was to reduce the high oxygen content of the wafers. This limits at the moment the hydrogen diffusion from a SiN coating and thus the efficiency of an

RGS solar cell in an industrial-type cell process. Further efficiency influencing factors are the formation of oxygen related recombination centers (thermal and new donors) [8,9,10]. In the past RGS wafers with high oxygen content were annealed in order to form larger oxygen precipitates and to avoid the formation of oxygen related donor complexes in the solar cell process. Recent machine improvements resulted in a low oxygen concentration RGS wafer (5×10^{17} cm^{-3}), which made it possible to reach high open-circuit voltages in a solar cell process without pre-annealing [11].

RGS prototype machine development. One of the major challenges of the RGS technology is the development of a new RGS wafer-manufacturing machine. The design is based upon the following ideas:

- The machine should translate the batch-wise process into a continuous operation.
- The machine should maintain operation even in the case of processing problems of limited duration. For this purpose, silicon melt control, replacement of substrates on the fly and many other safety mechanisms will be included.
- In contrast to silicon ingot growth or CZ crystal pulling, RGS wafer production involves mechanical movement with high precision at high temperatures. The design was made in a way that the mechanical movement is not in contradiction with the demand of minimum contamination of the hot silicon by particles from metallic parts of the machine.

Although silicon crystal pulling machines are state-of-the-art technology in the semiconductor and solar industry, the intended RGS machine will push the limits. The continuous silicon melt rate will be a factor 2 higher than the melting rate achieved during CZ-growth melt replenishment. Substrate materials have to be developed and optimized that can withstand the repetitive contact with liquid silicon and the temperature cycles in the machine for a long time. Mechanical and thermal stress of the wafers and machine parts has to be minimized during operation at high speed under large temperature variations.

All these conditions combined with the experience of the consortium led to a machine design (cross section see figure 5), which will be realized in the near future.

Multi-Crystalline Silicon Wafer Characteristics and Solar Cell Efficiency

In the following, wafer characteristics for multi-crystalline silicon wafers are shown and their relation with minority carrier lifetime respectively solar cell efficiency is outlined. The most important wafer characteristics are oxygen and carbon content, metallic impurities (e.g. iron) and crystal imperfections, dislocations and grain boundaries.

Oxygen and Carbon. The solubility limits from literature for oxygen and carbon in crystalline silicon at the melting point are $2.6\cdot10^{18}$ cm^{-3} (52 ppma) and $3.5\cdot10^{17}$ cm^{-3} (7 ppma), respectively

[13]. While the concentration of oxygen can usually be kept far below its limit in cast material, the concentration of substitutional carbon is often found to be much higher. This is attributed to strain release in the presence of interaction with oxygen [14], but also lattice defects and non-equilibrium effects during crystallisation may be expected to have an effect.

Shown in figure 6 are typical concentration profiles of oxygen and carbon found in a variety of multi-crystalline ingots, produced by casting, Bridgman, and HEM techniques.

In general cast ingots can have lower oxygen concentrations than Bridgman or HEM ingots, due to different gas ambient and better silicon volume to crucible surface ratio. However, it was also found that block casting material shows higher oxygen concentrations than HEM and Bridgman at the bottom of the ingot and reaches lower values in the middle and top part (figure 6). It is likely that the coating of the quartz crucible plays an important role in preventing quartz dissolution into the silicon. Damage of the coating (e.g., by sharp edges of the feedstock chunks) can therefore strongly affect the oxygen concentration.

While in experiments on the materials of figure 6, carbon concentrations as high as 18 ppma were not found to be noticeably detrimental to minority carrier lifetime or solar cell efficiency, the high oxygen concentrations are clearly disadvantageous. This could be due to precipitation of oxygen, possibly together with other (metallic) contaminants or, the formation of new or thermal donors during heat treatments, which can all lead to recombination-active defects. It was found that hydrogen-passivation has a stronger beneficial effect on these oxygen-related defects than elsewhere in the ingots [5,15].

Recently, a class of shunts in multi-crystalline silicon solar cells has been related to transmission electron microscopy images of carbon precipitates [16]. It is not published, however, under which conditions and at which carbon concentrations in the silicon, these precipitates developed.

For silicon wafers of lower initial quality, such as silicon films or ribbons, hydrogen passivation of defects during solar cell processing plays an important role in reaching competitive efficiencies. Both theoretical models [9] as well as experimental evidence [8] showed a relation between oxygen content and hydrogen diffusion speed and passivation potential. It was found that hydrogen in low oxygen EFG was diffusing much faster than in high oxygen RGS material.

At extremely high oxygen contents, such as in earlier RGS material, the formation of new donors during normal solar cell process steps and the low hydrogen diffusivity limited the solar cell efficiency. In order reduce the concentration of recombination active oxygen related defects, RGS material was therefore often annealed at high temperatures in order to form extended oxygen precipitates, which do not dissolve in a solar cell process. Recent changes in the RGS process reduced the oxygen content to values between 5×10^{17} cm^{-3} and 1×10^{18} cm^{-3}. This allowed the use of RGS wafers in a standard solar cell process without oxygen precipitation annealing.

Metallic impurities. Metallic impurities are always present in cast silicon material. They originate from contaminants in the feedstock and in the quartz crucible and its coating. Present-day ingots are partly produced from very clean ("semi-prime") silicon, produced specifically in reactors which are also used for electronic grade silicon production. This presently accounts for more than 50% of the feedstock for cast silicon. If handled properly, this material is very clean and hardly adds impurities to the silicon melt. The other part of feedstock used today consists of rejected and recycled silicon from the microelectronics industry, such as tops and tails from Czochralsky ingots and pot-scrap. These will contain higher levels of impurities. The most important source of contaminated feedstock is however, likely, the edges of ingots which are cut-off before wafering and recycled as feedstock for subsequent ingots. These have been contaminated by impurities diffusing from the quartz crucible and its coating into the silicon ingot during cool-down.

One of the most important recombination centers in cast material is the FeB pair, which develops from pairing of interstitial Fe impurities with a B dopant atom. FeB concentrations can be conveniently derived from carrier lifetime measurements before and after optically induced FeB pair dissociation. This is described in detail in ref [17].

Figure 7 shows FeB concentrations measured for a number of ingots. Figure 8 shows a detail for the bottom 100 mm of one particular ingot. An increased FeB concentration is found in the bottom and side edges of ingots. This Fe clearly has diffused in after solidification of the ingot [18]. Its source must be the crucible or crucible coating. This FeB is responsible for a very significant lifetime degradation: For example, a concentration of $2 \cdot 10^{12}$ cm^{-3} FeB pairs will reduce the lifetime to 10 μs (at an non-equilibrium carrier density of 10^{15} cm^{-3}).

Figure 9 shows the minority carrier lifetime and FeB profiles of one particular column. It is remarkable how well the lifetime follows the (inverse) trend of the FeB. There are potentially other impurities present in the crucible or coating material. However, these will generally have diffusivities very different from Fe, and will therefore diffuse to a different depth than the Fe during the cool-down of the ingot. The fact that the lifetime profile corresponds well with the FeB profile is an indication that Fe is the major detrimental impurity in ingots, when they are grown from high-purity feedstock. Indeed, below it will also be shown that when theoretically subtracting the effect of FeB, generally a high to very high lifetime results.

Because the impurities are concentrated in the liquid silicon as solidification progresses, the concentration of FeB increases towards the top of the ingot. The concentrated impurities precipitate in the final stage of solidification, in the very top of the ingot. During the cool-down, the impurities can diffuse back from this precipitated layer into the ingot. This is responsible for the peak in FeB contamination in the top of the ingots in Figure 7.

Dislocations in multi-crystalline silicon wafers. As a rule of thumb it is generally thought that dislocation densities below 105 cm-2 are acceptable for solar cells. This is supported by results from experiments done on float-zone silicon wafers with varying dislocation densities. Below a dislocation density of 10^5 cm^{-2}, minority carrier lifetime was high and dislocation density independent. Between 10^5 cm^{-2} and 10^6 cm^{-2} there is a transition region, while above a dislocation density of 10^6 cm^{-2} minority carrier lifetime drops rapidly [19,20].
In block-cast multi-crystalline material dislocation density is typically in the range of or below 10^5 cm^{-2}. However areas with low minority carrier lifetimes and very high dislocation densities are also found. These areas normally occur in neighboring wafers at identical locations, which results in the picture that they grow with the solid liquid interface vertically through the silicon block. As these areas are thought to be the quality-limiting factor for good multi-crystalline material, generation of highly dislocation rich areas and the further growth throughout the ingot are of major interest [21].
Dislocations also play an important role for RGS wafers. At the moment the general model is that dislocations in RGS wafers are generated by thermal or mechanical stress during the crystallization phase and the initial wafer cool-down. Dislocation densities between 10^5 cm^{-2} and 10^8 cm^{-2} are found in RGS wafers. Recent experiments indicates that it might be possible to control dislocation densities at an acceptable level, however more statistical evidence and analysis is needed.

Grain size and grain boundary recombination. During the development of the multi-crystalline silicon wafer technology, modelling work was done with respect to solar cell efficiency and grain size. In [22] grain boundaries were described by a barrier height and a space charge region around the grains. Depending on the parameters, grain boundaries are more or less recombination active, and also change their behaviour with injection level (typically recombination velocity decreases with increasing injection). The problem however is that there is insufficient knowledge about the grain boundaries in existing materials to describe real material completely with theoretical models. In directionally solidified and block-cast multi-crystalline silicon wafers typical grain sizes are large enough that grain boundary recombination is of no significant influence on solar cell efficiency. However, with the development of high-speed wafer production such as the ribbon-growth-on-substrate method or Astropower's Silicon Film, grain sizes become smaller and grain boundary recombination might become the ultimate efficiency limit to these technologies.

Summary

As was demonstrated, there is a strong ongoing drive to improve crystalline silicon wafer manufacturing technologies with respect to manufacturing costs and quality. With respect to

manufacturing costs, reducing the silicon loss, wear part costs and machine throughput are the main challenges. With respect to material quality, an improved understanding of the relation between wafer parameters and solar cell efficiency allows to optimize the combination of wafer and solar cell process with respect to cost per Wp.

With respect to the development of sawing based multi-crystalline silicon wafer manufacturing technology, the development from Bridgman technology, via the planarization of the solidification front to the separation of melting and crystallization process in the block casting machine demonstrates the development from a relatively low throughput, static process environment to a flexible, high throughput wafer manufacturing technology. By enlarging melting- and solidification volumes there is a large potential for material improvements and cost reduction.

From this point a logical step in the direction of the optimum silicon wafer manufacturing technology would be to avoid any silicon material losses by the direct production of silicon wafers, without compromising high machine throughput, flexible process control and wafer quality. Ribbon-growth-on-substrate silicon wafer casting has the potential for all these characteristics, however machine and material development have to prove that the promises can be realized in relation to the moving target of directionally solidified and cut wafer technology.

Acknowledgements

The authors would like to thank the silicon team at Access e.V. for their innovative work on solar silicon crystallization modeling and material characterization. The RGS and the multi-crystalline silicon processing team at ECN and the University of Konstanz for many experiments, discussions and a continuous stream of new and exciting research results.

The work on the RGS technology is supported by the Dutch E.E.T. program in the RGSolar project under contract EETK99150 and the European Commission in the RGSells project under ENK6-CT2001-00574. The multi-crystalline silicon work at ECN is supported by Novem under contract number 146.110-020.1 and 2020.01.13.11.2002.

References

[1] P. D. Maycock, The World Photovoltaic Market, June 15, 2002, http://www.pvenergy.com

[2] S. Nara, Y. Sakaguchi, 12th Workshop on Crystalline Silicon Solar Cell Materials and Processes, NREL/BK-520-32717, p. 28, 2002

[3] Y. Komatsu, Y. Takaba, S. Yasukawa, S. Okamoto, M. Shimizu, 12th Workshop on Crystalline Silicon Solar Cell Materials and Processes, NREL/BK-520-32717, p. 87, 2002

[4] SEMI M6-1000, Specification for Silicon Wafers for Use as Photovoltaic Solar Cells, Semiconductor Equipment and Materials International, www.semi.org

[5] L. J. Geerligs, 12th NREL workshop on silicon solar cell materials, NREL/BK-520-32717, p. 288, 2002

[6] W. Koch et al., Proceedings 2nd World PVSEC, 1998, p. 1254

[7] A. Schönecker, L. Laas, A. Gutjahr, M. Goris, P. Wyers, G. Hahn, D. Sontag, 12th NREL workshop on silicon solar cell materials, NREL/BK-520-32717, p. 7, 2002

[8] T. Pernau, et al., Proc. 17th European PVSEC, Munich 2001, p. 1764

[9] B. Sopori, et al., Journal of Electronic Materials, Vol. 30, No 12, 2001, p. 1616

[10] A. Kananmori, M. Kanamori, Journal Applied Physics, 50, 1979, p. 8095

[11] G. Hahn, S. Seren, D. Sontag, A. Gutjahr, L. Laas, A. Schönecker, "Over 10% efficient screen printed RGS solar cells", to be published in the proceedings 3rd WCPEC, Osaka, 2003

[12] Giso Hahn, private communications

[13] Properties of Crystalline Silicon, ed. R. Hull (Inspec, London, 1999).

[14] H. J. Möller, Semiconductors for solar cells (Artech, Norwood, 1993).

[15] L. J. Geerligs, "Impact of defect distribution and impurities on multi-crystalline silicon cell efficiency", to be published in the proceedings of the 3rd WCPEC3, Osaka, 2003

[16] O. Breitenstein et al., "Shunt types in multi-crystalline solar cells", ", to be published in the proceedings of the 3rd WCPEC3, Osaka, 2003

[17] D. Macdonald and A. Cuevas, Proceedings of the 11th workshop on crystalline silicon solar cell materials and processes, (NREL, 2002) p. 24

[18] M. Acciarri et al., 13th European PVSEC, p. 1336, 1995

[19] T. F. Ciszek, T. H. Wang, Proceedings Electrochemical Society Fall Conference, Phoenix, 2000, NREL/CP-520-28569

[20] D. Cavalcoli, A. Cavallani, E. Gombia, M. Reiche, Solid State Phenomena Vol. 32, p319, 1993

[21] Dieter Franke, PhD thesis, Shaker Verlag, ISBN 3-8265-8585-2

[22] Dugas et al., Rev. Phys. Appl. 22, p. 677-685, 1987

Figure captions.

Figure 1: World photovoltaic module shipments per technology. [1]

Figure 2: The principles of Bridgman, Heat Exchange Method (HEM) and Block-Casting as technologies to solidify a multi-crystalline silicon block.

Figure 3: Principle of the RGS ribbon growth process. The relatively cold substrate extracts the crystallization heat from the liquid silicon in the casting frame. This causes the growth of a silicon ribbon in contact with the substrate. By transporting the substrate from the casting zone into the cooling down section, crystal growth is stopped and the silicon ribbon can be removed.

Figure 4: Record RGS solar cell efficiencies. Earliest results were from Telefunken and its successor ASE. In later projects the Fraunhofer Institute for Solar Energy Systems (FhG-ISE) and the University of Konstanz (UKN) held the efficiency records. [12].

Figure 5: Cross section from the design of the continuously operating RGS machine. In the lower part of the vacuum vessel the mechanical drive is enclosed, while in the upper section the furnace and casting sections are situated. Wafer stacker and wafer load lock is shown on the right. The diameter of the machine will be about 3.5 m.

Figure 6: Measurements by Fourier Transform Infrared Spectroscopy of dissolved carbon and oxygen (substitutional and interstitial, respectively) in a range of multi-crystalline silicon ingots. The source of carbon in ingots is both carbon present as contaminant in the feedstock as well as carbon monoxide from the furnace environment, which dissolves into the liquid silicon. Probably the latter is by far the most important. The source of oxygen contamination is mostly dissolution of the quartz crucible into the silicon melt, which mainly influences silicon material at the bottom of the ingot.

Figure 7: FeB concentration in dependence of the wafer position in multi-crystalline silicon ingots.

Figure 8: FeB and oxygen concentrations together with Short circuit current value variation of solar cells processed with and without hydrogen passivation from a SiN coating are presented in relation to FeB and oxygen concentration. The wafers are from the bottom of an ingot with high oxygen concentration.

Figure 9 Typical minority carrier lifetime and FeB concentration correlation in a multi-crystalline silicon block.

Figure 10: RGS crystal structure (left). Average grain size is about 150 μm. The right picture shows the RGS crystal structure after a defect-etch.

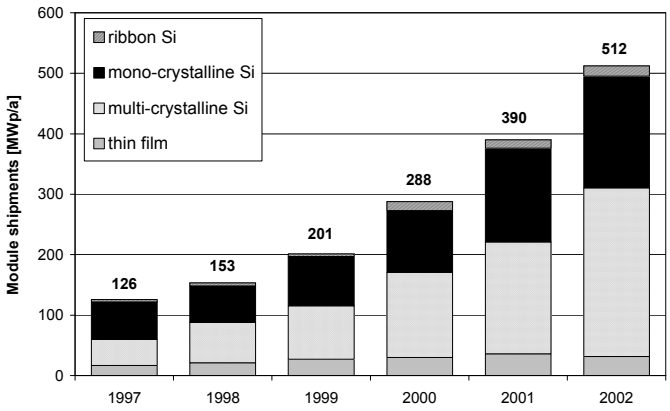

Figure 1

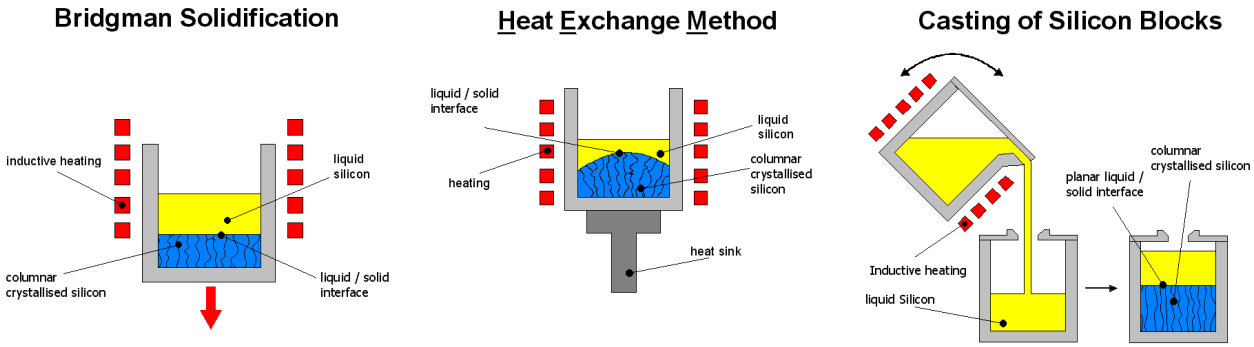

Figure 2

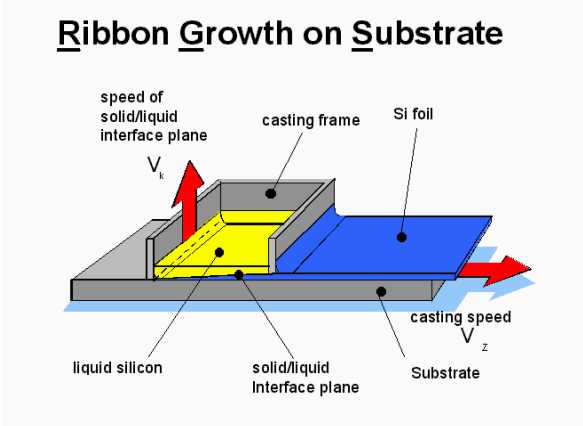

Figure 3

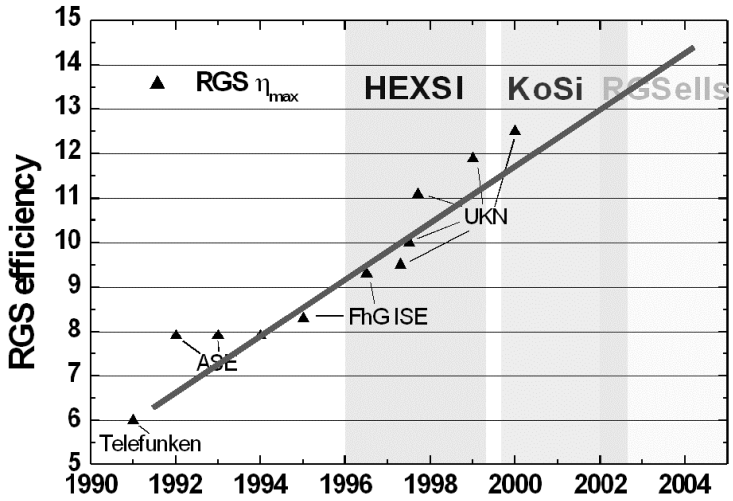

Figure 4

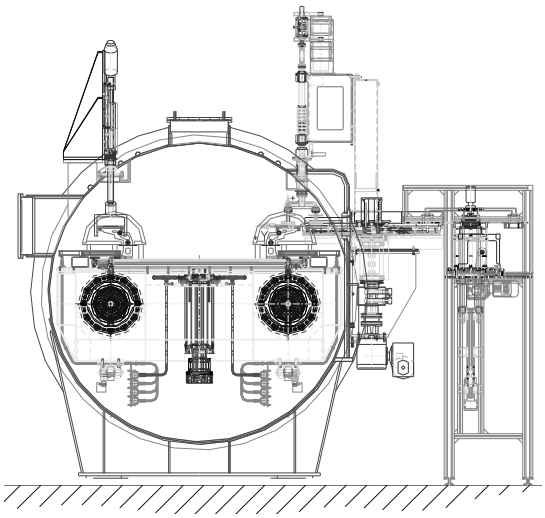

Figure 5

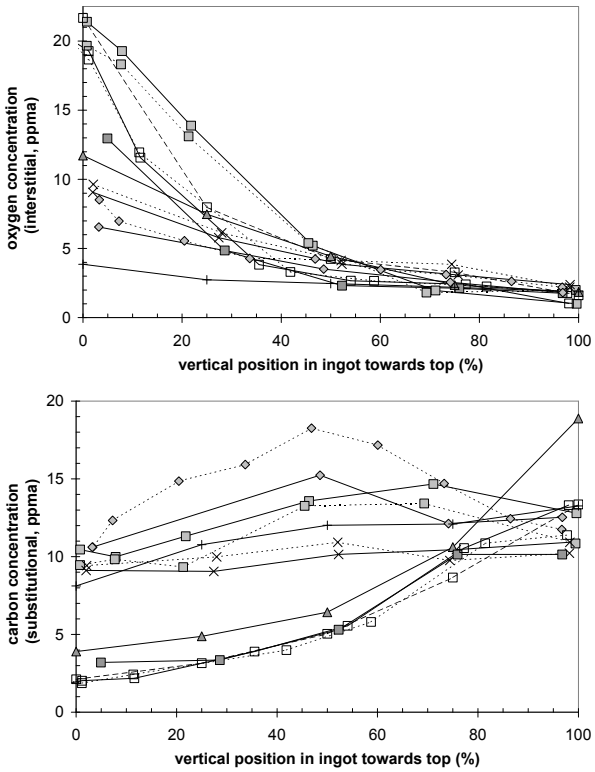

Figure 6

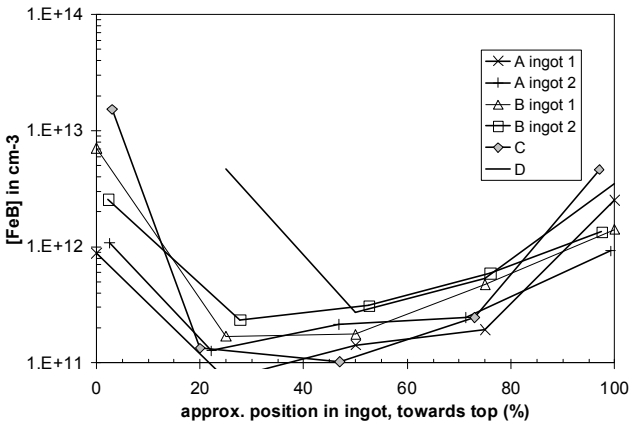

Figure 7

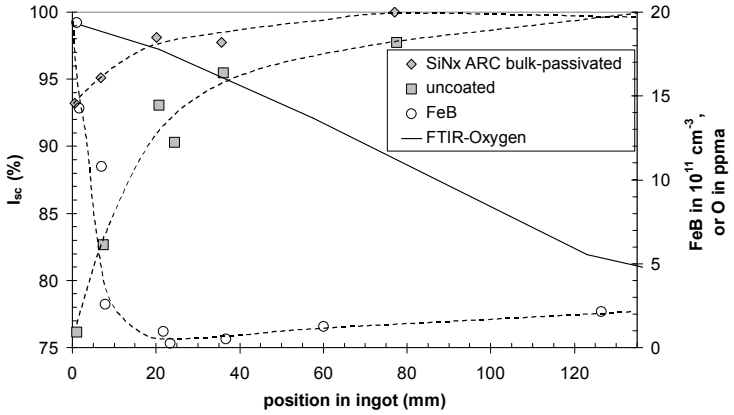

Figure 8

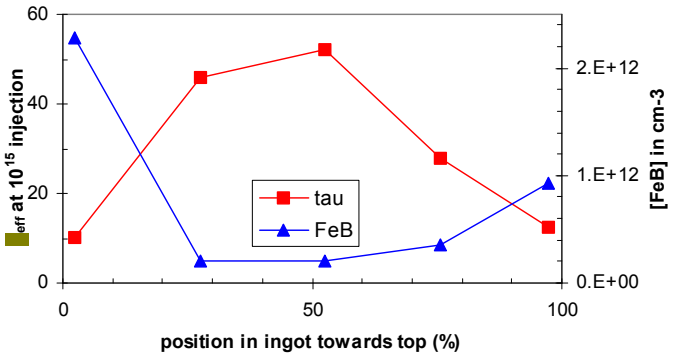

Figure 9

Figure 10

9. CHARACTERISATION OF MULTI-CRYSTALLINE BLOCKS AND EFFORTS TO RELATE THEIR PROPERTIES TO THE EFFICIENCIES OF SOLAR CELLS

L. J. Geerligs

ECN Solar Energy, PO Box 1, NL-1755 ZG Petten, The Netherlands

Abstract

We present characterisation results of current standard quality multicrystalline ingots, with the objective to relate the material quality to the solar cell performance. Interstitial iron (Fe_i) and oxygen concentrations and crystallographic defect density are among the most useful parameters. The use and interpretation of measurements of interstitial iron content in multicrystalline silicon is discussed in some detail. Fe_i is generally the most important impurity and lifetime measurements become more predictive and applicable when quantitatively separating the lifetime due to Fe_i from lifetime due to other defects. In addition, because of its convenient measurement, Fe_i is a convenient probe to evaluate and model the effect of high-temperature steps.

14th Workshop on Crystalline Silicon Solar Cell Materials and Processes. August 8th-11th, 2003. Winter Park, Colorado, USA. Published by NREL, Golden, Co.

Introduction

The properties of solar cells produced from multicrystalline silicon (mc-Si) wafers show a significant variation. It is useful to understand the part of this variation which is due to material properties, and to see whether the understanding can be generic, independent of manufacturer. In this paper we will look at current standard quality ingot-grown mc-Si. A characterization of commonly used mc-Si can help to put studies which focus on special material with for example high concentrations of a particular kind of defect into context.

Multicrystalline silicon (mc-Si) for solar cells is commonly grown in large rectangular ingots, which are solidified from bottom to top. These ingots are cut into vertical ‘bricks’ or 'columns' of square cross-section, which are subsequently cut into wafers. The material parameters of the ingots vary from bottom to top, as well as laterally, depending on equipment, materials and procedures used by the manufacturers.

It has been a long-standing goal to develop a quick screening of as-grown material which predicts the solar cell properties. As a rudimentary screening, manufacturers measure the lifetime on blocks, before wafering, to determine which part of the block can be sold as wafers, and which part should be recycled or discarded.

Measuring some more parameters can improve the usefulness of this screening. Only using the lifetime criterium may in fact result in discarding more material than necessary. Hence, a better understanding of the relation between material parameters and cell performance is valuable in several respects:
- By determining more exactly which material will result in acceptable cells, the yield from mc-Si ingot growth may be increased.
- It will be clearer which growth parameters form a bottleneck for cell performance and need to be improved (e.g., feedstock purity, or cool down rate).
- If it is clear which material parameters are responsible for cell degradation, and how these material parameters vary through an ingot, it should be possible to adapt process parameters in a production line to the part of an ingot that is momentarily processed.

Parameters which turn out to be useful are:
- the concentration of dissolved iron (Fe_i)
- the concentration of dissolved oxygen (O_i)

- the defect and lifetime distribution (i.e., the distribution of low defect, high lifetime areas versus high defect, low lifetime areas over the wafer).

In this paper, all three parameters are found to be necessary to qualitatively explain the response of wafers to cell processing and the resulting cell efficiencies. The defect/lifetime distribution seems to be the main parameter for the variation of cell efficiency within most of the ingot volume (in some cases excluding some of the edge regions). The quantitative prediction of variation of cell efficiency between ingots will probably depend on microscopic parameters, such as decoration of dislocations, or presence of impurities other than Fe, additional to the three parameters listed above (Fe, O, defect distribution).

This paper is largely based on earlier papers[1,2], together with some related recent results. Of course there exists a large literature on the subject of the relation between impurities, defects, and cell performance. It is hoped that this paper provides a useful sketch of some main features of this relation, and of the use of, in particular, Fei measurements in its analysis.

Experimental

The results reviewed here concern standard wafers of about 300 micron thickness, from regular commercial ingots, from different manufacturers. Results are presented from wafers which are normally sold. That excludes material of the edges of the ingots which is normally discarded, and which is about 20-30 mm thick. If in a figure the coordinate 'position in ingot' is given, it thus refers to this part of the ingot, excluding the edges.

For FTIR measurements the wafers were chemically polished and FTIR spectra were compared to a floatzone reference.[3] For lifetime measurements the wafers were chemically polished and coated with a SiNx layer with deposition parameters optimised for surface passivation. Surface recombination velocities tested on floatzone wafers were below 100 cm/s. Lifetimes were measured with Sinton WCT-100 (spatially averaged, quasi-steady-state photoconductance - QSSPC) or spatially resolved by MFCA (modulated free carrier absorption)[4].

Fei concentrations were derived from Sinton measurements before and after optically induced FeB pair dissocation, as discussed later.

Solar cells were processed with a conservative industrial cell process: 45 Ω/sq emitter and screen printed aluminum rear side metallisation. Cells were mostly not anti-reflection coated, to facilitate their comparison.

Oxygen contamination of mc-Si

It is well known that the oxygen concentration decreases slowly from bottom to top of an ingot. In most of the ingots the oxygen is everywhere below 10 ppma, and in most of the material even below 5 ppma. Figure 1 shows that some ingots (type A in this paper) have much higher maximum oxygen concentrations of around 20 ppma in the bottom.

In literature,[5] it has been noted that there exists a threshold of 12-14 ppma for precipitation of oxygen during high-temperature steps. From cell results later in this paper, it appears that indeed a major effect of oxygen occurs only when the concentration is higher than this threshold.

Another detrimental effect of oxygen is the carrier-induced formation of boron-oxygen defects. This varies more gradually with oxygen concentration. While there is still uncertainty about the physical nature of the defect, its effects have been quite well documented.[6,7] For an oxygen concentration of 10 ppma, and a boron dopant density of 10^{16} cm^{-3}, it imposes a cap of approx. 50 μs on the lifetime.

Fe contamination of mc-Si

It is a convenient coincidence that interstitial iron (Fe_i) in silicon is a major impurity (probably the most important bulk point defect for recombination) in mc-Si, and that at the same time it can be measured very sensitively using lifetime measurements. The measurement is by FeB pair dissociation; it utilizes the fact that the iron content of a boron-doped p-type Si wafer can be deliberately cycled between being mostly present as Fe_i or as pairs with substitutional boron: $(Fe_i)^+(B_s)^-$ pairs. At room temperature in thermal equilibrium virtually all Fe_i is present as FeB pairs. FeB pair dissociation can be accomplished by illumination at room temperature,[8] by minority carrier injection,[9] or by increasing temperature which shifts the equilibrium state of Fe_i and B to isolated ions.[10] The isolated and paired form of interstitial iron have markedly different recombination properties.[11,12] This leads to significant changes in carrier lifetime and diffusion length after dissociating the FeB pairs. Assuming that all other recombination processes remain unchanged, the FeB concentration can be found by measuring the carrier lifetime before (τ_0) and

after (τ_1) pair dissociation: $[FeB]=C(\tau_1^{-1}-\tau_0^{-1})$. The use of the known recombination parameters of both FeB pairs and Fe_i provides the pre-factor C.[11,12,13]

Calculating FeB concentrations from geometrically averaged lifetimes (such as determined with the Sinton WCT-100) can result in an overestimate. This happens when the lifetime measurement averages over areas of low and high lifetime, with the same concentration of FeB. Typical errors are estimated to be up to a factor 2. Details will be given in ref.[14]

Figure 2 shows FeB concentrations measured for a number of ingots. Figure 3 shows a detail for the bottom 100 mm of one particular ingot. The *central parts* (20-80% of ingot height) of the ingots show qualitatively different properties than the *edges*. This is due to different mechanisms for the incorporation of Fe_i.

1) In the central parts, take-up is from contamination in the liquid silicon during solidification. This is governed by the process of segregation: only a small fraction ($\sim 10^{-4}$) of the concentration in the liquid state is incorporated as Fe_i in the solid state. Because the impurities are concentrated in the liquid silicon as solidification progresses, the concentration of Fe_i increases towards the top of the ingot. Most of the concentrated impurities precipitate in the final stage of solidification, in the very top of the ingot.

The amount of Fe_i in the central part of the ingots is about $1\text{-}3\cdot10^{11}$ cm^{-3}, or about 0.05 ppba. The equilibrium segregation coefficient of Fe between solid and liquid silicon is just below 10^{-5}, and would apply for infinitely slow ingot growth The real segregation coefficient is probably higher by approx. a factor 10, i.e. around 10^{-4}.[15] This indicates that the typical contamination of the melt with iron is of order 0.5 ppma.

2) In the edges, most Fei originates from solid-state diffusion *after* solidification.[16] This gives rise to the increased FeB concentration; between 10^{12} and 10^{13} cm^{-3} at approx. 2-3 cm distance from the edges. For bottom and side edges, the source must be the crucible or crucible coating. In the top edge, the impurities have diffused back into the ingot from the precipitated layer of the final stage of solidification.

The source of iron may in fact be partly the same in both cases: The Fe diffusing from crucible/coating into the solidified ingot will also dissolve into the liquid silicon before

solidification. Together with Fe impurities already present in the silicon feedstock, this gives rise to at least part of the Fei in the central parts of the ingots.

Figure 4 shows the lifetime and FeB profiles of one particular column. It is remarkable how well the lifetime follows the (inverse) trend of the FeB. There are potentially other impurities present in the crucible or coating material. However, these will generally have diffusivities very different from Fe, and will therefore diffuse to a different depth than the Fe during the cool-down of the ingot. The fact that the lifetime profile corresponds well with the FeB profile is an indication that Fe is the major detrimental impurity, at least in this ingot. Indeed, below it will also be shown that when theoretically subtracting the effect of FeB, generally a high to very high lifetime results.

Rinio *et al.* have recently analysed the edge zone of ingots with LBIC and micro X-ray fluorescence.[17] They could clearly detect precipitated Fe up to approx. 20 mm from the edge of the crucible, i.e. up to the edge of the 'commercial' regions as in Figure 2. They observed a 'denuded zone' of approx. 650 micron around grain boundaries. Thus it is likely that part of the solid-state diffused Fe_i with concentration $>10^{13}$ cm^{-3} precipitates during cool-down of the ingot.

The total concentration of Fe found in mc-Si material is generally much higher than the $\sim 10^{11}$-10^{12} cm^{-3} found as interstitial Fe.[18] Recently, Macdonald *et al.* have compared the measurements by FeB pair dissociation with measurements of total concentration by Neutron Activation Analysis (NAA).[19] Results from this work are reproduced in Figure 5. It is striking that Fe_i as well as total Fe both show the same segregation profile in agreement with the Scheil equation[20]:

$$C_s = kC_o(1-f_s)^{k-1},$$

but different by several orders of magnitude. Here k is the segregation coefficient, C_s is the concentration in the solid state, C_o is the starting concentration in the liquid, and f_s is the fraction solidified. (On plots such as Figure 5 it is impossible to distinguish between different k if their value is <0.1.) It is possible that the two concentration profiles in Figure 5 were mostly created already during crystallisation: segregation to crystal defects and segregation to bulk Si in crystals may have very different coefficients.[21] This would imply that the Fe_i curve in Figure 5 is not a remnant of diffusion and precipitation of most of the Fe_i during ingot cool-down.

The relationship between dissolved Fe_i and Fe-precipitates, i.e., the processes of crystallisation, segregation, precipitation and dissolution of precipitates, are a subject of current research. For this paper it is probably most important to note that Fe_i has much more impact on lifetime measurements (in particular on averaged lifetime measurements such as QSSPC) than the rest of the Fe. At the same time, gettering under the right conditions can reduce the Fe_i concentration significantly. Therefore, a lifetime measurement before gettering with the aim to characterise material with respect to cell properties should try to separate the contribution from Fe_i.

If the lifetime only due to Fe_i (paired to FeB in thermal equilibirium) is denoted by τ_{FeB} and the lifetime due to all other recombination channels is denoted by τ_{other} , then the measured lifetime τ_{eff} is related to both as

$$1/\tau_{other} = 1/\tau_{eff} - 1/\tau_{FeB} \quad (1)$$

τ_{other} can likely be better used as predictive parameter for cell efficiency than τ_{eff}. Because of the effective gettering of Fe_i, τ_{other} is more closely related to the lifetime after gettering than τ_{eff}.

Figure 6 shows τ_{other} and τ_{eff} for ingot B2. τ_{other} is quite high (up to >100 μs), also in the edges where τ_{eff} is suppressed by Fe_i. In the next section we will show that this is predictive for good cell results, also in the edges. For some other ingots we have found that τ_{other} at the edges is quite reduced. Also in such a case, τ_{other} is in fact a good predictive parameter. This may be because it is reduced due to a high density of precipitates which make gettering problematic (although not impossible [22,17]).

Neither the Fe_i concentration nor τ_{other} are necessarily stable under thermal treatments. A typical belt furnace anneal during diffusion is at ~900 ºC, and cool-down is much more rapid than the original ingot cool-down. Such an anneal may therefore release impurities from precipitates. Figure 7 shows the effect of an anneal at ~900 ºC and rapid cool in a belt furnace. It shows only a limited increase of [FeB] and τ_{other}^{-1}. This probably originates from precipitates. With a phosphorous gettering layer present, the Fe_i concentration drops significantly in the edges, resulting in similar values as in the center of the bricks. Gettering keeps τ_{other}^{-1} rather constant.

τ_{other} and cell efficiency

From the previous it is clear that τ_{other} can be interpreted as a 'potential lifetime' which can be obtained after gettering. Fe_i diffuses fast at phosphorous diffusion temperatures and can be removed quite well by gettering. A limitation to gettering due to the ratio of solubilities in phosphorous-rich layer and in the silicon, is discussed in refs.[23,24]

In Figure 8 we compare cell results to lifetime. Focus is on I_{sc} because V_{oc} is affected noticably by the background doping of the wafer. This doping varies quite strongly within an ingot (up to a factor 2), and between manufacturers (also of the order of a factor 2).

Figure 8 shows for three ingots (from different manufacturers) the τ_{eff} and τ_{other} of as-cut wafers, and I_{sc} of cells. The qualitative correspondence between τ_{other} and I_{sc} is good. Quantitative comparison is limited already a priori by the different areas used for the lifetime measurement (~2 cm diameter) compared to the the cell (100 cm^2), in combination with the inhomogeneous lifetime distribution in multicrystalline wafers. For quantitative comparison a spatially resolved τ_{other} would have to be converted to overall cell response.[25]

In our experience, Figure 8(b) is encountered most often. Figure 8(a) which is related to a high oxygen concentration in the bottom occurs much less frequently. Figure 8(c) is also less frequent. Figure 8(c) shows a low τ_{other} in the bottom and top edges of an ingot. This may be due to materials or thermal parameters used for the ingot growth. Adjusted gettering procedures for this ingot improved the cell results from the edge wafers significantly.[22]

We do not discuss hydrogenation in detail here. The Fe_i concentration is already low after gettering. Recent results show that it may be further reduced due to hydrogenation.[26]

τ_{other} and crystalline quality

A major factor giving rise to the variation of τ_{other} and cell results from wafer to wafer is the distribution of the crystal defect density. Figure 12 shows the close correlation which exists between density of crystal defects (mostly dislocation tangles) and the lifetime histograms. Histograms of such maps show large qualitative differences between ingots. Figure 9 illustrates the wide varieties of lifetime distributions which can be found in ingots. They correspond to the cell variations in Figure 8. In ingot a) cell performance improves from bottom to top, whereas in

ingot b) it is the reverse. Ingot c) resulted in the best cells (excluding the contaminated edge wafers).

The trend we encounter most often in commercial ingots is that defects increase towards the top of the ingot, and lifetime and cell properties therefore decrease.

Oxygen

The ingot of Figure 8a) has a, not very common, high oxygen concentration in the bottom. As mentioned before it is known that oxygen can precipitate into recombination active defects above a threshold of 12-14 ppma. Ingots with oxygen concentration below that level and a high τ_{other} show no particularly deviating cell properties for bottom wafers. Wafers with oxygen above that level, such as in Figure 8a) and Figure 10, show a large reduction of cell efficiency, and τ_{other} strongly decreases after a gettering or anneal step.

Figure 10 FeB, oxygen, and cell Isc from the bottom of an ingot with high O concentration.

In the bottom wafers from Figure 10, after anneal without a phosphorous source, FeB hardly decreased. After emitter diffusion, however, the FeB was strongly reduced. The lifetime nevertheless decreased, suggesting that the anneal enhanced precipitation. It is possible that the Fe and O co-precipitate into an iron silicate.[27]

The harmful effects of the oxygen-related precipitates can be removed to a large extent by hydrogen passivation, as Figure 10 shows.

The impact of the boron-oxygen defect, or CID (carrier-induced degradation) on industrial mc-Si solar cells has been modeled in ref.[7]. Results are reproduced in Figure 11. There is a slight impact of oxygen even below 10 ppma.

Summary

In conclusion, lifetime and FeB measurements on a number of mc-Si ingots have been reported which show that FeB drastically influences the carrier lifetime of the wafers, without being indicative for the solar cell properties expected after standard industrial processing. The as-cut lifetime after correction for the presence of FeB, τ_{other}, is a useful indication for cell results, in particular for variation of cell properties through an ingot. Yield of ingots may improve when these considerations are taken into acount when deciding which edge parts are to be discarded.

The variation of τ_{other} generally follows the distribution of crystal defects. Quality of ingots and homogeneity of cell results therefore depend on the control over the creation of crystal defects during growth. The exact variation of cell properties will probably also depend on microscopic material parameters which were not included in this paper, such as presence of impurities other than Fe_i.

Generally, τ_{other} decreases slightly after thermal treatment. It could therefore be a useful parameter to follow thermally induced material changes (such as precipitation and dissolution), other than those involving Fei only. Changes in Fe_i can be very well monitored by FeB pair dissociation measurements.

The presence of a high concentration of oxygen, above 10-15 ppma (which is not very common), is clearly detrimental to cell properties, in particular in combination with iron.

Acknowledgments

We are grateful to A. Kinomura, Y. Nakano, D. Macdonald, and A. Cuevas for the NAA characterisation results of ref.[19] We acknowledge the manufacturers of mc-Si wafers which supplied test material. We acknowledge valuable discussions with Daniel Macdonald, Giso Hahn, Gaute Stokkan, Erik Sauar, Tonio Buonassisi and the group members of ECN-solar.This work has been supported by NOVEM (The Netherlands Agency for Energy and the Environment).

References

[1] L.J. Geerligs, 12th NREL workshop on crystalline Si solar cells and materials, p. 288 (2002).

[2] L.J. Geerligs, 3rd WCPEC, Osaka, p. 1044 (2003).

[3] The calibration constant used for conversion of absorbance to concentration was the ASTM-1995 standard: 6.28 ppma-cm for oxygen (at ~1107 cm-1). The effective thicknesses of the floatzone reference wafer and the test wafers were matched using the Si phonon bands similar to the discussion in K. Krishnan et al., *Characterization of Semiconductor Silicon using FTIR*, in: *practical Fourier Transform Infrared Spectroscopy*, eds. J.R. Ferraro, K. Krishnan (Academic Press, 1990) p. 313.

[4] methodology as in A. Schönecker et al., J. Appl. Phys. **79**, 1497 (1996).

[5] J.W. Mayer and S.S. Lau, *Electronic Materials Science* (Macmillan, 1988), p. 176. The rate of precipitate nucleation is a high power of the oxygen concentration, see *Handbook of Semiconductor silicon technology*, eds. O'Mara, Herring, and Hunt (Noyes publications, 1990). A threshold of around 14 ppma for the detrimental effects of oxygen was reported by. S. Martinuzzi et al., 13th EC-PVSEC, p. 1382 (1995).

[6] J. Schmidt *et al*, 26th IEEE PVSC, Anaheim (1997); K. Bothe *et al*, 3rd WCPEC, Osaka, p. 1077 (2003); S. Rein *et al*, 3rd WCPEC, Osaka, p. 1048; p. 1057 (2003).; H. Nagel *et al*, 14th EC-PVSEC, 762-765 (1997); M. Dhamrin *et al*, 29th IEEE PVSC, New Orleans, 2002.

[7] D. Macdonald *et al*., 13th NREL workshop on crystalline Si solar cells and materials, p. 182 (2003), focuses on evaluation of the effect in mc-Si.

[8] K. Graff and H. Pieper, J. Electrochem. Soc. 128, 669 (1981); L.J. Geerligs and Daniel Macdonald, *Dynamics of light-induced FeB pair dissociation in crystalline silicon*, submitted to Appl.Phys.Lett.

[9] L.C. Kimerling and J.L. Benton, Physica 116B, 297 (1983); L.C. Kimerling, Proc. of the MRS Annual Meeting, 1980, Boston, MA (North-Holland), p. 85.

[10] G. Zoth and W. Bergholz, J. Appl. Phys. 67, 6764 (1990).

[11] D. Macdonald, A. Cuevas, J. Wong-Leung, J. Appl. Phys. 89, 7932 (2001).

[12] A.A. Istratov, H. Hieslmair, and E.R. Weber, Appl. Phys. A: Mater.Sci.Process. 69, 13 (1999).

[13] D.H. Macdonald, L.J. Geerligs, and A. Azzizi, J. Appl. Phys. 95, 1021 (2004).

[14] D. Macdonald and L.J. Geerligs, to be published.

[15] L.J. Geerligs et al., Proceedings of the 12th workshop on crystalline silicon solar cell materials and processes, (NREL, 2003) p. 216.

[16] M. Acciarri et al., 13th EC-PVSEC, 1336 (1995).

[17] M. Rinio, C. Ballif, T. Buonassisi, and D. Borchert, *Defects in the deteriorated border layer of block-cast multicrystalline silicon ingots.* To be published in the proceedings of the 19th EC-PVSEC, June 2004, Paris.

[18] D. Macdonald, A. Cuevas, A. Kinomura, and Y. Nakano, 29th IEEE PVSC, New Orleans, (2002); A. A. Istratov et al,. J. Appl. Phys. 94, (2003), 6552.

[19] D. Macdonald, A. Kinomura, Y. Nakano, L. J. Geerligs and A. Cuevas, *Interstitial and Precipitated Iron Content of a Photovoltaic-Grade Cast Multicrystalline Silicon Ingot*, submitted to 4th International Symposium on Advanced Science and Technology of Silicon Materials, Nov. 22-26, 2004, Kona, Hawaii; and to be published.

[20] see e.g. Schei, Tuset, and Tveit: *High Silicon Alloys* (TAPIR Forlag, Trondheim, 1998).

[21] T. Buonassisi, private communiation; A. A. Istratov, W. Huber, and E. R. Weber, *Experimental evidence for the presence of segregation and relaxation gettering of iron in polysilicon layers*, submitted to Appl. Phys. Lett.; T.

Buonassisi *et al*., *Synchrotron-based investigations of the nature and impact of iron contamination in multicrystalline silicon solar cell materials*, submitted to J. Appl. Phys.

[22] P. Manshanden et al., to be published.

[23] C. Ballif et al., *17th European PVSEC*, 1818 (2001).

[24] L. Caballero *et al*., 3rd WCPEC, Osaka, p. 1013 (2003).

[25] for relation of lifetime distribution to cell results, see, e.g., W. Warta et al., 2nd World Conference on PVSEC, 1650 (1998); B.L. Sopori, Mater. Sci. Forum **258-263**, 527 (1997); J. Isenberg et al., 29th IEEE PVSC, (2002), R.A Sinton, 3rd WCPEC, Osaka, p. 1028 (2003); S. Riepe *et al*., *Increased wafer yield for solar cells in top and bottom regions of cast multicrystalline silicon*, 18th European PVSEC (Paris, 2004); and references therein.

[26] A. Azzizi, et al., *Hydrogen passivation of iron in crystalline silicon*, to be published in the proceedings of the 18th EC-PVSEC (Paris, 2004).

[27] S. McHugo et al., Physica B **273-274**, 371 (1999).

Figure captions

Figure 1 Typical oxygen concentrations in multicrystalline Si ingots

Figure 2 FeB in mc-Si ingots.

Figure 3. Detailed FeB measurements in the bottom of ingot A2.

Figure 4 Typical lifetime and FeB correlation in a multicrystalline Si block (ingot B2).

Figure 5. Measurements of total and interstitial Fe concentration in a mc-Si ingot. From ref.19 Solid lines are conform the Scheil equation with $k<0.1$.

Figure 6. Effective lifetime and carrier lifetime calculated in the absence of FeB, τ_{other}, for two bricks from ingot B2.

Figure 7. Change of FeB and of $1/\tau_{other}$ in material of Figure 6 (ingot B2). Top: after anneal at ~900 ºC and rapid cool. Bottom: after gettering.

Figure 8. τ_{eff} measured, τ_{other}, calculated with eq. 1, and I_{sc} of cells. Ingots from three different manufacturers; (a) ingot A2 with high oxygen concentration in the bottom, (b) ingot B2 with low oxygen concentration ingot C with low oxygen but also low τother in the edges.(ingots A2 and B2 processed without ARC, ingot C processed with ARC, separately).

Figure 9 Histograms of lifetime maps (0 - 120 μs) for "as-cut" wafers from the ingots of Figure 8. Left to right plots correspond to wafers from a height of 25%, 50%, and 75% in the ingots.

Figure 11. Modelled V_{OC} as a function of $[O_i]$ for standard SiN coated industrial mc-Si cells with modified-Gaussian lifetime distributions. From ref.[7]

Figure 12. Photographs after defect etch and corresponding MFCA lifetime maps of the three samples of Figure 8-b and Figure 9-b. X and Y dimensions are in mm. The MFCA grey scale is 0-130 μs (linear).

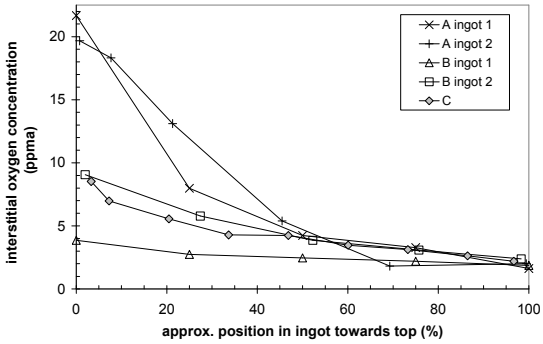

Figure 1

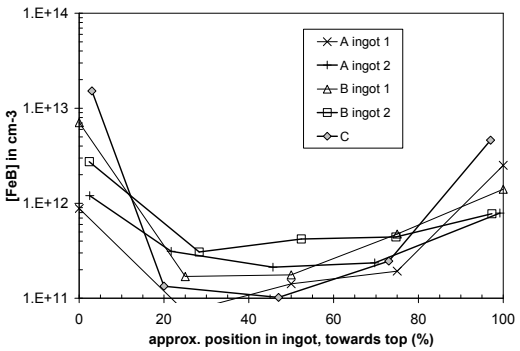

Figure 2

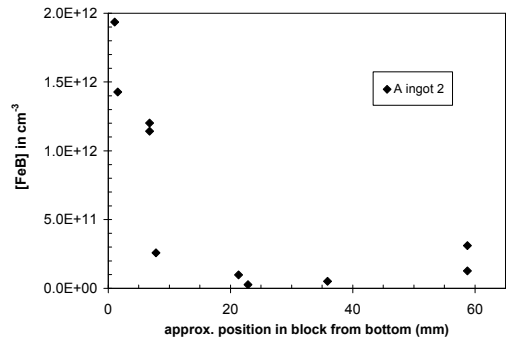

Figure 3

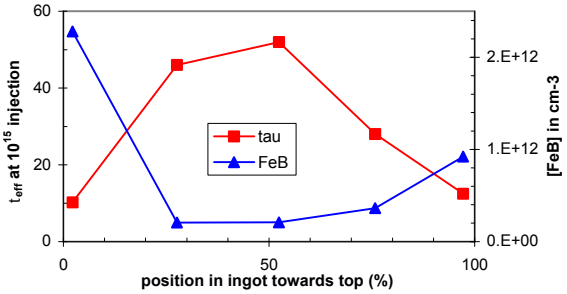

Figure 4

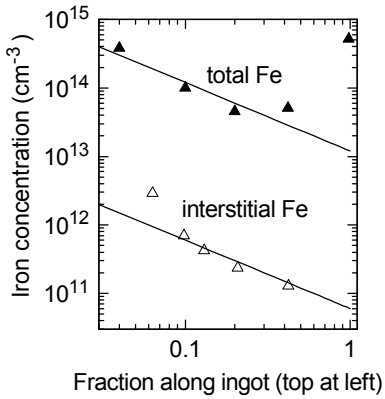

Figure 5

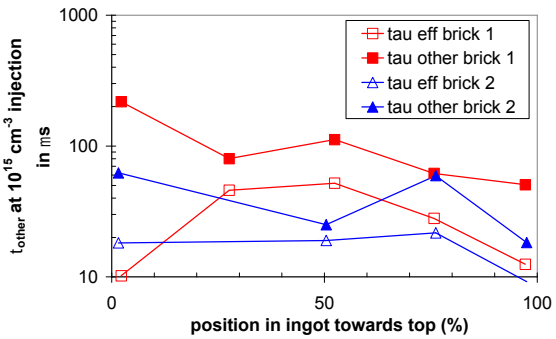

Figure 6

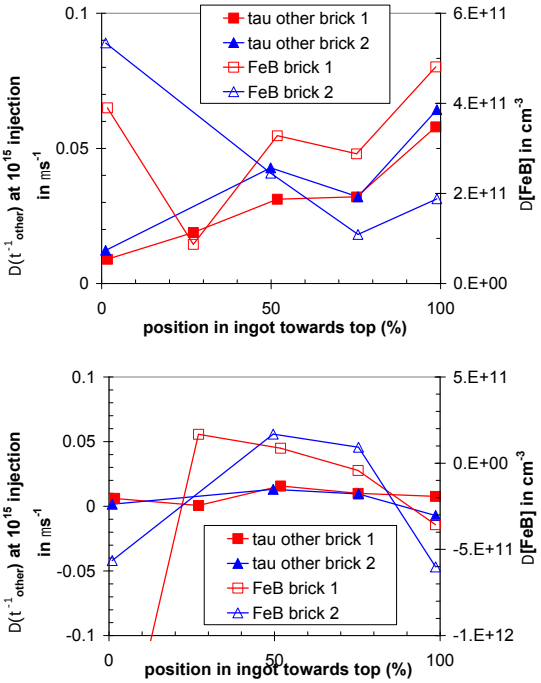
tau other brick 1
tau other brick 2
FeB brick 1
FeB brick 2
0.1
0.05
0
6.E+11
4.E+11
2.E+11
0.E+00
0
50
100
position in ingot towards top (%)
D(t-1 other) at 10-15 injection in ms-1
D[FeB] in cm-3
5.E+11
0.E+00
-5.E+11
-1.E+12
-0.1
-0.05

Figure 7

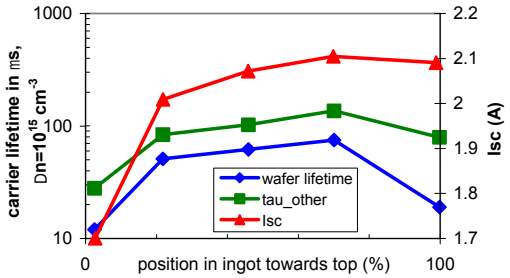
1000
100
10
2.2
2.1
2
1.9
1.8
1.7
carrier lifetime in ms,
Dn=10^15 cm^-3
Isc (A)
wafer lifetime
tau_other
Isc
0
position in ingot towards top (%)
100

a)

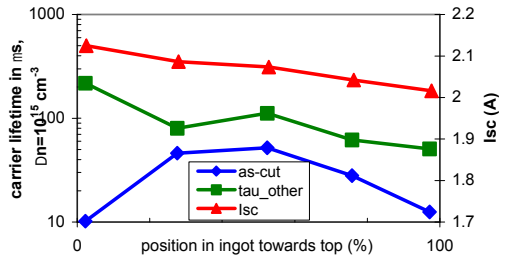
1000
100
10
2.2
2.1
2
1.9
1.8
1.7
carrier lifetime in ms,
Dn=10^15 cm^-3
Isc (A)
as-cut
tau_other
Isc
0
position in ingot towards top (%)
100

b)

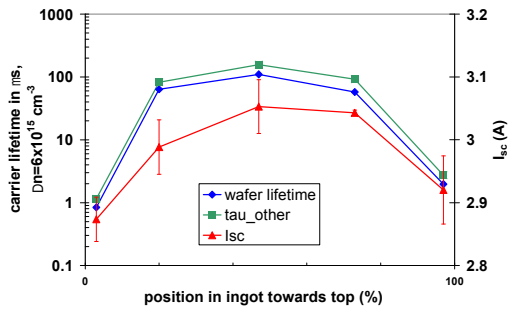
1000
100
10
1
0.1
3.2
3.1
3
2.9
2.8
carrier lifetime in ms,
Dn=6x10^15 cm^-3
Isc (A)
wafer lifetime
tau_other
Isc
0
100
position in ingot towards top (%)

c)

Figure 8

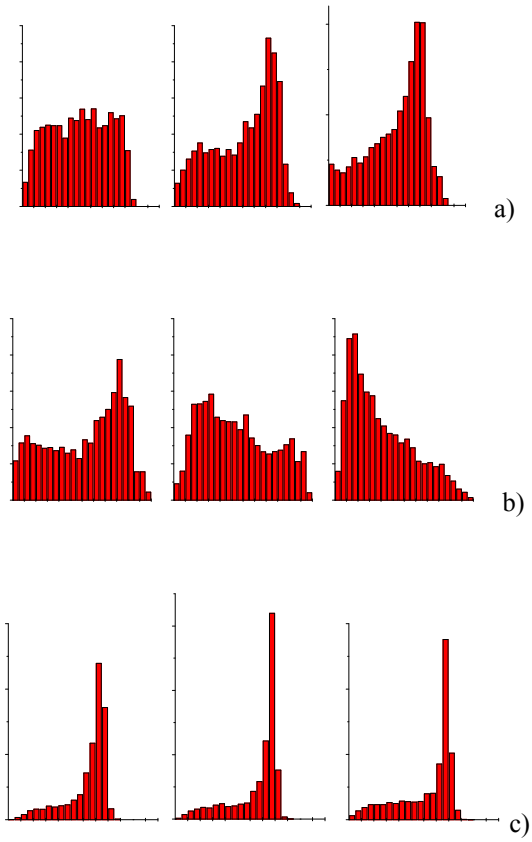

Figure 9

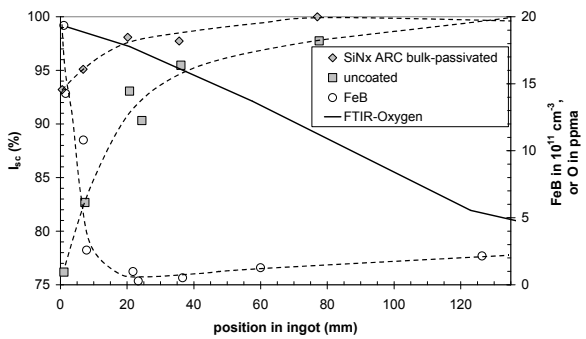

Figure 10

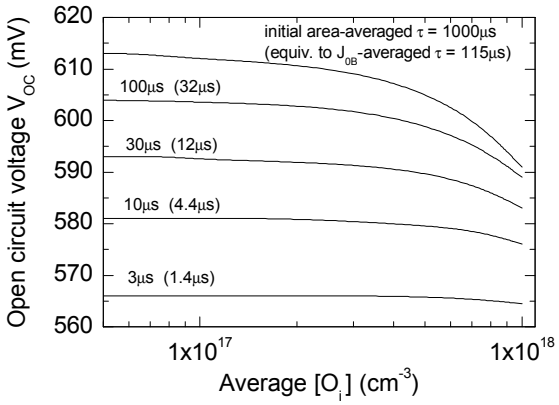

Figure 11

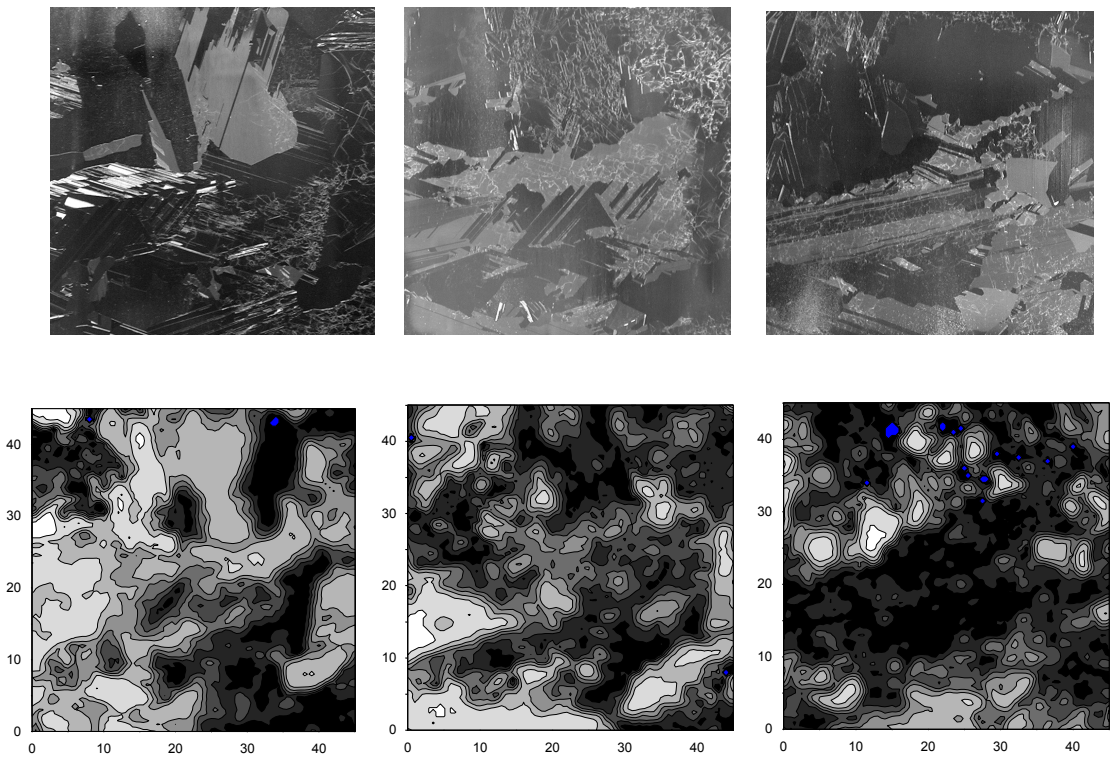

Figure 12

10. EFFECTIVE AND PRACTICAL PHOSPHOROUS GETTERING OF MULTICRYSTALLINE SILICON

P. Manshanden and L.J. Geerligs

Energy research Centre of the Netherlands ECN, Solar Energy, PO Box 1, NL-1755 ZG Petten, The Netherlands

Tel. +31 224 564765 Fax +31 224 568214

Email: manshanden@ecn.nl

Abstract

The gettering during an emitter diffusion in multicrystalline silicon is improved by adding a low-temperature tail to the standard diffusion. The tail preserves the emitter sheet resistance. An increase in minority carrier lifetime of up to a factor ten is obtained. Recombination activity of grain boundaries as well as concentration of interstitial iron decrease, accounting at least partly for this improved lifetime. Two mechanisms which may be responsible for the improvements are discussed: beneficial changes in thermodynamics and kinetics of the gettering because of the low temperature, and reduction of size and concentration of precipitates because of the longer duration.

Keywords

iron, silicon, minority carrier lifetime

1 Introduction

The majority of solar cells are made from crystalline silicon. More than half of the crystalline silicon solar cell production is based on multicrystalline silicon. Multicrystalline silicon (mc-Si) incorporates many impurities and defects that limit the minority carrier lifetime and thus the solar cell performance.[1] The quality of mc-Si wafers may become worse in the future, for several reasons. First, lower-quality feedstock will probably have to be used, for cost reduction and availability reasons.[2] Second, faster crystallisation, increased recycling of contaminated silicon, lower-cost and lower-quality furnace materials, and ribbon growth techniques may be used which result in more contamination of the wafers. Third, to increase the yield of wafers from an ingot, wafers may be cut closer to the contaminated edge zones of ingots. Therefore, there is a growing need for techniques to improve the quality of mc-Si wafers, i.e., to increase the minority carrier lifetime, during the cell process. The carrier lifetime should preferably be increased by adaptation of existing cell process steps, which in addition should not alter any other process characteristics such as sheet resistance or contact resistance. In this paper, we will investigate the increase of carrier lifetime by an extended phosphorous gettering, an adaptation of the existing emitter diffusion.

There exists an extensive literature on phosphorous gettering. The concept of variable temperature gettering was proposed by Plekhanov et al.[3] It aims to enhance the removal of impurities which are trapped at crystal defects, e.g., in precipitates. Dissolution of such impurities into the silicon matrix may at low temperature be kinetically limited, due to e.g. volume mismatches[4], and/or thermodynamically limited, due to maximum solubility. In variable temperature gettering a high temperature part of the gettering is therefore proposed to provide sufficient thermal energy to free impurities from their trapped state. A subsequent lower temperature gettering is then used to getter the impurities into the phosphorous-rich layer (PRL) at the surface. This lower temperature is necessary because segregation to the PRL is temperature-dependent. The solubility of impurities in the gettering layer divided by the solubility in the silicon lattice is the segregation coefficient for the gettering process.[3,5,6] For phosphorous gettering (as well as for Al gettering) this segregation coefficient decreases with increasing temperature, i.e., the solubility in the Si increases faster than in the gettering layer.

Variable temperature gettering was tested experimentally by Macdonald et al. with a high temperature of 1200˚C followed by a ramp down in steps of 100 ºC,[7] following the temperature profile proposed by Plekhanov et al, but using plateaus of constant temperature between the steps. The process has not been described more specifically. This did not result in improvement compared to the as-received wafers, perhaps because the low-temperature part was not long enough to getter all released impurities, or the final temperature was too high. However, Harkönen et al.[8] successfully increased the minority carrier lifetime of multi-crystalline samples by a phosphorous diffusion at 870˚C followed by gettering at 700˚C for 840 minutes. In contrast to the profile proposed by Plekhanov et al. and used by Macdonald et al., the temperature profile of Härkönen et al. can be used for emitter diffusion. Because the second temperature is much lower than the diffusion temperature it does not decrease the sheet resistance of the resulting emitter. The average lifetime increase, compared to standard gettering, found by Harkönen et al. was approximately 35%. The results were obtained on low-quality wafers of two ingots: one that met the (lifetime) requirements of the manufacturer and one that did not meet those requirements. It was not investigated whether the lifetime improvement was due to depletion of precipitates (the principle of variable temperature gettering), the improved segregation (the effect of the lower temperature), a combination of both, or another effect.

Other existing literature, in particular by Ballif et al. also notes the temperature-dependence of gettering results. Ballif et al. showed that even when using a constant gettering temperature, gettering already improves for lower temperature. This was demonstrated both in lifetime and in the resulting concentration of interstitial iron impurities. The result was attributed to the improved segregation coefficient at low temperature. Similar results were obtained by Rinio et al.[9] and Caballero et al[6].

In this paper, we will investigate the effect of an extended diffusion similar to Harkönen et al, but for more practical (shorter) durations. We investigate standard commercial multicrystalline wafers. The results are analysed on the basis of minority carrier lifetime measurements (averaged and spatially resolved), and changes in interstitial iron concentration. We observe improvements in average lifetime of up to a factor ten. The temperature dependence of the segregation ratio appears not to be the main or only

reason for the benefit of the low-temperature tail. Rather, the balance between release of impurities (from e.g. precipitates) and gettering could be a major reason.

2 Experiment

Multicrystalline wafers of 300 μm thickness were selected from two different manufacturers (ingot A and B). Wafers were selected from two different positions in the ingots, see *table 1*. The first position is near the bottom edge (A5 and B10, approx. 5 and 10% from the bottom edge, respectively). At that position both precipitated and dissolved impurities are present at a high concentration, probably due to solid state diffusion from the nearby crucible. The other position is more towards the middle of the ingot where impurity concentration is significantly lower (A15 and B50, approx. 15 and 50% from the bottom edge, respectively). The character (size, composition, location) of the precipitates may be different between bottom and central location but only preliminary results on this are available in literature.[10]

Sets of sister wafers were used to compare the gettering profiles. Sister wafers are wafers which were vertically adjacent to each other in the ingot. Therefore, differences between sister wafers after different processing can be interpreted as being due to variations in the process parameters, rather than due to material variations. Wafers were divided in quarters to enhance statistics. Floatzone control wafers were processed together with the multicrystalline wafers to check for any contamination that occurs during processing.

The processing schemes are indicated in *figure 1*. The as-cut wafers were etched in an alkaline solution until the saw damage was removed. A phosphorous dopant was spun on both sides, and the organic solvents were evaporated. Different temperature-profiles were applied for gettering (*fig 2*). A standard gettering/diffusion at a high temperature for a limited duration was used as a reference. The improved extended gettering/diffusion profile consisted of a normal period at standard emitter diffusion temperature followed by a longer period at a lower temperature (the 'low-temperature tail'). All wafers had a target sheet resistance of 48 Ohm/sq. The thermal profile was applied in a rapid thermal process (RTP) furnace under dry air atmosphere, for all samples except the ones with shortest low temperature

tail. The latter were diffused using a belt furnace. This belt furnace can extend a gettering/diffusion step only by a limited time, using the minimum belt speed. As will be shown in the results section, the type of furnace has little influence on the resulting lifetime changes. The phosphorous glass was removed in HF, and the emitter was measured with a four-point probe. Then 10 μm from each side of the wafer was removed with a chemical etch. This removed the emitter as well. The wafers were then surface passivated with silicon nitride[11]. This silicon nitride has no bulk passivating properties at the deposition temperature. This surface passivating SiNx layer has a surface recombination velocity of <100 cm/s. Therefore the reported effective lifetime approximates the bulk minority carrier lifetime closely, except for the wafers with very high lifetimes.

The minority carrier lifetime of the samples was analysed with the quasi steady state photoconductance technique (QSSPC).[12] The sample is illuminated with infrared light. The resulting change in photoconductance is measured with an inductively coupled coil, providing a minority carrier lifetime which is a geometrical average over the coil area.

Iron is a major impurity in multicrystalline silicon, probably the most important bulk point defect for recombination[13,14]. It is present both as precipitates and as interstitially dissolved point defects (Fe_i)[15]. The concentration of Fe_i can be determined very sensitively using the QSSPC lifetime measurements. The measurement is by FeB pair dissociation; it utilizes the fact that the interstitial iron in a boron-doped p-type Si wafer can be deliberately cycled between being mostly present as isolated Fe_i^+ or as pairs with substitutional boron: $(Fe_i)^+(B_s)^-$ pairs. At room temperature in thermal equilibrium virtually all Fe_i is present as FeB pairs. [16] FeB pair dissociation can be accomplished by illumination at room temperature[17]. The isolated and paired form of interstitial iron have markedly different recombination properties.[18,19] This leads to significant changes in carrier lifetime and diffusion length after dissociating the FeB pairs. Assuming that all other recombination processes remain unchanged, the FeB concentration can be found by measuring the carrier lifetime before (τ_0) and after (τ_1) pair dissociation: $[FeB]=C(\tau_1^{-1}-\tau_0^{-1})$. The use of the known recombination parameters of both FeB pairs and Fe_i provides the pre-factor C.[18,19,20]

In this paper we show the inverse QSSPC minority carrier lifetime. The *inverse* lifetime is more relevant because it is related to the defect concentrations by the general expression:

$$\frac{1}{\tau} \propto \sum_d \sigma_d C_d = \sigma_{Fe_i} C_{Fe_i} + \frac{1}{\tau_{other}}$$

with σ_d the recombination cross-section of the impurity d and C_d the concentration of the impurity d. Therefore changes in $1/\tau$ are in first approximation proportional to changes in defect concentration (when taking into account precipitates this equation is of course no longer exact). This makes presentation of the results of different gettering profiles more direct and quantitative. The second part of the equation defines τ_{other}, the lifetime that would be found in the absence of Fe_i. This is a useful parameter to track changes in the mc-Si other than changes in concentration of Fe_i.

The spatially resolved minority carrier lifetime was measured by modulated free carrier absorption (MFCA)[21]. The sample is illuminated by a modulated laser which generates carriers. An infrared detection laser beam of 200 μm diameter is absorbed by the free carriers. The transmitted signal will be phase-shifted with respect to the generation laser. From the phase shift, the minority carrier lifetime is calculated. The intensity of the generation laser (5 suns) is high enough to dissociate iron-boron pairs rapidly. Therefore the MFCA lifetime measurements are with interstitial Fe in the dissociated state, which is less recombination active (at excess carrier densities typical for the MFCA measurements) than FeB. This means that Fe_i has only a modest effect on the MFCA measurements. The measurements are primarily used for monitoring changes in recombination activity of grain boundaries and subgrain boundaries.

3 Results

3.1 Wafer characterisation

In tabel 2 we show the substitutional carbon and interstitial oxygen contents of the wafers measured with fourier transform infrared spectroscopy (FTIR). Carbon and oxygen play an important role in the formation of precipitates. Oxygen can be an important inhibiting factor in gettering.[22] In general, from

literature results it seems that precipitates containing carbon or oxygen are much more difficult to remove by gettering than precipitates containing just silicon and transition metals. Oxygen concentrations above 10 ppma (parts-per-million by atom) are known to be a problem for dissolving precipitates, because the oxygen-metal complexes that form above those concentrations have a higher binding energy[12]. The samples used in our experiments all have relatively low carbon content. An oxygen concentration higher than 10 ppma is only found in the bottom wafers of one of the ingots: samples B10.

3.2 Average lifetime and interstitial Fe measurements

The diffusion/gettering was checked for possible contamination from external sources, such as furnace materials. Diffusion on FZ wafers with the same parameters did not reduce their lifetime noticably. Therefore we assume that such contamination can be neglected. We know that some contamination would occur if a PRL were not present, therefore an artefact that could possibly play a role is saturation of the PRL with external impurities, reducing gettering efficiency. From the absence of lifetime degradation for longer gettering times, we conclude that this has not taken place in our experiments.

We tested the two used furnaces to ensure a good match between the resulting emitters. For identical effective temperatures and times, we could make emitters with the same sheet resistance and the same doping profile. With the QSSPC technique we measured a set of sister wafers on lifetime (*see table 3*). We see that the effective lifetime of the wafers all fall within the measurement error of 5%.

The minority carrier lifetime of the wafers was measured without diffusion/gettering, after the standard diffusion/gettering, and after the extended diffusion/gettering. The temperature profiles used are all compatible with a standard emitter sheet resistance. The resulting emitter sheet resistance was within the normal range of 48±2 Ω for all profiles. The effect of the low-temperature tail on minority carrier lifetime is shown in *fig 3*, for a duration of 150 minutes. All wafers show a consistent increase in lifetime after the extended gettering, compared to the standard gettering, but the increase itself differs markedly depending on the origin of the wafer (the ingot and the position in the ingot). The standard gettering and

extended gettering are much more effective for bottom wafers. Especially for ingot A the extended gettering of the bottom wafers A5 results in strong improvement, to a level as good as that of wafers A15 inside the ingot. As can be seen in *fig 3*, there is some spread in the absolute carrier lifetimes measured on the different quarters of the wafers, but the *decrease* of the inverse lifetime is very similar.

Figure 4 shows the lifetime after an extended gettering of 45, 150, and 480 minutes for sample B10. An extended gettering of 480 minutes does not result in any significant additional lifetime improvement compared to 150 minutes. For the 45 minutes extended gettering, exact sister wafers were not available. Wafers from a different brick of the same ingot, at the same height, were used. These show for the 45 minutes low-temperature tail generally a smaller effect than for the 150 minutes tail. Also, the variation in the effect of the extended emitter with a 45 minutes tail is larger than for the 150 minutes tail and the 480 minutes tail.

The results of interstitial iron measurements are displayed in *fig 5.* The absolute amount by which the interstitial iron decreases after diffusion/gettering differs depending on ingot positions and ingots. The improvement of the extended gettering over the standard diffusion/gettering profile is in most cases very significant. The interstitial iron in sample B50 is after standard gettering already close to the measurement limit. It is therefore not possible to measure an effect of extended gettering.

In experiments with contaminated floatzone material (*fig 6)*, we observe that high concentrations of Fe_i can be strongly reduced by standard gettering. In contrast, in samples A5, A15 and B10 standard gettering results in significantly less reduction of Fe_i. Probably this difference may be attributed to the differences between floatzone and multicrystalline silicon, especially the presence of precipitates in the mc-Si sample. Nevertheless, the *extended* gettering removes almost all interstitial iron in the mc-Si samples. We will return to this in the discussion section.

Using the measured interstitial iron (Fe_i) concentration, it can be determined how much of the improvement of the extended gettering is due to removal of Fe_i. In *figure 7*, the change of τ_{other}^{-1} , the lifetime calculated if all Fe_i were absent, is given. The effect of the extended gettering on τ_{other}^{-1} is

comparable to the effect on Fe_i. In all cases the extended gettering is as good as or better than the standard diffusion/gettering. In sample B50 the defects other than Fe_i are not gettered in significant amounts with the standard gettering. An extended gettering however does reduce defects other than interstitial iron. After standard gettering this sample is no longer dominated by Fe_i, but by other defects, of which a number can be gettered by an extended gettering.

Sample B10 has a τ_{other} which does not respond much to extended gettering (*see figure 7*). The additional gettering effect of an extended gettering is almost entirely due to the removal of iron from the sample (compare *figure 3,5 and 7*). Since the lifetime of sample B10 is rather low, it must contain other defects beside iron. These defects are not removable with an extended gettering. From *figure 4* we can see that the lifetime of this sample is not significantly improved after a much longer gettering, so we must conclude that sample B10 contains defects that are very difficult to getter.

3.3 Spatially resolved lifetime

The QSSPC measurements give a geometrically averaged lifetime, which means they strongly emphasise the high lifetime regions. These high lifetime regions are sensitive to Fe_i, and therefore the QSSPC measurements are very sensitive to changes in Fe_i. For solar cells, however, poor quality regions such as heavily dislocated crystals, or grain boundaries, are very important. Changes in these areas are partly reflected in changes in τ_{other}. The low quality regions are also useful to obtain information on behaviour of precipitates. Therefore, it is relevant to study in detail the spatial behaviour of the lifetime changes found above. This was done with MFCA measurements on sections of the samples, at an excitation of 5 suns, and with a gridsize of 0.5 mm.

All MFCA measurements were done with iron-boron pairs in the dissociated state. As noted above the recombination activity of Fe_i is smaller than that of FeB (at the injection levels used in the MFCA). Therefore the observable difference between the standard gettering and the extended gettering is decreased in MFCA measurements compared to the QSSPC measurements. The lifetime with MFCA is generally not equal to τ_{other}, because the recombination activity of Fe_i is still noticeable.

Fig. 8 and 9 show MFCA scans of sections of samples A5 and B10. The areas are approximately the same as used for the QSSPC measurement. Also given is the difference between the standard gettering and the extended gettering (*fig 8c, 9c).* In figure 8 the grains that had a very low initial lifetime increased most in $1/\tau$. The grains with higher initial lifetime are often not much changed in $1/\tau$. Most grain boundaries have an improved lifetime, but the response is sometimes small.
In the MFCA scans of sample B10 (fig 9), we also see that the low lifetime grains are strongly improved by gettering, and grain boundaries are generally improved as well.

4 Discussion

The extended gettering is useful to improve the quality of mc-Si wafers in general, and especially the low quality wafers from the bottom edge of an ingot. It will be similarly effective for wafers from top and side edges of ingots. The improvements occur in areas dominated by recombination at precipitates (grain boundaries) as well as in the bulk silicon lattice, as shown by the reduction of Fe_i. In this section we will try to interpret and explain the results. Where the existing literature on gettering as emphasises the effect of the segregation ratio, a thermodynamic (equilibrium) parameter, it will be shown that more attention is required for the kinetic aspects of precipitate dissolution and impurity diffusion.

Our results show that standard gettering does not remove interstitial iron in the mc-Si samples as much as in floatzone samples with similar or higher concentration. This is consistent with the presence of a significant and continuous supply of Fe_i, during gettering, by dissolution of precipitates. The standard gettering has especially poor performance in bottom sample A5. One can speculate that in that ingot position the precipitates are especially large or abundant (in agreement with ref.[10]).

The low-temperature gettering tails improve the result of gettering. This is related to two main effects: depletion of precipitates, and improvement of segregation ratio to the gettering layer (the PRL).

1. Depletion of precipitates: The MFCA results show that grain boundary recombination decreases, which is a sign of depletion of precipitated impurities. The results of extended gettering improve with duration of the tail. This also indicates a depletion of precipitates. As gettering progresses, the decrease of size or concentration of precipitates will result in a lower average dissolution rate of impurities, and this will shift the balance between dissolution and gettering to a lower concentration of point defects such as Fe_i. Thus, a higher bulk lifetime is obtained.

2. Temperature dependence of segregation: The lower temperature of the gettering tail will also improve gettering. As referred in the introduction, the segregation ratio to the PRL improves. From the effect of longer gettering duration, and dependence of gettering results on sample position, it is clear that the segregation ratio by itself is not the only reason. In fact, in sample A15 the results of standard gettering are already excellent, even though also in that sample most likely precipitates are present. The segregation ratio by itself therefore is not limiting, as is also clear from the FZ sample.

Our results indicate that in mc-Si wafers at high temperature a higher rate of dissolution of precipitates must play a role. Additionally, it is possible (and likely) that a worse segregation ratio at high temperature also limits gettering effectiveness.

Longer gettering at a standard temperature may also result in an increase in average minority carrier lifetime[23]. For depletion of precipitates it could even be more effective because dissolution and diffusion of impurities from precipitates would be more rapid than in a low temperature tail. However, the segregation will be worse than during the low temperature tail. The balance between dissolution of precipitates and diffusion to the PRL will determine the remaining concentration of point defects such as Fe_i. For best results, it is likely that also such gettering would need to be followed by, at least a short, low-temperature tail. The absence of such a tail in the variable temperature gettering experiments by Macdonald et al. may be related to their negative results. The duration of the tail should be sufficient for diffusion of impurities across the thickness of the wafer.

An important negative practical aspect of longer gettering at a standard temperature, as opposed to the low-temperature tail which we discussed, is that it will not preserve the required emitter sheet resistance. It can therefore only be used as pre-gettering (the phosphorous emitter would be stripped). A final practical note is that for long pre-gettering at high temperatures, the cleanliness of the furnace may become an issue, as the PRL may eventually become saturated with impurities.

5 Conclusions

In conclusion, we have found that a limited extension of phosphorous diffusion/gettering can improve the minority carrier lifetime. An increase of gettering time by approx. 2 hours is very effective, and this duration can possibly be reduced. The extended gettering is compatible with a normal emitter sheet resistivity. It has the capability to improve carrier lifetime in bottom wafers of an ingot significantly, and will probably have a similar effect for low-quality wafers from side and top regions of an ingot. It results in enhancement of low quality wafer regions, which will be very important for solar cells.

The extended gettering acts by reducing the interstitial iron concentration, reducing the recombination activity of grain boundaries, and possibly reducing other mobile defects. At least part of the effect of the extended gettering is to reduce precipitates (size or concentration). A low gettering temperature, lower than proposed by Plekhanov et al. for variable temperature gettering, is important. Our results indicate that the effect of temperature on the dissolution rate of precipitates must play a role. Additionally, it is possible (and likely) that the temperature-dependence of the segregation ratio for gettering plays a role.

Acknowledgments

This work has been financially supported by Novem, the Dutch Agency for Energy and the Environment and by the Crystal Clear project of the EC (contract no. SES6-CT-2003-502583). The authors thank the staff of ECN for assistance with the processing and useful advice and discussions.

References

[1] B.Sopori, J. Electronic Mat., vol 31, pg 972 (2002)
[2] K.Kaneko *et al.*, proceedings of PV in Europe, pg 67 (2002)
[3] P.S. Plekhanov *et al.*, Journal of Applied Physics, volume 86, pg 2453 (1999)
[4] T.Y. Tan, NREL2004
[5] C. Ballif, proceedings of 17th EPVSEC München, pg 1818 (2001)
[6] L.J.Caballero proceedings 3rd world conference, pg 1013 (2003)
[7] D. Macdonald and A. Cuevas, proceedings 16th EPVSEC, pg 1707 (2000)
[8] J. Härkönen *et al.*, Solar Energy Materials & Solar Cells, Volume 73, pg 125 (2003)
[9] M. Rinio *et al*, *Defects in the deteriorated border layer of block-cast multicrystalline silicon ingots,* preprint 18th EPVSEC Paris (2004)
[10] T. Buonassisi NREL2004
[11] A.W. Weeber *et al.*, proceedings of 3rd world conference, pg 1131 (2003)
[12] R.A. Sinton and A. Cuevas, Applied Physics Letters, volume 69, pg 2510 (1996)
[13] D. MacDonald *et al.*, proceedings of 29th IEEE, pg 285 (2002)
[14] A.A. Istratov *et al.*, Journal of Applied Physics, volume 94, pg 6552 (2003)
[15] D. Macdonald et al., submitted to J. Appl. Phys.
[16] G. Zoth and W. Bergholz, J. Appl. Phys. 67, 6764 (1990).
[17] K. Graff and H. Pieper, J. Electrochem. Soc. 128, 669 (1981); L.J. Geerligs and Daniel Macdonald, *Dynamics of light-induced FeB pair dissociation in crystalline silicon*, submitted to Appl.Phys.Lett.
[18] D. Macdonald, A. Cuevas, J. Wong-Leung, J. Appl. Phys. 89, 7932 (2001).
[19] A.A. Istratov, H. Hieslmair, and E.R. Weber, Appl. Phys. A: Mater.Sci.Process. 69, 13 (1999).
[20] D.H. Macdonald, L.J. Geerligs, and A. Azzizi, J. Appl. Phys. 95, 1021 (2004).
[21] S. Glunz and W. Warta, J. Appl. Phys. **77**, 3243 (1995); A. Schönecker et al., J. Appl. Phys. **79**, 1497 (1996).
[22] B.L Sopori, L. Jastrzebski and T. Tan, proceedings of 25th IEEE, pg 625 (1996)
[23] eg: A.Cuevas *et al*, Applied Physics Letters vol70, pg 1017

sample code	ingot	height in brick (approx. % from bottom)
A5	A	5
A15		15
B10	B	10
B50		50

Table 1
Wafers used in the experiments. Each sample code represents a set of sister wafers and the quarters of each sister wafer.

code	$[C_s]$ (ppma)	$[O_i]$ (ppma)
A5	4.0	8.0
A15	4.5	7.0
B10	1.4	11.3
B50	3.5	2.5

Table 2
Carbon and oxygen concentration in the samples, determined by FTIR.

Lifetime RTP	Lifetime beltfurnace	Deviation
20.3 µs	21.0 µs	-3%
45.6 µs	46.1 µs	-1%
55.9 µs	55.8 µs	0%
63.3 µs	63.0 µs	0%

Table 3
Lifetime comparison of the used furnaces

Figure captions

Figure 1. Processing sequence of the wafers.

Figure 2. Schematic of the two different temperature profiles used for the phosphorous-gettering in this experiment; i) the standard gettering at a constant temperature T_h, and ii) the extended gettering consisting of diffusion at the same temperature as i) followed by an extended time at lower temperature T_l. The duration of the low-temperature tail was 45 minutes, 150 minutes, and 480 minutes.

Figure 3. Effective recombination lifetime measured with the QSS technique at 10^{15} cm^{-3} minority carrier injection level. As-received, gettered, and improved-gettered results are shown (vertical points correspond to sister wafers). Per sample code two or three different sets of sister wafers are shown. Inset: details of the high lifetimes.

Figure 4. Effective recombination lifetime at 10^{15} cm^{-3} injection level, for different low temperature tails for sample B10.

Figure 5. Interstitial iron concentration for the right-side wafers of each sample code in Fig. 3.

Figure 6. Interstitial iron concentration of contaminated floatzone samples before and after standard gettering.

Figure 7. τ_{other}, the lifetime that would be found in the absence of Fe_i calculated at 10^{15} cm^{-3} injection level, for the same wafers as in Fig. 5.

Figure 8. MFCA lifetime maps of sample B10. a) after standard gettering; b) after extended gettering; c) difference in $1/\tau$ of a) and b).

Figure 9. MFCA lifetime maps of sample A5. a) after standard gettering (a corner of the sample is missing); b) after extended gettering; c) difference in $1/\tau$ of a) and b).

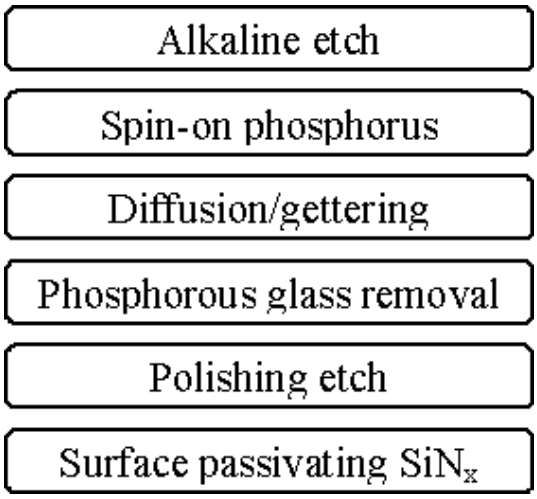

Figure 1

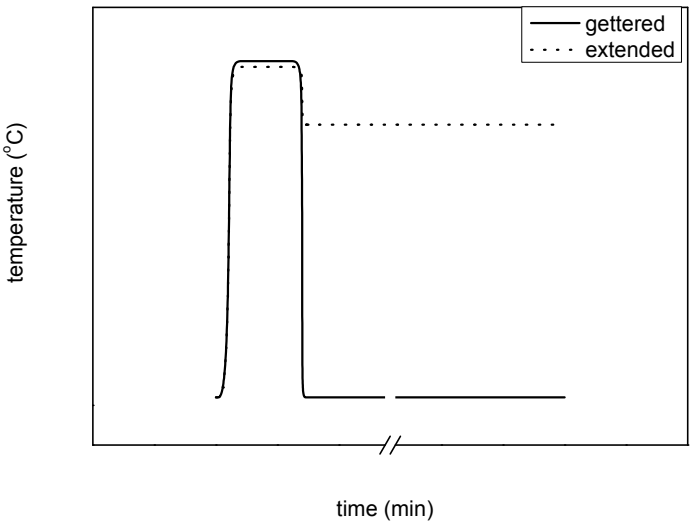

Figure 2

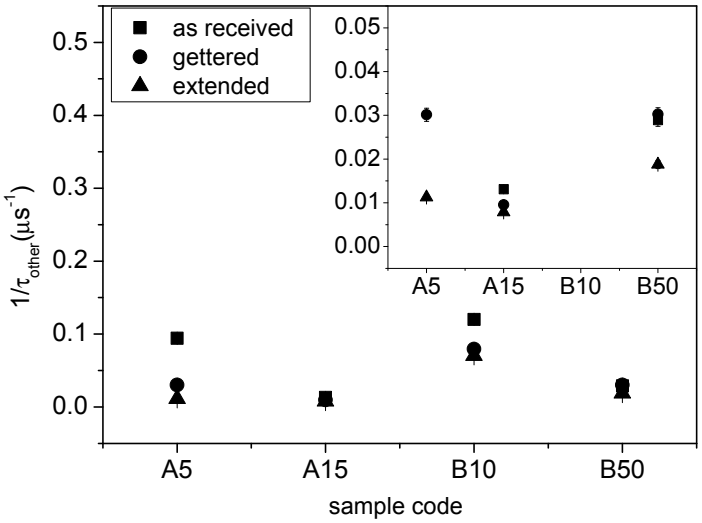

Figure 3

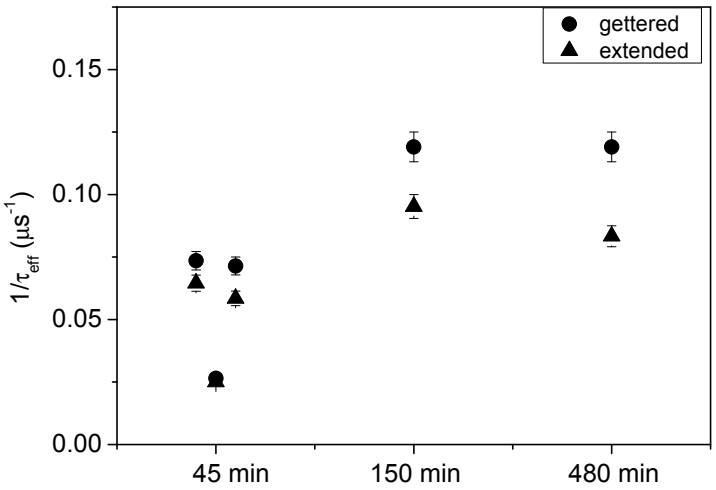

Figure 4

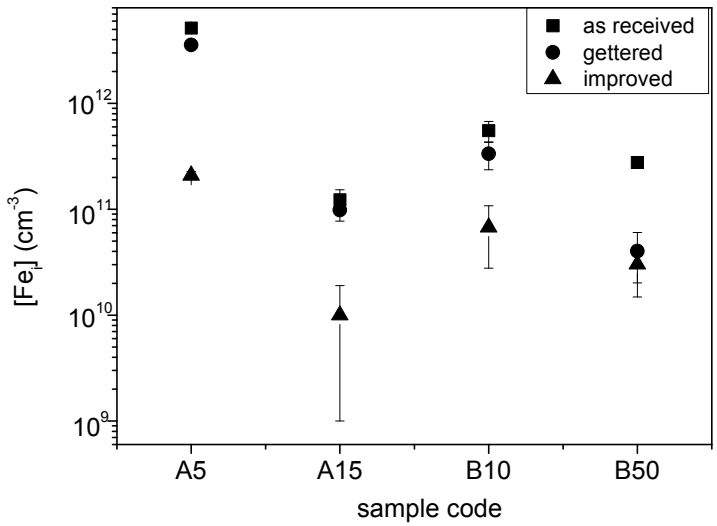

Figure 5

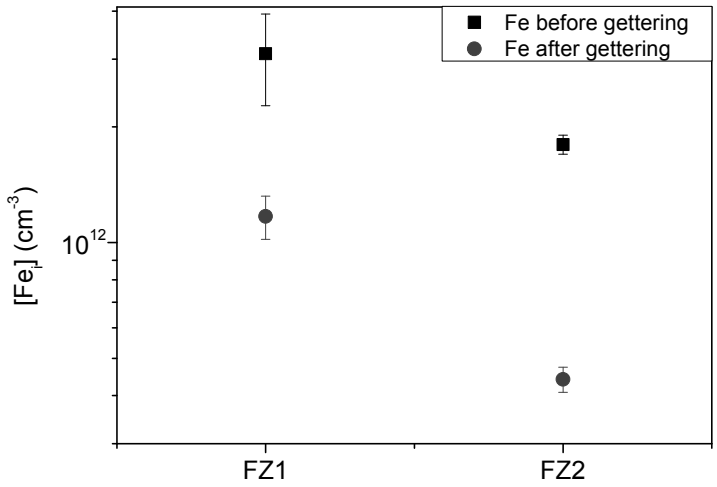

Figure 6

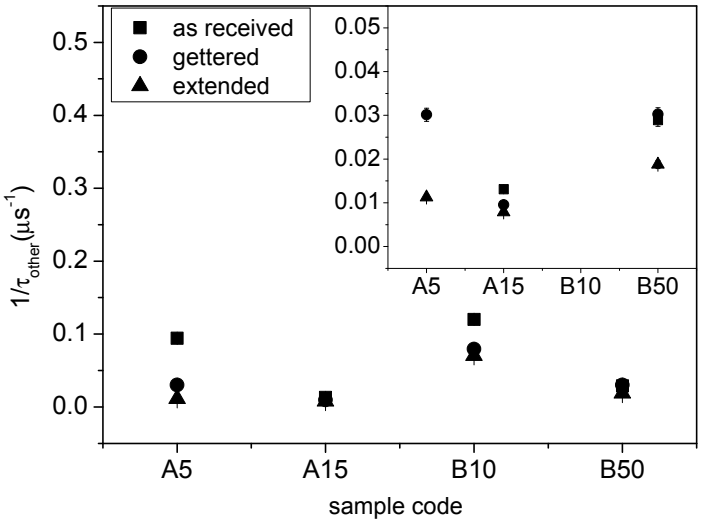
as received
gettered
extended
0.5
0.4
0.3
0.2
0.1
0.0
$1/\tau_{other}$ (μs^{-1})
A5
A15
B10
B50
sample code
0.05
0.04
0.03
0.02
0.01
0.00
A5
A15
B10
B50

Figure 7

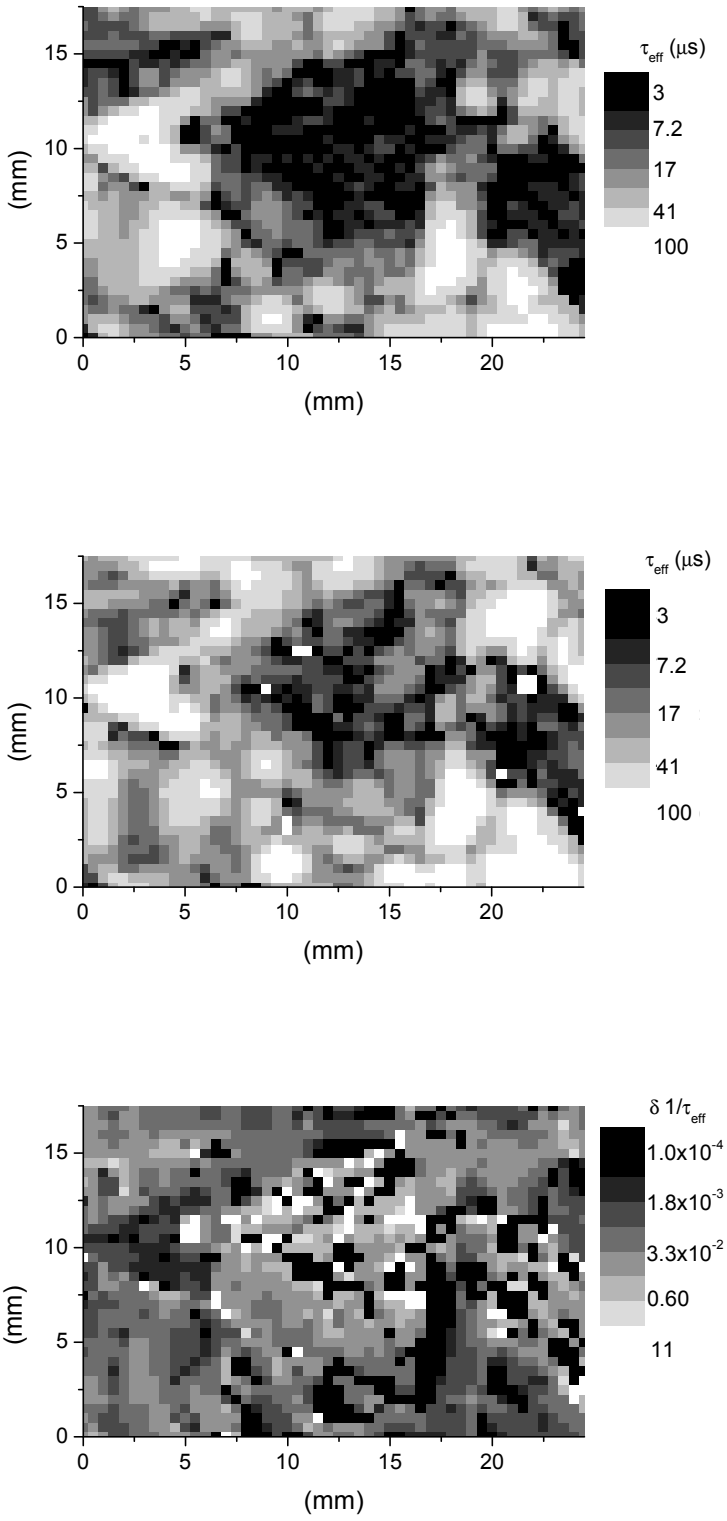
τ_{eff} (μs)
3
7.2
17
41
100
(mm)
0
5
10
15
20
τ_{eff} (μs)
3
7.2
17
41
100
(mm)
δ 1/τ_{eff}
1.0x10^{-4}
1.8x10^{-3}
3.3x10^{-2}
0.60
11
(mm)

Figure 8 a, b, c

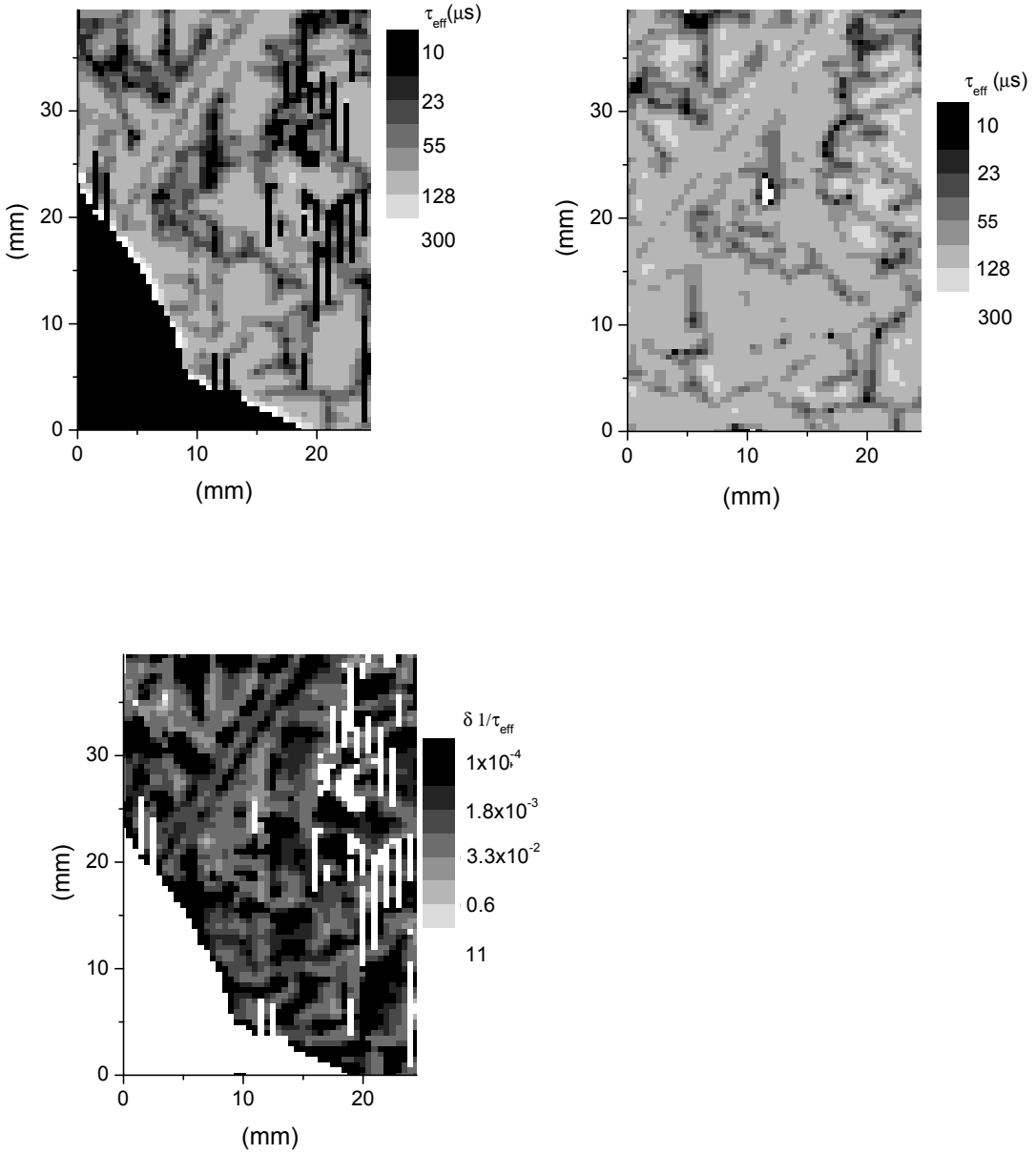
τeff(μs)
10
23
55
128
300
(mm)
0
10
20
30
τeff (μs)
10
23
55
128
300
δ 1/τeff
1x10-4
1.8x10-3
3.3x10-2
0.6
11

Figure 9 a,b,c

APPENDIX A LIST OF PUBLICATIONS AND PRESENTATIONS

Invited talks: presentation and article.

Casting Technologies for Solar Silicon Wafers: Block Casting and Ribbon-Growth-on Substrate. A. Schönecker, L.J. Geerligs, A. Müller. 10th International Autumn meeting on Gettering and defect engineering in semiconductor industry. September 21-26, 2003. Berlin, Germany. Solid State Phenomena **94-95**, 149-158 (2003)

Characterisation of Multi-Crystalline Blocks and Efforts to Relate Their Properties to the Efficiencies of Solar Cells. L.J. Geerligs. 14th Workshop on Crystalline Silicon Solar Cell Materials and Processes. August 8th-11th, 2004. Winter Park, Colorado, USA. pp. 143-151

Journal articles.

Iron detection in crystalline silicon by carrier lifetime measurements for arbitrary injection and doping. D.H. Macdonald, L.J. Geerligs, A. Azzizi. J. Appl. Phys. **95**, 1021-1028 (2004).

Base doping and recombination activity of impurities in crystalline silicon solar cells. L.J. Geerligs and D. Macdonald. Prog. Photovolt.: Res. Appl. **12**, 309-316 (2004).

Recombination activity of interstitial iron and other transition metal point defects in p- and n-type crystalline silicon. Daniel Macdonald and L.J. Geerligs. Appl. Phys. Lett. **85**, 4061 (2004).

Dynamics of light-induced FeB dissociation in crystalline silicon. L.J. Geerligs and Daniel Macdonald. Appl. Phys. Lett. **85**, 5227 (2004).

Transition metal profiles in a multicrystalline silicon ingot. Daniel Macdonald and Andrés Cuevas, A. Kinomura, Y. Nakano, L. J. Geerligs. Accepted for publication in J. Appl. Phys. (2005).

Journal articles submitted or in preparation.

Effective and practical phosphorus gettering of multicrystalline silicon. P. Manshanden and L.J. Geerligs. In preparation for submission to Solar Energy Materials and Solar Cells (2004).

Hydrogen passivation of the grain boundaries in n- versus p-type multicrystalline silicon. A. Azzizi, L.J. Geerligs, and A.R. Burgers. In preparation.

Conference contributions: oral presentation and article.

Recombination Activity of Iron and Other Transition Metals in p- and n-type Crystalline Silicon. D. Macdonald and L.J. Geerligs. 19th European Photovoltaic Specialists Conference, Paris, June 2004. To be published.

Conference contributions: poster and article.

Analysis of cell-process induced changes in multicrystalline silicon. A. Azzizi, L.J. Geerligs and A.R. Burgers. 3rd World conference on Photovoltaic Energy Conversion, May 11-18, 2003. Osaka, Japan. pp. 1384-1387.

Impact of defect distribution and impurities on multicrystalline cell efficiency. L.J. Geerligs. 3rd World conference on Photovoltaic Energy Conversion, May 11-18, 2003. Osaka, Japan. pp. 1044-1047.

Hydrogen passivation of iron in multicrystalline silicon. L.J. Geerligs, A. Azzizi, D.H. Macdonald, and P. Manshanden. 13th Workshop on Crystalline Silicon Solar Cell Materials and Processes. August 10th-13th, 2003. Vail, Colorado, USA. pp. 199-202.

Light-induced Lifetime Degradation in Multicrystalline Silicon. D.H. Macdonald, L.J. Geerligs, and S. Riepe. 13th Workshop on Crystalline Silicon Solar Cell Materials and Processes. August 10th-13th, 2003. Vail, Colorado, USA. pp. 182-185.

Hydrogen passivation of iron in crystalline silicon. A. Azzizi, L.J. Geerligs, and D. Macdonald. 19th European Photovoltaic Specialists Conference, Paris, June 2004. pp. 1021-1024.

Interstitial and precipitated iron content of photovoltaic grade multicrystalline silicon. Daniel Macdonald, Andrés Cuevas, A. Kinomura, Y. Nakano, and L. J. Geerligs. 4th International Symposium on Advanced Science and Technology of Silicon Materials (JSPS Si Symposium), Nov. 22-26, 2004,Kona, Hawaii, USA. To be published.

Conference contributions: poster only.

Studies of Efficiency-limiting Defects in Silicon. L.J. Geerligs, D. Macdonald, P. Manshanden, A. Azzizi, A.R. Burgers. Annual Dutch Solar Cell R&D seminar. Vredenburg, Utrecht, 29 September 2004.